FABRICATION OF POLYMER AND NANOCOMPOSITE MICROSTRUCTURES AND MICROACTUATORS BY CAPILLARY INFILTRATION AND REPLICA MOLDING

by

Davor Copic

A dissertation submitted in partial fulfillment
of the requirements for the degree of
Doctor of Philosophy
(Mechanical Engineering)
in the University of Michigan
2013

Doctoral Committee:

Assistant Professor A. John Hart, Chair
Associate Professor Jinsang Kim
Professor Katsuo Kurabayashi
Timothy J. White, Air Force Research Laboratory

ACKNOWLEDGEMENTS

I had spent the last five years in the beautiful town of Ann Arbor, putting all my efforts towards my graduate work. I have spent over 17,000 hours doing the work that I love. It has been a pleasure not because the work was trouble free, but because it was an incredible exhilarating challenge. At many times it looked insurmountable and –truthfully– many more times I contemplated giving up. I am profoundly grateful for all those that helped me along the way and those who encouraged me to stay and finish my work. I would like to thank:

- My advisor, John Hart, for his infectious passion and drive for research, for his advice and perspective, and for always pushing me to be a better researcher.

- My thesis committee, Professor Jinsang Kim, Professor Katsuo Kurabayashi, and Dr. Timothy J. White, for your support and words of advice on my research, this thesis, and my defense.

- All my lab mates who have suffered with me through the woes of critical experiments gone awry and the pain of treasured samples destroyed in the blink of an eye in the early morning hours. I was happy to help where I could and I am grateful for your help. The time we spent together I will always treasure.

- My family and friends who, more than frequently, reminded me that there is more to life then work and whom I promise to promptly call after I have submitted this thesis (If you are reading this significantly after Sept. 24th, 2013, please bare with me I have years of sleep to catch up on).

- Most of all I'd like to thank my wife, Jennifer, for her never ending support and patience, for her calming and gentle words, and for helping me stay the course.

TABLE OF CONTENTS

LIST OF FIGURES

LIST OF ABBREVIATIONS

AR	Aspect ratio
CF	Capillary forming
CMOS	Complementary metal–oxide–semiconductor
CNT	Carbon nanotube
CV	Control volume
CVD	Chemical vapor deposition
DRIE	Deep reactive ion etch
ESEM	Environmental scanning electron microscope
FEA	Finite element analysis
HAR	High aspect ratio
HMDS	Hexamethyldisilazane
LCE	Liquid crystal elastomer
LCN	Liquid crystal network
PDMS	Polydimethylsiloxane
pHEMA	Polyhydroxyethylmethacrylate
PI	Proportional-integral
PID	Proportional-integral-derivative
PMMA	Poly(methyl methacrylate)
POM	Polarized optical microscopy
PU	Polyurethane
REM	Replica molding
SEM	Scanning electron microscope
TC	Thermocouple
UV	Ultraviolet

LIST OF SYMBOLS

a	Half distance between microstructures
c_x	Set of constants which depend on microchannel geometry
d_{fiber}	Fiber diameter
dr	Infinitesimal length along the radius
$d_{spacing}$	Spacing between fibers
f_x	Set of functions depending on the radius
g	Acceleration due to gravity
h	Channel height
h_{eq}	Capillary rise height
l	Microstructure size
P	Pressure
R_{mi}	Equivalent capillary radius of interstitial space between fibers
V	Average velocity
z	Liquid height
γ	Surface energy
η	Viscosity
Θ_C	Contact angle
Θ_R	Receding angle
ρ	Density
ω	Angular velocity

ABSTRACT

Addition of micro- and/or nanoscale textures to surfaces can enable engineering of a wide range of properties. Passive surfaces (using fixed microstructures) can manipulate cell adhesion, liquid drag, and thermal and electrical contact resistance. Active surfaces (using shape-changing microstructures) can enable modulation of liquid wetting, adhesion, and optical properties. Nevertheless, it remains a challenge to fabricate the mechanically and environmentally robust microstructures and microactuators in large arrays.

This thesis presents new fabrication methods for microstructured polymer and nanocomposite surfaces. Two approaches are pursued: capillary driven infiltration of fabricated carbon nanotube (CNT) microstructures and replica molding (REM) of master templates in liquid crystal networks (LCNs).

First, it is demonstrated that CNT-polymer microstructures can function as robust large-area master molds. The fabricated microstructures include pins, tubes, re-entrant microwells, bent pillars, and high-aspect-ratio honeycombs (thickness of 400nm, aspect ratio 50:1). All are used as master structures for replica molding. A 25-fold replication sequence is shown with no physical degradation of the master or the replicas. Further, the increased stiffness and toughness of CNT-SU-8 microstructures is quantified.

Second, active surfaces were created by capillary infiltration of paraffin into CNT forests. Large stroke sheet actuators, exhibiting up to 20% thermal strain at 175°C are shown. Third, thermally and optically active LCN microstructure replicas were created. Their generated strains were measured to be 6% and 0.25%, respectively. In situ monitoring of the LCN phase and order was also performed. Although having low strains, optically active microstructures are attractive for future work because they can be actuated individually and remotely.

These scalable methods of fabricating microstructured surfaces, both with robust mechanical properties and active geometries, indicate promise for enhancement of liquid wetting, adhesion, optical properties, and thermal conductivity of surfaces and interfaces. However, further increases in the thermally and optically generated strains are needed to make useful active surfaces. This could be accomplished by either material reformulation, improvements in material processing, or strain amplification via design of microstructure geometry.

CHAPTER 1: MOTIVATION AND OUTLINE

Traditionally, planar coatings and random surface textures have provided the main means of engineering surface properties. An alternative approach is to change the microscale texture or structure of the surface. This approach has led to significant improvements in the properties of biological, fluidic, thermal, and electrical interfaces. Additionally, significant strides have been made in using microstructured surfaces to control the wetting behavior of fluids and the adhesion behavior of solids.

Nevertheless, it remains challenging to fabricate microstructures with well-defined nanoscale surface textures and to fabricate arbitrary 3D shapes at the microscale, especially over large areas. Rapid fabrication methods compatible with continuous manufacturing are necessary to achieve this. Additional functionalities are enabled by microstructured surfaces when the microstructures are themselves able to go through a shape change and individually behave as microactuators; such surfaces are referred to as active surfaces. For example, active surfaces are able to locally change hydrophobicity which is useful to manipulate microscale droplets on a surface.

Although there are many approaches to fabricate microstructured and active surfaces, this thesis presents the use of carbon nanotube-polymer nanocomposite microstructures for microstructured surfaces and the replica molding of liquid crystal networks for thermally and optically active surfaces. Comparable approaches suffer from either limited feature geometry and heterogeneity or low throughput. Sections giving an overview of seminal work on passive and active surfaces, CNT-polymer fabrication, and replica molding follow below.

1.1 Microtextured and microstructured surfaces

Microstructured surfaces contain large arrays of positive or negative features with dimensions on the order of 500µm or smaller, while microtextured surfaces contain either random or highly varied features of the same size. Figure 1-1a contains schematics and top down views of simple microstructured surfaces comprising rectangular silicon posts and Figure 1-1b contains a scanning electron microscope (SEM) image of a similar surfaces made of vertical carbon nanotubes (CNTs).

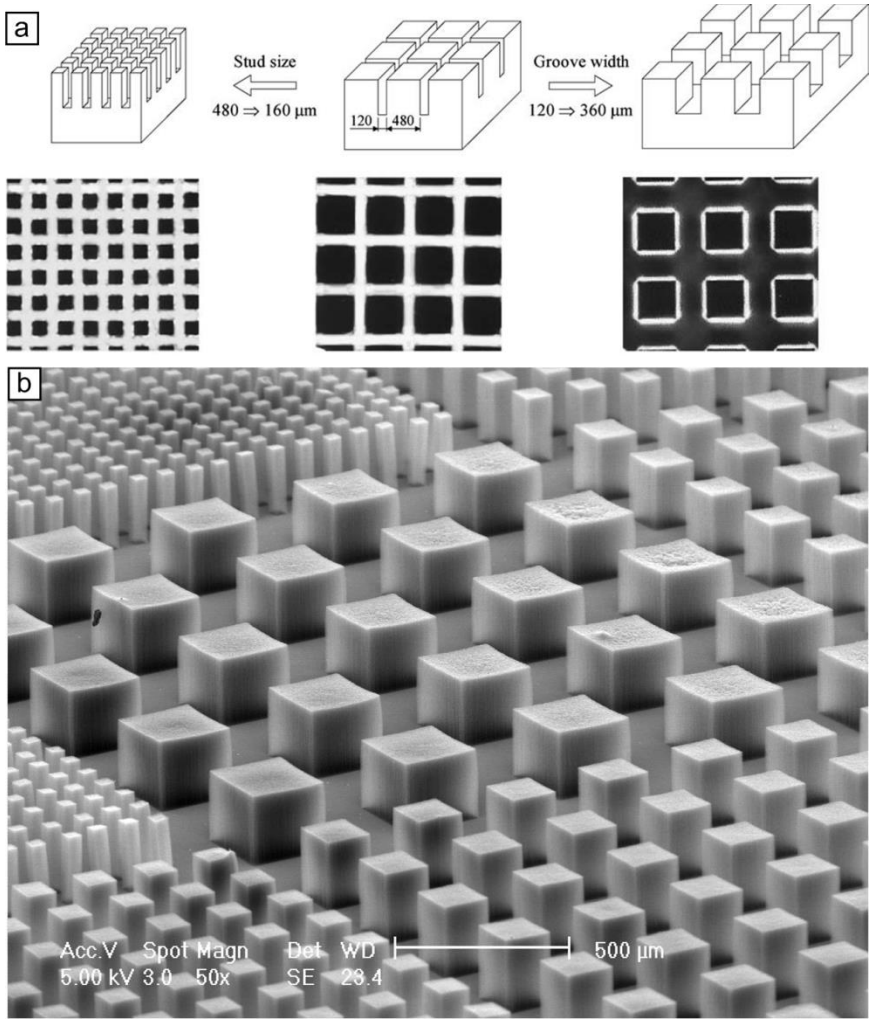

Figure 1-1. Simple microstructured surfaces containing (a) silicon micropillars (taken from [1]) and (b) CNT micropillars.

More complex examples of microstructured surfaces with reentrant, high-aspect-ratio, tilted, and twisting features are shown in Figure 1-2.

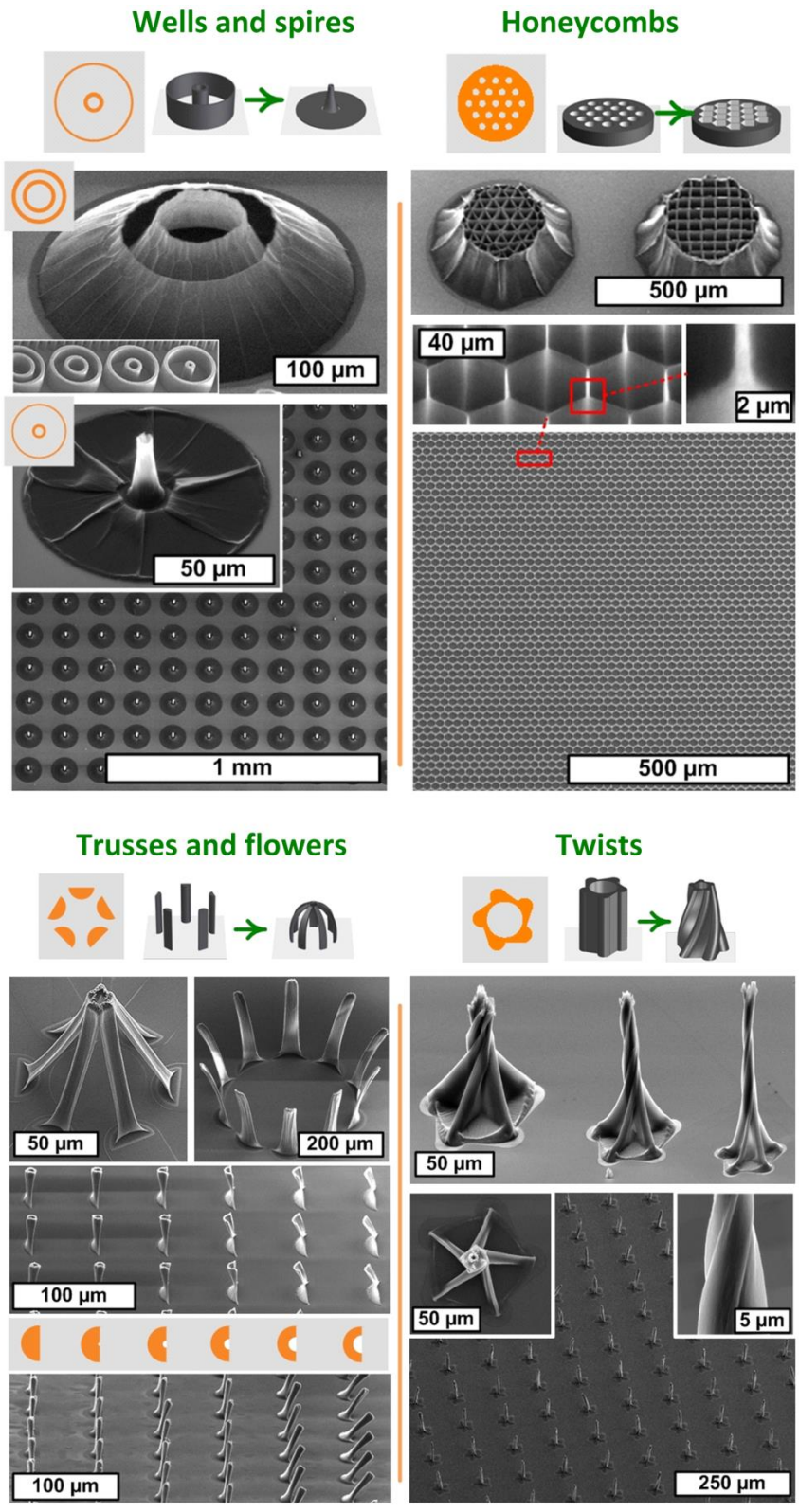

Figure 1-2. Examples of microstructures which can be used in large arrays to form microstructured surfaces. Figure taken from [2].

Microtextured and microstructured surfaces are of long standing interest, since they enhance existing or give entirely new material properties to surfaces as compared to smooth surfaces of the same material. For example, microstructured surfaces are employed in biointerfaces [3, 4], drug delivery [5], the wetting behavior of liquids [6, 7], the dry adhesion of solid surfaces [8, 9], friction [10], thermal interfaces [11], and electrical interconnects [12]. Additionally, multifunctional microstructured surfaces with complex or three dimensional geometries show promise in the areas of metamaterials [13], substrates for cell culture and tissue engineering [14], and lab-on-a-chip systems [15].

For example, Figure 1-3 shows the principle and the design of microstructured surfaces which are simultaneously both superhydrophobic (repelling watter) and superoleophobic (repelling oil). The shown microstructures have complex reentrant geometry.

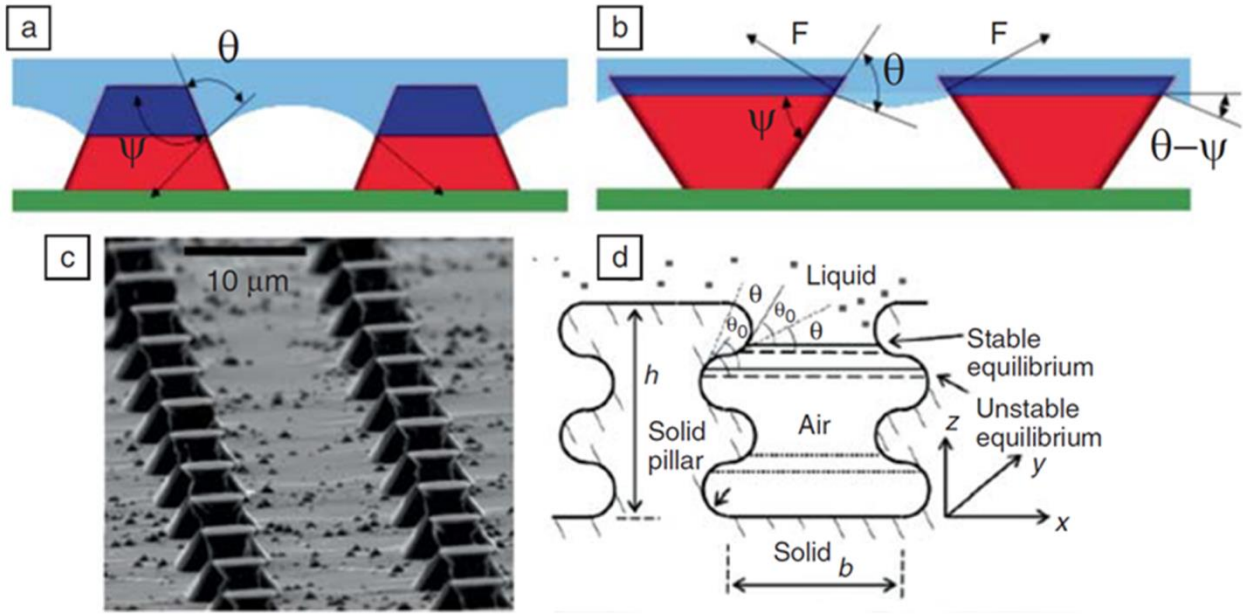

Figure 1-3. Principle and design of superhydrophobic and superoleophobic microstructured surfaces. (a) Salient surfaces are required for superhydrophobicity, while (b) reentrant surfaces are required for superoleophobicity. (c) SEM image of fabricated microstructures which have both salient and reentrant sections. (d) Principle behind simultaneously superhydrophobic and superoleophobic surfaces. Figure taken from [7].

Furthermore, microstructured surfaces can also be used to increase the rate of evaporative cooling by controlling the droplet shape during evaporation, as shown in Figure 1-4.

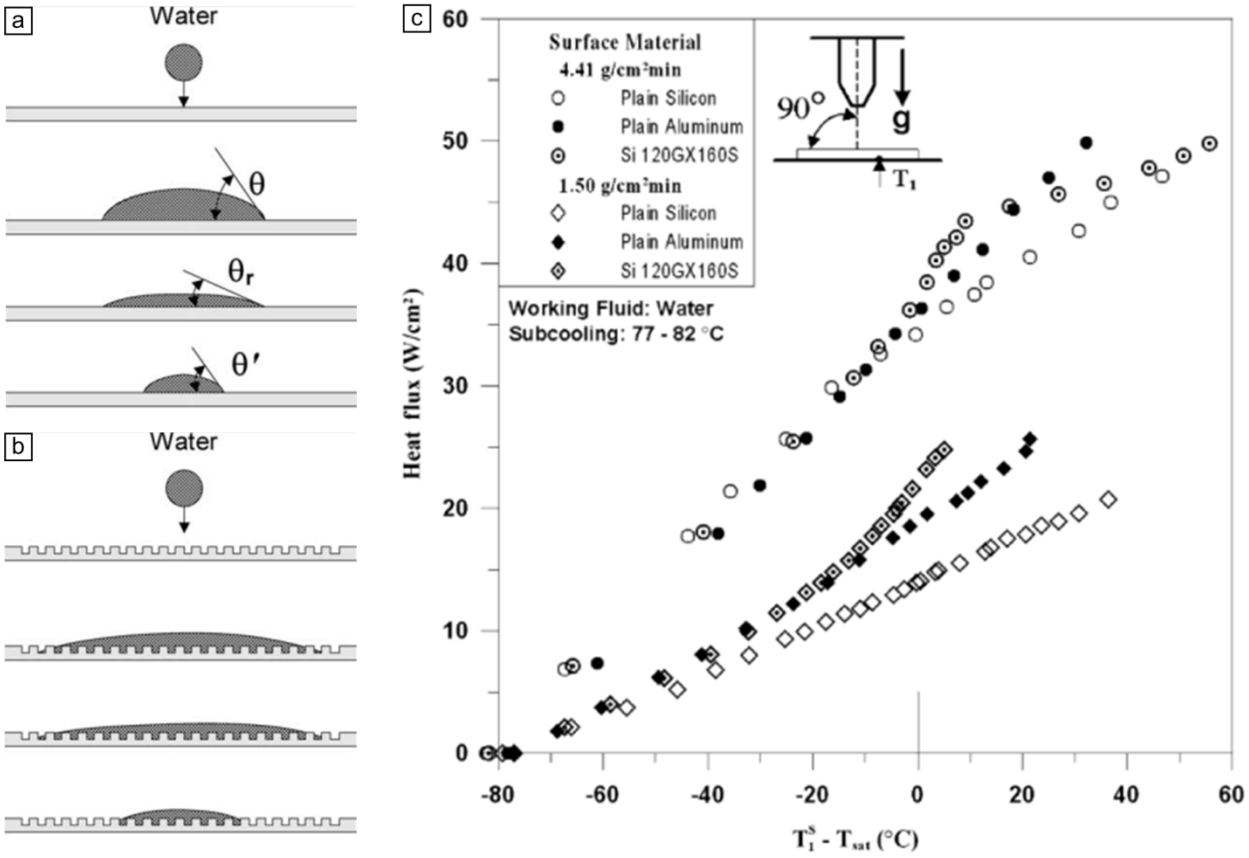

Figure 1-4. Enhanced evaporative cooling on microstructured surfaces. (a) Droplet shape change during evaporation on flat substrate. (b) Increased surface area of evaporating droplet microstructured surface. (c) Relative cooling rates of flat and microstructured surfaces. Figure taken from [1].

As mentioned, microstructured surfaces work well for enhancing dry adhesives, by manipulating the shape of the contact to maximize conformal contact or impart anisotropic adhesive properties, see Figure 1-5. Furthermore, the use of novel microstructured surfaces such as patterned networks of carbon nanotubes (CNT) enables further increases in dry adhesion, see Figure 1-6.

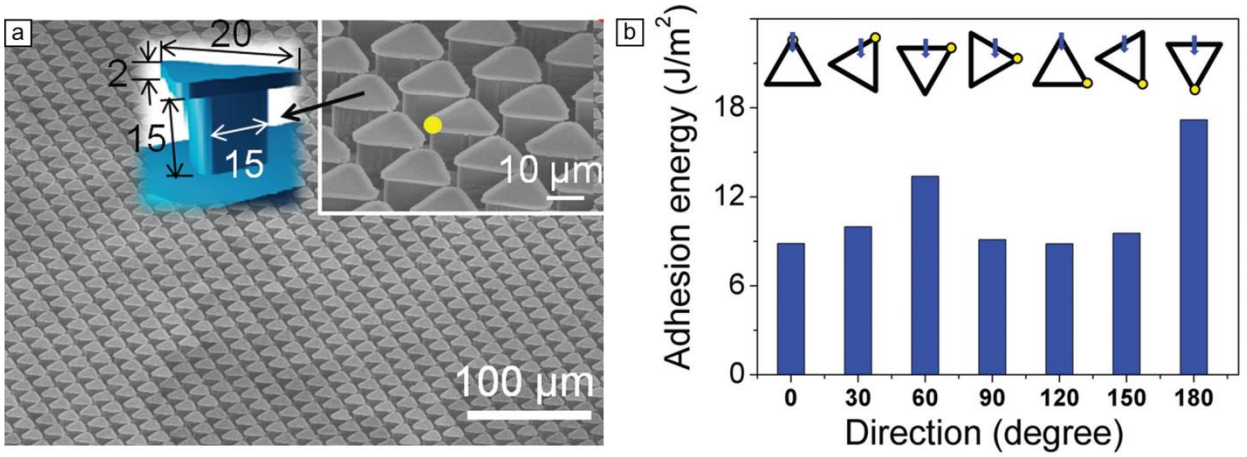

Figure 1-5. Reentrant microstructured surfaces has excellent dry adhesive properties. (a) SEM of PDMS microstructures. (b) Anisotropic adhesion energy of triangular microstructures. Figure adapted from [16].

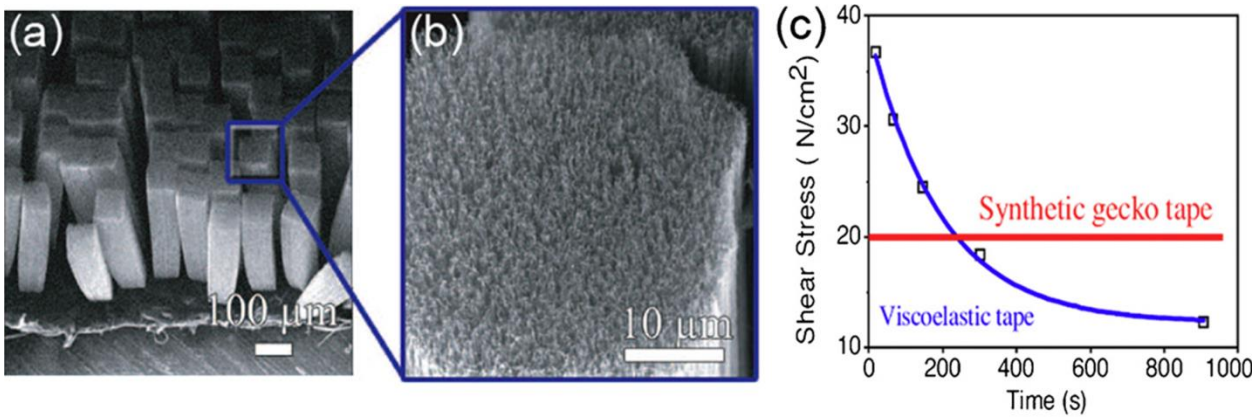

Figure 1-6. CNT micropillar dry adhesive. (a) CNT microstructured surface with (b) closeup (c) shear stress comparison between viscoeleastic tape and synthetic gecko tape. Figure taken from [17].

The idealized microstructure for use in dry adhesive microstructured surfaces is shown in Figure 1-7. These microstructures have high-aspect-ratios (HAR), reentrant and slanted features, as well as hierarchical portions with nanoscale features.

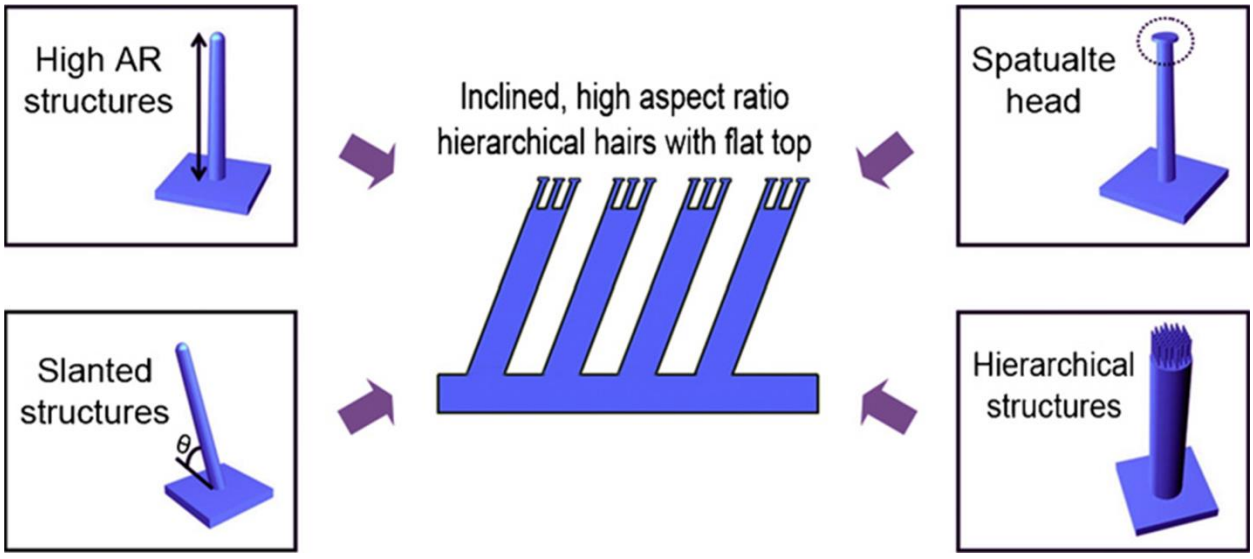

Figure 1-7. Desirable microstructure features for the ideal dry adhesive surface. Figure taken from [18].

However, it remains a challenge to fabricate many of the curved, reentrant, and non-planar surfaces in general which are needed in the aforementioned applications. This is largely due to the tradeoffs which the existing fabrication techniques suffer, which include throughput, heterogeneity, feature geometry, and resolution. Typically parallel methods such as interference or inclined lithography [19] are limited in terms of feature geometry and heterogeneity. On the other hand, serial methods such as stereolithography[20], multiphoton lithography [21], and focused ion beam processing [22] have low throughput, although they can create arbitrarily shaped microstructures. Although, the previously mentioned applications do not place large emphasis on heterogeneity, throughput is of the utmost importance. An additional limitation of these techniques is their reliance on polymers which typically have low mechanical stiffness and toughness, along with low thermal and electrical conductivity.

The primary challenges in moving microtextured and microstructured surfaces toward applications are the limited scalability in many of the used fabrication techniques and the weak mechanical and environmental robustness of the materials used.

1.2 Active surfaces

New capabilities can be added to the previously discussed surfaces by enabling controllable changes in the morphology of the microstructures themselves. Where microstructured surfaces are comprised of large arrays of microstructures, active surfaces are comprised of a large number of microactuators undergoing a shape change individually or in unison in response to a local or global stimulus. This microscale morphology change enables modulation in the properties of active surfaces. For example, local changes in hydrophobicity can be used to manipulate microdroplets on a surface [23] which have utilityin biosensors and microfluidics. Figure 1-8 shows a device consisting of silicon micropillars embedded in a hydrogel [23]. A hydrogel is a polymer network, which is able to swell significantly in the presence of water. In this case, upon wetting of the hydrogel the hydrophobicity of the surface changes locally as the embedded silicon pillars change from a compact horizontal state to a vertical free standing configuration.

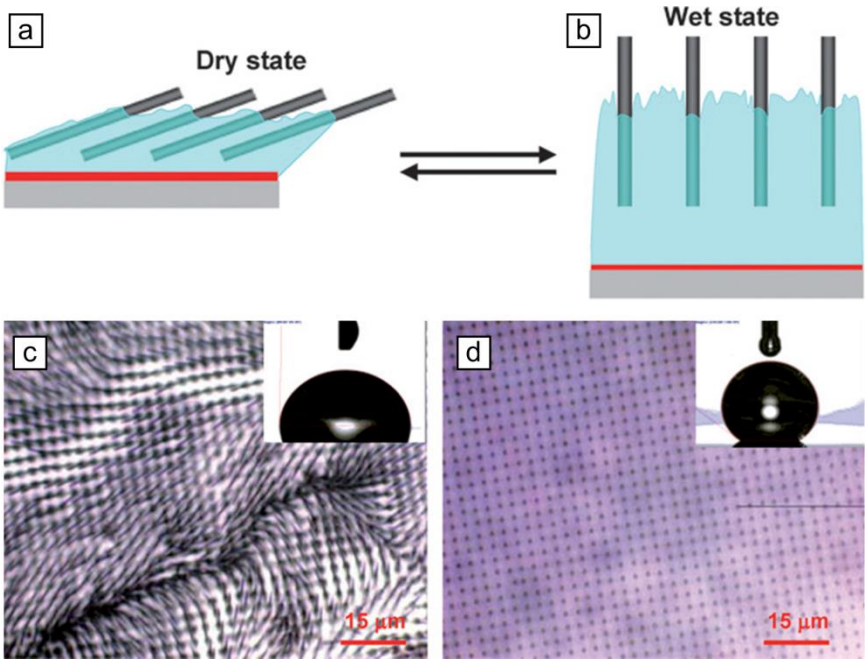

Figure 1-8. Responsive surface changes hydrophobicity upon wetting. (a) Dry state of surface and (b) changed morphology upon wetting. (c) Top down view of dry surface and (d) wetted surface. Figure taken from [23].

Using a similar principle as shown above, Figure 1-9a illustrates vertical micromirrors bending upon the drying of the hydrogel. As the mirrors bend to be parallel to the surface they are able to reflect significantly more light, hence allowing for the modulation of the transmisivity

and reflectivity of the surface. Figure 1-9b shows the change in reflectivity of the surface upon a change in pH.

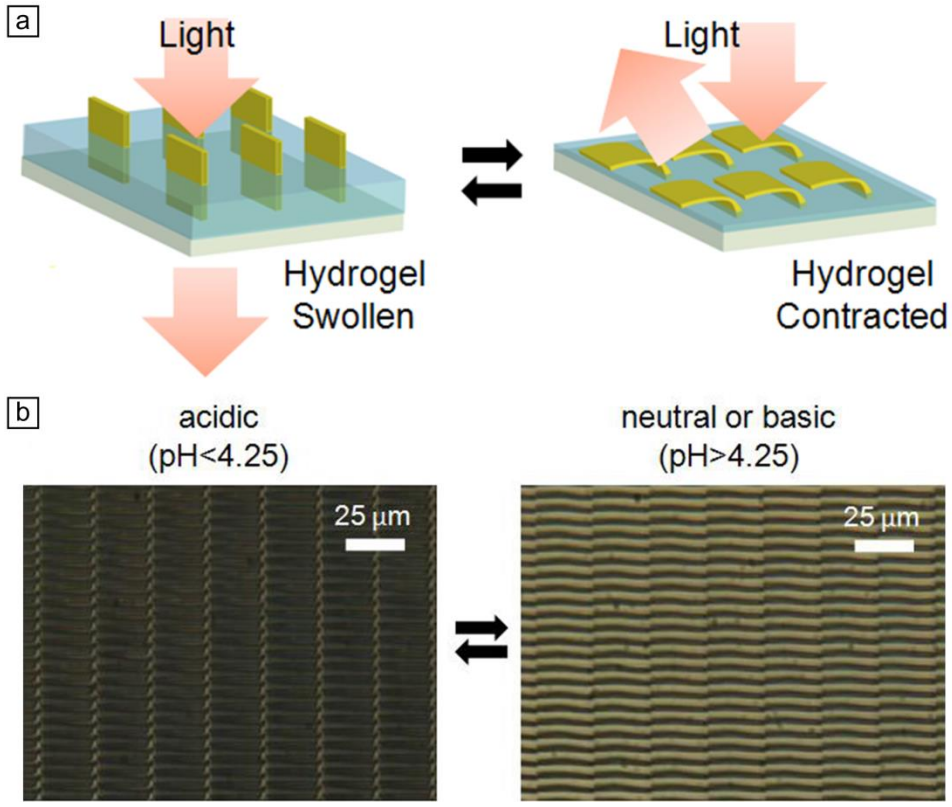

Figure 1-9. Reflectivity/transmisivity modulation of surface by folding of micromirros upon wetting. (a) Schematic of principle and (b) reflectivity modulation based on pH sensitive hydrogel. Figure adapted from [24].

Hydrogels are particularly attractive materials for active surfaces due to their sensitivity to a variety of stimuli, including pH [25], ion concentration [25], temperature [26], solvent composition [26], and electric potential [27]. However, they typically have very poor mechanical properties, particularly the stiffness and toughness is poor in their swollen state, and are not able to exert significant mechanical work. The local and global change in opacity of an adaptive surface is shown in Figure 1-10. Applied stress changes the pore size of a thin film which is wetted by a fluid, with a change of the pore size fluid is expelled or draws into the film for tensile or compressive stresses, respectively.

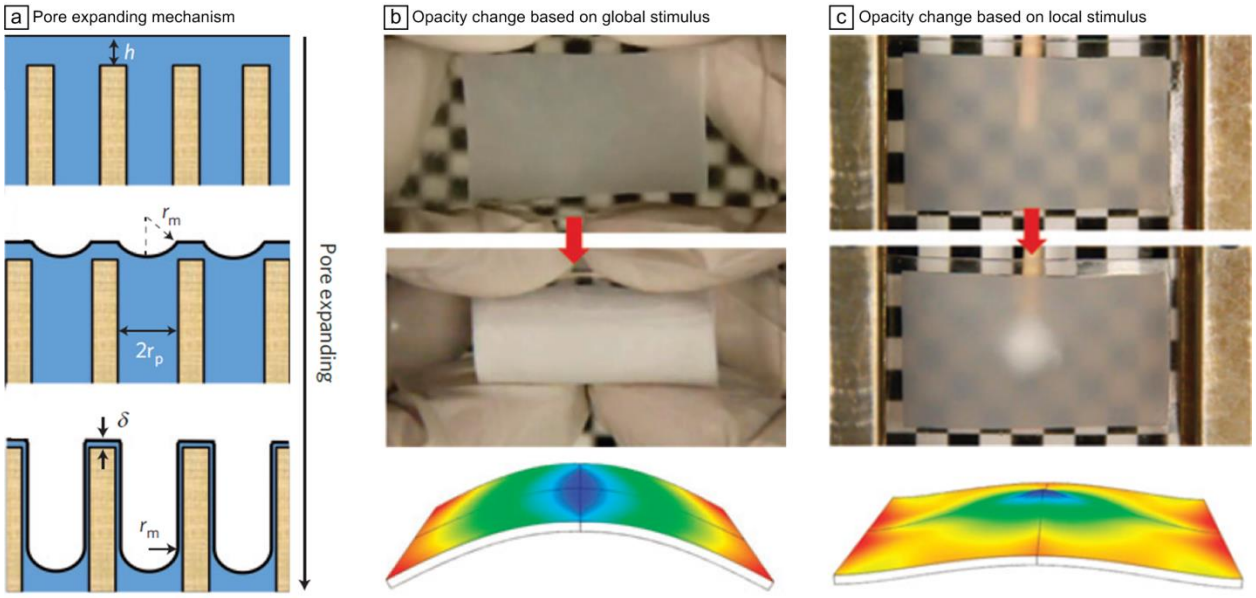

Figure 1-10. Transmisivity modulation of a surface via a local or global stress application. (a) Applied stress changes the pore size inside the material to cause change in transmisivity. (b) Global and (c) local change in transmisivity via application of stress. Figure adapted from [28].

Active surfaces whose shape change is powered by hydrogels or analogous materials offer large scale shape change, but suffer due to lack of robustness, dependence on a controlled environment, and inability to do work. Moving active surfaces towards commercialization requires a significant increase in their robustness and environmental stability. Additional challenges lie in the fabrication of scalable, cost effective, hierarchical, and high aspect ratio (HAR) polymer microstructures. Fabrication of HAR microstructures typically requires controlled deep-etching methods or high-intensity exposure.

1.3 CNT-polymer composites

Carbon nanotubes (CNTs) are carbon allotropes which can be thought of as a single layer of graphitic carbon rolled in a seamless tube on the order of ten nanometers in diameter. This hypothetical sheet can be rolled at discrete angles referred to as chiral angles. Single walled nanotubes with select chiral angles can exhibit either metallic or semiconducting electrical properties, while multiwalled CNTs are always metallic. Multiwalled CNTs consist of two or more concentric walls with spacing on the order of 0.34 nm.

Individual carbon nanotubes (CNT) have been shown to exhibit exceptional mechanical, electrical, and thermal properties. Individual CNTs have Young's moduli as high as 1000 GPa [29], which is five times that of bulk steel; maximum current density as high as 10^9 A cm^{-2} [30], which is three orders of magnitude higher than that of bulk copper; and thermal conductivities on the order of 3500 W/mK [31], which is approximately three times larger than that of diamond. However, a long standing challenge is to fabricate macroscale or larger assemblies of many CNTs with comparable properties to those of individual nanotubes. Typically a reduction of at least 1-2 orders of magnitude in material properties is observed for macroscale assemblies [32]. This degradation of material properties is largely due to low CNT volume fraction, a lack of relative alignment, and poor understanding of the physics and chemistry of inter-particle interactions. Devised approaches to address these issues can generally be grouped in techniques relying on random suspension of CNTs in polymer matrices [33] and approaches relying on the synthesis of CNTs from lithographically patterned catalyst areas [34].

Although the formation of CNT-polymer composites from bulk CNTs requires purification, dispersion, and optionally functionalization, it remains a very attractive technique due to the significant improvements in composite properties over the neat polymer [35-39]. The processing required for CNT-polymer formation can be broken up into three categories: melt-mixing, solution processing, and in situ polymerization. In the preparation of CNT-polymer composites by melt-mixing, thermoplastics are molten and mixed with processed CNT powders; the mixtures can then be extruded or injection molded. Limited CNT alignment can be achieved when combining high-shear mixing with elongation flow [40, 41] and when spinning of extruded melt [42, 43]. Thermosets and thermoplastics as well as their precursors may be combined with CNTs in solution processing. Like melt-mixing, solution processing allows for limited flow alignment via shear flow [44, 45] or electrospinning [46]. The obvious disadvantage of solution processing is the limited amount of CNTs that can be dispersed into the solvent and the frequent need to remove the solvent via drying. Lastly, in situ polymerization disperses the CNTs into a mixture containing predominantly a monomer. The defect sites on the CNTs themselves may be used to covalently bond the polymer to the CNTs enabling excellent load transfer [47-49].

There are two common failure modes of CNT-polymer composites, regardless of which method was used to fabricate them. If the case where interfacial energy between the CNTs and

the host polymer is weak, the CNTs act as nanoscale holes, which in of themselves are stress concentrations and lower the strength of the composite [50]. In the second case the dispersion of the CNTs is either insufficient or the CNTs drop out of solution during processing, forming microscale CNT domains inside the composite. These microscale domains act as microscale stress concentrations and induce failure during loading [51, 52].

Both of the mentioned disadvantages can be avoided by infiltrating vertically aligned CNT 'forests' and microstructures with polymers, instead of forming bulk CNT-polymer composites. The load transfer in CNT microstructures takes place directly from one CNT to another, since the CNTs form a self-supporting network. On the other hand, the added polymer in bulk composites is responsible for the load transfer between CNTs. Not relying solely on the polymer to transfer the load through the material reduces the importance of the CNT-polymer interfacial energy. Because the CNTs in the microstructure are uniformly located throughout the network there are no microscale concentrations analogous to microscale CNT domains which have dropped out of solution. This thesis is guided by the motivation that such pre-patterned and polymer infiltrated CNT microstructures would form excellent candidate materials for microstructured and microtextured surfaces. Furthermore, if the infiltrating polymer is an active material such microstructure arrays would form exciting active surfaces.

1.4 Replica molding of polymeric microstructures

An alternative method for creating microstructured and microtextured surfaces is replica molding (REM) [53-55]. In REM, a stiff and tough microstructures array is used as a master molds. Masters are traditionally fabricated by photolithography and/or etching and include photoresist (e.g. SU-8) master templates fabricated by photolithography and silicon masters fabricated via anisotropic bulk micromachining, such as deep reactive ion etching (DRIE) of a silicon wafer. Next, a soft elastomeric negative is cast from the master, typically using polydimethylsiloxane (PDMS). Replicas of the master microstructured surface can then be transferred in a variety of materials, including PDMS, SU-8, polyurethane (PU), and poly(methyl methacrylate) (PMMA), as well as a variety of metals by electroplating onto a seed layer [56]. A schematic process and representative results are shown in Figure 1-11.

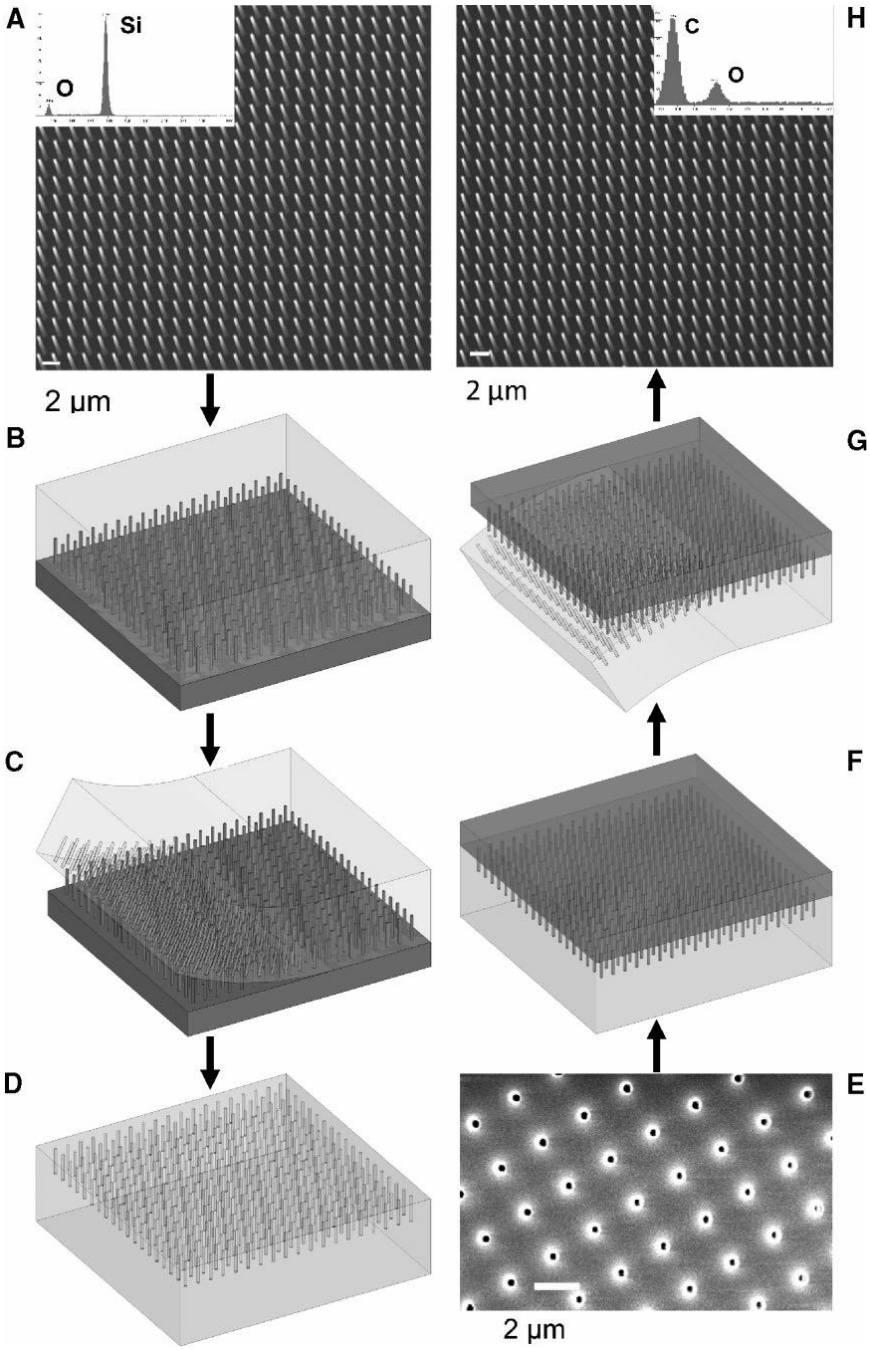

Figure 1-11. (a) Master and (h) replica microstructure array with (b-g) detailed process flow. (b) casting negative PDMS, (c) demodling negative, (d) negative, (e) top-down SEM of negative, (f) casting of replica, and (g) demolding of replica. Figure taken from [57].

Further, active and adaptive surfaces can be created using REM simply by casting a replica from an active material. Although conceptually simple, creating high yield, high fidelity replicas of non-trivial geometries is a challenge. Good candidate active materials have low surface energies, can easily be transferred onto other surfaces, and have anisotropies in their actuation

mechanism or have highly anisotropic responses to certain stimuli. For example, Figure 1-12 shows replica molded thermally active liquid crystal elastomer microstructures undergoing shape change upon heating.

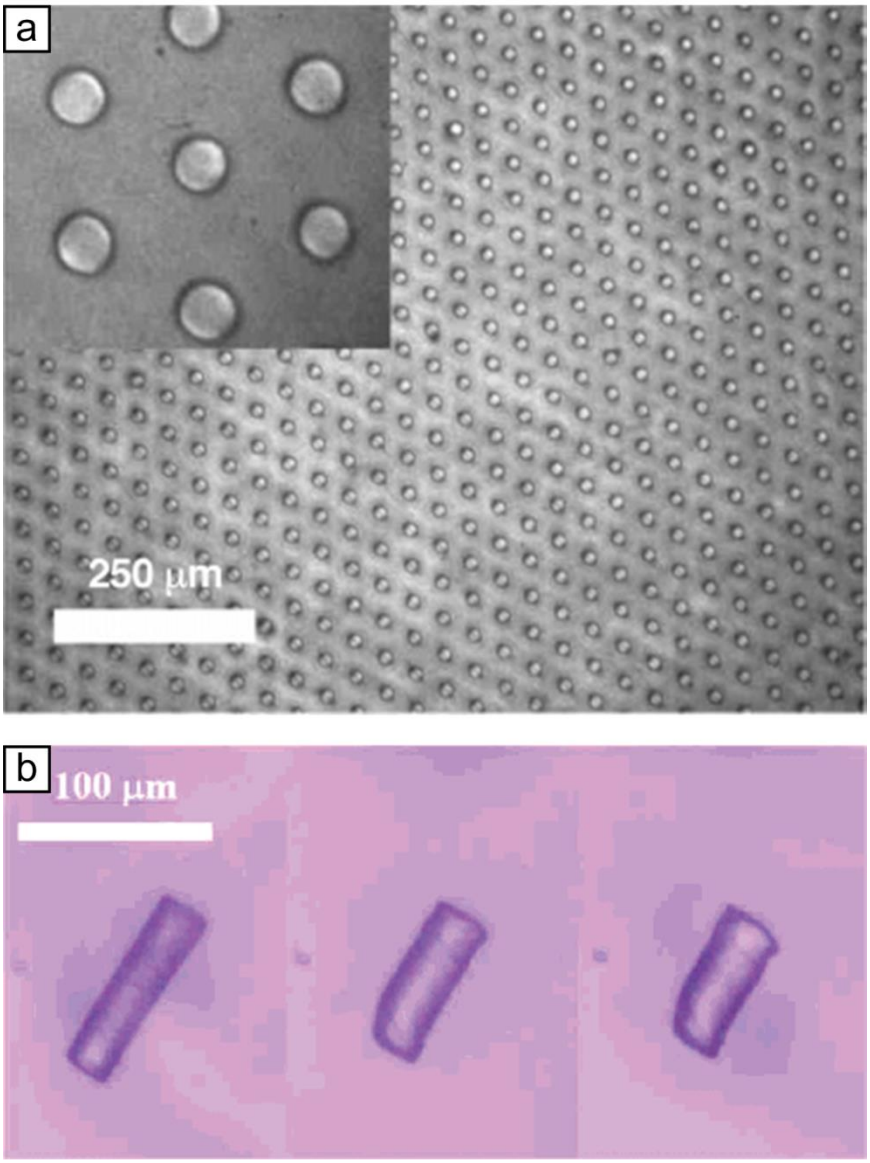

Figure 1-12. Cast thermally active LCE microstructures. (a) Top-down SEM and (b) optical side-view images of microstructures. Micro pillar contracts by 35% at 130ºC. Figure taken from [58].

1.5 Thesis outline

Please note that domain-specific background information is placed at the beginning of each chapter. Because of the heterogeneity of materials and processing topics related to each chapter, the author chose to organize the thesis this way.

Chapter 2 details the newly developed infiltration process for fabricating of CNT-polymer composites (as published by the author in [59] and [60]). The prerequisite steps, including CNT catalyst patterning, CVD growth of patterned CNT 'forests', and CNT capillary forming, are discussed. Additionally, use of the CNT-SU-8 composite microstructures as master molds in replica molding are shown. A library of replicated structures including microscale pins, tubes, reentrant wells, bent pillars, and high-aspect-ratio walls with thickness of 400nm and an aspect ratio of 50:1 is shown. A 25-fold replication sequence is also shown with no physical degradation of the master or the replicas.

Chapter 3 describes the mechanical properties and electrical integration of CNT-polymer nanocomposite microstructures. CNT-polymer nanocomposites are shown to be significantly stiffer than neat polymers. CNT-SU-8 is 3.5 times stiffer then SU-8, while CNT-PMMA is 8.3 times stiffer then PMMA. Additionally, electrical integration of actuating CNT-hydrogel microstructures is shown. CNT-hydrogel composites are used to sense temperature changes. Lastly, a deformable control volume model is developed to show the impact of processing conditions on the liquid level between adjacent microstructures.

Chapter 4 shows that paraffin-infiltrated CNT forests can serve as high stroke vertical thin film actuators (as published by the author in [61]). The actuator is shown to extend reversibly in thickness by 20% at about 150ºC. Use of the actuator as a thermal switch is also demonstrated.

Chapter 5 presents the fabrication of thermally and optically active liquid crystal network microstructured by replica molding (as published by the author in [62]). Optically active LCN microactuators exhibit up to 0.25% strain along the director and a 0.11% contraction orthogonal to it after light exposure. For the first time, centimeter-scale areas

of high aspect ratio microstructures were fabricated, enabled by careful environmental process control and removal of oxygen during casting. In situ monitoring of LCN phase and order during casting was also performed.

Chapter 6 summarizes the key contributions to the field and findings of this work. Ongoing and proposed future work is discussed as well.

Figure 1-13 summarizes the thesis topics, showing the parallel approaches taken towards achieving improved microactuators and active surfaces.

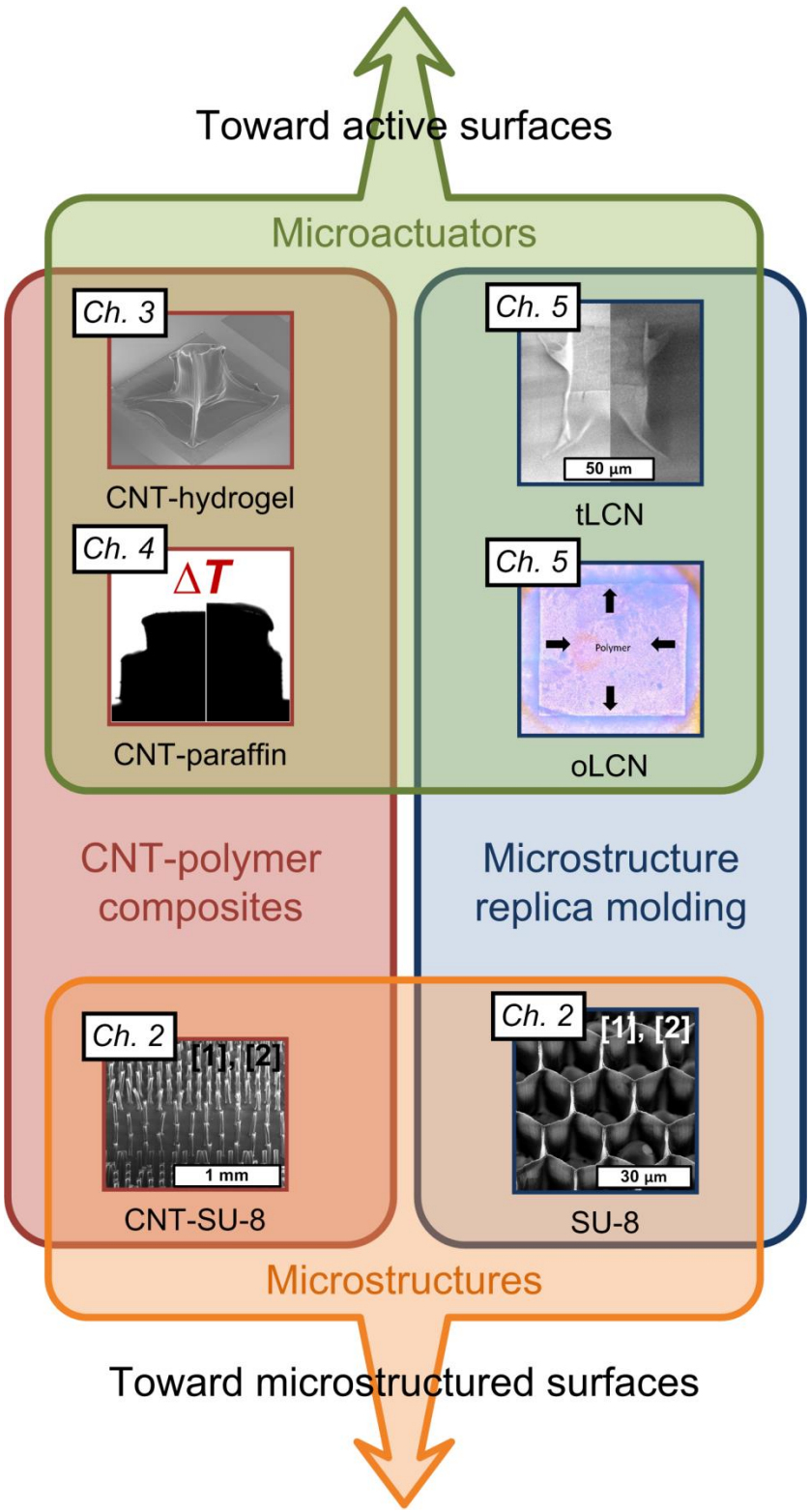

Figure 1-13. Pictorial overview of thesis topics towards microactuators and active surfaces.

CHAPTER 2: FABRICATION AND REPLICA MOLDING OF CNT-POLYMER NANOCOMPOSITE MICROSTRUCTURES

Significant portions of this chapter with additional editing were published in: D. Copic, S.J. Park, S. Tawfick, M. De Volder, A.J. Hart, Journal of Visualized Experiments 65:e3980, 2012, DOI 10.3791/3980, ref [59] *and in D. Copic, S.J. Park, S. Tawfick, M. De Volder, A.J. Har, Lab on a Chip 11(10):1831-1837, 2011, DOI 10.1039/c0lc00724b, ref* [60].

This chapter presents methods for fabrication of patterned microstructures of vertically aligned CNTs and their use as master molds for production of polymer microstructures having controlled nanoscale surface texture. The CNT-polymer nanocomposite master molds are made by (1) growth of vertically aligned CNT patterns, (2) capillary densification of the CNTs using organic solvents, and (3) capillary-driven infiltration of the CNT structures with SU-8. Densification of CNT 'forests' and microstructures is performed by condensation and subsequent evaporation of an organic solvent onto the substrate, which significantly increases the CNT packing density and enables self-directed formation of complex shapes. Lastly, the nanocomposite master microstructures are replicated in SU-8 using standard PDMS transfer molding methods. By this process, a library of replicas including vertical micropillars, honeycomb lattices with sub-micron wall thickness and aspect ratios exceeding 50:1, and microwells with sloped sidewalls were fabricated. The developed process enables batch manufacturing of polymer features that capture complex nanoscale shapes and textures, while requiring only optical lithography and conventional thermal processing.

2.1 Background

The introduction of new materials and processes to microfabrication has, in large part, enabled many important advances in microsystems, lab-on-a-chip devices, and their applications. In particular, capabilities for cost-effective fabrication of polymer microstructures were transformed by the advent of soft lithography and other micromolding techniques [53-55], which in turn led a revolution in application of microfabrication techniques in the areas of biomedical engineering and biology. Precise fabrication of materials and surfaces having controlled shape and texture at a hierarchy of length scales is essential to understand and control the behavior of soft matter. Additionally, the combination of microscale surface geometry with nanoscale texture governs the wetting behavior of liquids [7, 63] and the adhesive character of solids [8, 64]. Further, hierarchical roughness of metal surfaces imparts strong enhancement of optical spectra [65] and electrochemical signals [66] for chemical and biological analysis. There is also a burgeoning interest in the relationship between cell behavior and mechanical cues which are transduced into biochemical signals [67, 68]. For example, the degree of roughness and isotropy of surface texture at 1-100 nm scales has been shown to affect the growth of neurons [69] and cardiomyocytes [70] and the differentiation of stem cells [71]. For these reasons, integration of nanoscale textures with lithography-based fabrication is vital for continued advancement of lab-on-a-chip systems [72].

Nevertheless, it remains challenging to fabricate microstructures with well-defined nanoscale surface textures and to fabricate arbitrary 3D shapes at the microscale. The combination of hierarchical textures and heterogeneous shapes is a profound challenge to existing microfabrication methods that largely rely upon top-down etching using fixed mask templates. On the other hand, the bottom-up synthesis of nanostructures such as nanotubes and nanowires can offer new capabilities to microfabrication, in particular by taking advantage of the collective self-organization of nanostructures, and local control of their growth behavior with respect to microfabricated patterns.

The goal of the work presented in this chapter is to introduce vertically aligned CNTs, which are referred to as CNT forests, as a new microfabrication material and as a host matrix used in formation of nanocomposites. A suite of related methods is presented, including (1) fabrication

of CNT forest microstructures by thermal CVD from lithographically patterned catalyst thin films, (2) self-directed elastocapillary densification of CNT microstructures [2], (3) CNT-polymer nanocomposite formation via capillary infiltration [2, 59, 60], and (4) replica molding of polymer microstructures using CNT-polymer nanocomposite master molds [59, 60]. The development of CNT-polymer nanocomposite infiltration represents a crucial step into taking robust and functional CNT microstructures towards applications; this along with modified replica molding are new developments shown herein. Self-directed capillary densification ("capillary forming"), which is performed by condensation and subsequent evaporation of a solvent onto the substrate with CNT microstructures, significantly increases the packing density of CNTs. This process enables directed transformation of vertical CNT microstructures into straight, inclined, and twisted shapes, which have improved mechanical properties when compared to as-grown CNTs and typical microfabrication polymers [2]. This in turn finally enables formation of nanocomposite CNT microstructures by capillary-driven infiltration of polymers, which can serve as master molds used in REM.

Master molds used in replica molding (REM) are traditionally fabricated by photolithography and/or etching. Photoresist (e.g. SU-8) master templates are fabricated by photolithography, and silicon masters are fabricated via anisotropic bulk micromachining, such as DRIE of a silicon wafer. Master features typically have straight cross-sections and it is difficult to controllably impart nanoscale texture on micro-scale features. Next, a soft elastomeric negative is cast from the master, using PDMS. Replicas of the master can then be transferred in a variety of materials, including PDMS, SU-8, polyurethane (PU), and PMMA, as well as a variety of metals by electroplating onto a seed layer [56]. It has been shown that polymer replication using REM can achieve exceptional fidelity. For example, PDMS molding has been used to replicate textures as small as 0.4 nm which is half the width of a PDMS monomer [73]. The shapes of individual CNTs confined to a surface have also been replicated [74]. Limitations in fabrication of master templates have also motivated use of natural materials as masters, including lotus and rice leafs [75], butterfly wings [76], and viruses [77]. Replicas of lotus leaves were used to create non-wetting surfaces [75], and replicas of butterfly wings were used to create photonic crystals [76].

These developments emphasize that advances in soft lithography are highly dependent on the ability to generate novel and relevant master templates. Thus, bottom-up synthesis and assembly

of nanostructures offer opportunities to create new master materials and geometries. In particular, CNT forest microstructures can span size scales and aspect ratios that meet the capabilities of high-aspect-ratio DRIE and SU-8 fabrication [78-80], suggesting that these structures may be used as a master material for polymer replication. One important challenge is cost-effective fabrication of high-aspect-ratio polymer structures, which traditionally require careful optimization of deep UV exposure of SU-8 [80, 81], or synchrotron X-ray lithography which is not widely available [82].

The replica microstructures cast using the developed process exhibit the anisotropic nanoscale texture of the aligned CNTs, and can have walls with sub-micron thickness and aspect ratios exceeding 50:1. Integration of CNT microstructures in fabrication offers further opportunity to exploit the electrical and thermal properties of CNTs, and diverse capabilities for chemical and biochemical functionalization [83].

2.2 Fabrication process

Each step in the fabrication process is detailed in a separate section below in the following order: (1) catalyst deposition and patterning, (2) CVD growth of CNTs, (3) CNT densification, (4) CNT-polymer nanocomposite master mold fabrication, and (5) replica molding. Figure 2-1 [60] shows a pictorial overview of the process flow, while Table 2-1 [59] summarizes all the employed chemicals and equipment.

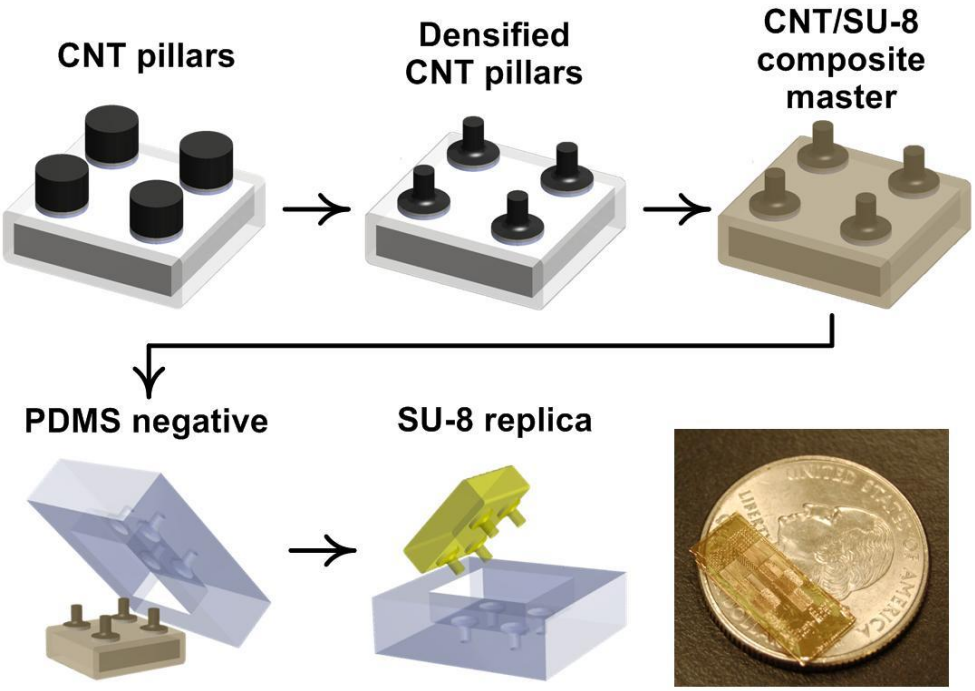

Figure 2-1. Process flow for replica molding of CNT-polymer nanocomposite microstructures, and image of representative replicated microstructure array compared to U.S. quarter dollar coin.

Table 2-1. Used chemicals and equipment in CNT-polymer infiltration and REM.

Name of the reagent	Company	Catalogue number	Comments (optional)
4" diameter <100> silicon wafers coated with SiO_2 (300 nm)	Silicon Quest	Custom	
Positive photoresist	MicroChem	SPR 220-3.0	
Hexamethyldisilizane (HMDS)	MicroChem		
Developer	AZ Electronic Materials USA Corp.	AZ 300 MIF	
Sputtering system	Kurt J. Lesker	Lab 18	Sputtering system for catalyst deposition
Thermo-Fisher Minimite	Fisher Scientific	TF55030A	Tube furnace for CNT growth
Quartz tube	Technical Glass Products	Custom	22 mm ID × 25 mm OD 30" length
Helium gas	PurityPlus	He (PrePurified 300)	
Hydrogen gas	PurityPlus	H_2 (PrePurified 300)	UHP
Ethylene gas	PurityPlus	C_2H_4 (PrePurified 300)	UHP
Perforated aluminum sheet	McMaster-Carr	9232T221	For holding sample above densification beaker
UV flood lamp	Dymax	Model 2000	
SU-8 2002	MicroChem	SU-8 2002	
Polydimethylsiloxane (PDMS)	Dow Corning	Sylgard 184 Silicone Elastomer Kit	

2.2.1 Catalyst deposition and patterning

CNT forests and patterns are grown from a thin film catalyst which is deposited by electron beam evaporation on a thermally-oxidized silicon wafer, as described below.

1. Acquire a (100) silicon wafer with a 3000Å thick silicon dioxide layer, with at least one polished side. Alternatively, you may acquire a bare silicon wafer and grow 3000Å silicon dioxide on the wafer. All processing described below is done on the polished side of the wafer.
2. Spincoat a layer of hexamethyldisilizane (HMDS) at 500rpm for 4s, then at 3000rpm for 30s. HMDS promotes adhesion between the wafer and the photoresist.

3. Spincoat a layer of SPR-220-3 at 500rpm for 4s, then at 3000rpm for 30s.
4. Bake the wafer on a hotplate at 115^{o}C for 90s.
5. Using the desired mask for catalyst patterning, expose the wafer to UV light with an irradiance of 20 mW/cm^2 at 405 nm for 6s in hard contact mode. Bake the wafer on a hotplate again at 115^{o}C for 90s (post exposure bake).
6. Develop the exposed photoresist for 60s using AZ-300 MIF developer.
7. Rinse the wafer for 60s in DI water.
8. Deposit 10nm Al_2O_3 followed by 1nm Fe by e-beam evaporation or sputtering.
9. Manually scribe and break wafer into pieces approximately 20×20 mm or smaller.
10. Perform lift-off of the photoresist by soaking the wafer pieces in a 1L beaker containing 100ml of acetone, while the beaker is placed in an ultrasonic bath at power 6 for 8min (CREST Ultrasonics 1100D).
11. Dispose and replace the acetone and sonicate again with the same settings.
12. Transfer the wafer pieces to a beaker with isopropanol (IPA), and then soak for 2min.
13. Remove the wafer pieces from the IPA individually using tweezers. Dry each piece with a gentle nitrogen stream using a handheld nozzle.

2.2.2 CNT CVD growth

Lithographic patterning and preparation of the CNT catalyst substrates is straightforward and repeatable; however, achieving consistent CNT growth requires careful attention to how the height and density of CNT forests are impacted by the ambient humidity and the condition of the growth tube [84]. The CNT growth rate depends on the temperature, gas composition, and residence time of the gas in the furnace. Thus, it is often necessary to empirically find the "sweetspot" in any growth system. The sweetspot is the location in the furnace which yields the desired density and growth rate. The placement of the samples in the procedure noted here is based the sweetspot for our tube furnace and process parameters.

In general, patterns larger than 1000 μm^2 are less sensitive to small fluctuations in the processing conditions. Further, the density of the patterns affects the local density and height of the CNTs [85]. The growth density and height are larger for patterns with fill fraction (total area of catalyst divided by total substrate area) greater than approximately 20%. Figure 2-2 shows the employed furnace setup and approximate sweetspot location for our system.

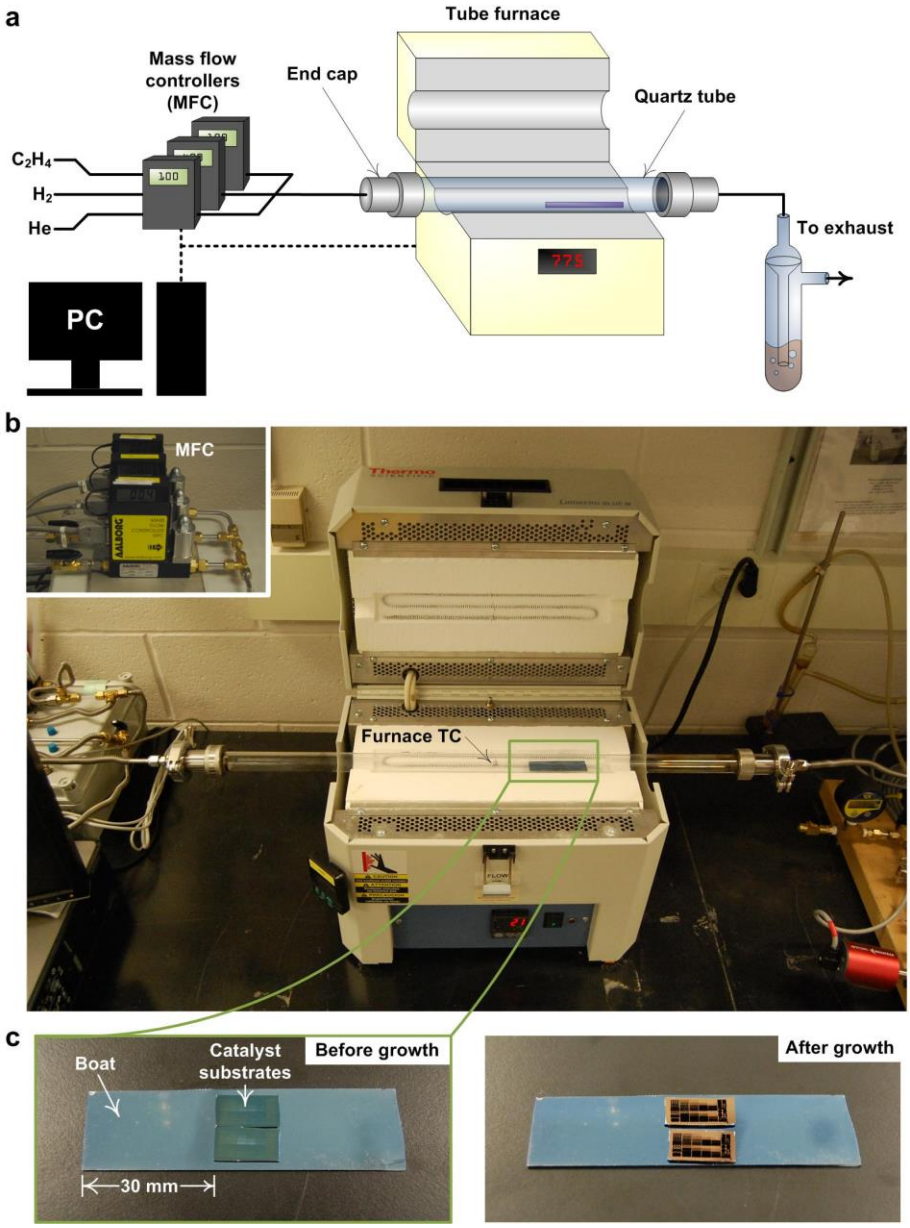

Figure 2-2. Tube furnace setup for CNT growth. (a) System schematic. (b) Tube furnace (Thermo-Fisher Minimite), with cover open to show silicon boat inside sealed quartz tube. (c) Silicon boat with patterned samples, shown before and after growth.

The growth was performed following the procedure detailed below.

1. Acquire a bare (or oxide-coated) silicon wafer and manually scribe and break a piece with dimensions approximately 22×75 mm. This “boat” will be used to support and load the catalyst-coated wafer pieces into the tube furnace.
2. Place a desired number of catalyst-coated wafer pieces (growth substrates) on the boat, 30mm from the leading edge.
3. Load the boat with growth substrates into the tube. Push the boat into the tube such that the leading edge is located 30mm downstream of the furnace thermocouple, using a stainless steel or quartz push rod.
4. Connect the end caps, sealing the tube. Care should be taken to not disturb the position of the boat or the patterned silicon pieces. Note: CNT growth is highly sensitive to position inside the tube.
5. Flush the quartz tube with 1000sccm of helium for 5min at room temperature.
6. While flowing 400sccm of hydrogen and 100sccm of helium, ramp the temperature to 775°C in 10min, and then hold the flow and temperature for 10min. This step causes the iron film to dewet into nanoparticles for CNT growth.
7. Change the hydrogen flow rate to 100sccm and the helium flow rate to 400sccm, while adding 100sccm of ethylene and maintaining the furnace at 775°C to grow CNTs. The height of the CNTs is controlled by the duration of this step.
8. To stop CNT growth and cool the sample, manually slide the quartz tube downstream until the catalyst chips are located approximately 1cm downstream of the furnace insulation or open the furnace. Use care to maintain the same flows and furnace setpoint temperature as in the previous step, for 15 minutes.
9. Flush the tube with 1000sccm of helium for 5min, prior to retrieving the samples, and turning the furnace off.

The adhesion of the CNTs to the substrate is enhanced by rapidly cooling the substrates in the growth atmosphere, which is done immediately after the conclusion of the programmed growth time. In this case, the furnace is opened and the heater power is turned off while the

growth gas mixture is still flowing through the furnace tube. It is also vital to keep the growth tube clean and bake out the tube between consecutive growths to remove accumulated carbon deposits. Tube baking is performed by heating the tube for 30 minutes at 875°C with 100sccm of air flow.

2.2.3 Capillary forming

The use of as-grown CNT microstructures as the masters in replica molding is not possible because forces exerted by infiltration of polymers and especially the viscous forces during spin coating damage the forest. Instead, the CNTs forest is first reinforced and shaped by capillary densification. In accordance with theory of elastocapillary aggregation [86], the aspect ratio of CNT microstructures determines whether the forests densify into a single aggregate or form internal voids [2]. As a rule-of-thumb, cylindrical CNT forests with aspect ratio exceeding 3:1 do not form voids. The cross-sectional dimensions of the as-grown CNT microstructures are chosen so the structures do not form internal voids during elastocapillary densification.

Densification can also change the shape of the pillar cross-section, and this is seen by comparing initially circular pillars, which remain circular after densification, and square pillars which resemble four-pointed stars after densification [87]. Polygonal cross-sections form star-like shapes due the dynamics of liquid infiltration and evaporation through the CNT forest, as well as the nonlinear mechanical stiffness of the CNT forest under lateral compression [88]. For example, pentagonal CNT pillars give five-pointed stars after densification; hexagonal pillars give six-pointed stars, and so on.

Figure 2-3 shows an array of CNT microstructures (a) before and (b) after capillary forming. Additionally, a large defect free array of bent CNT pillars is shown (c). Further, as seen in Figure 2-3, the master and replica structures broaden at the base, because the individual CNTs remain attached to the substrate at the location of their corresponding catalyst particles. Densification causes the cross-sectional area of the pillar to contract approximately 10-fold at the top, representing a 3-fold reduction in the diameter between the base and top. This tapered geometry could be advantageous for mechanical stability of high-aspect-ratio structures, such as fine pins

or needles. The strong adhesion between the CNTs and the forest that causes tapering is also essential for high-yield processing. CNT structures with weak adhesion to the substrate may delaminate during densification, SU-8 infiltration, or demolding of the PDMS negative.

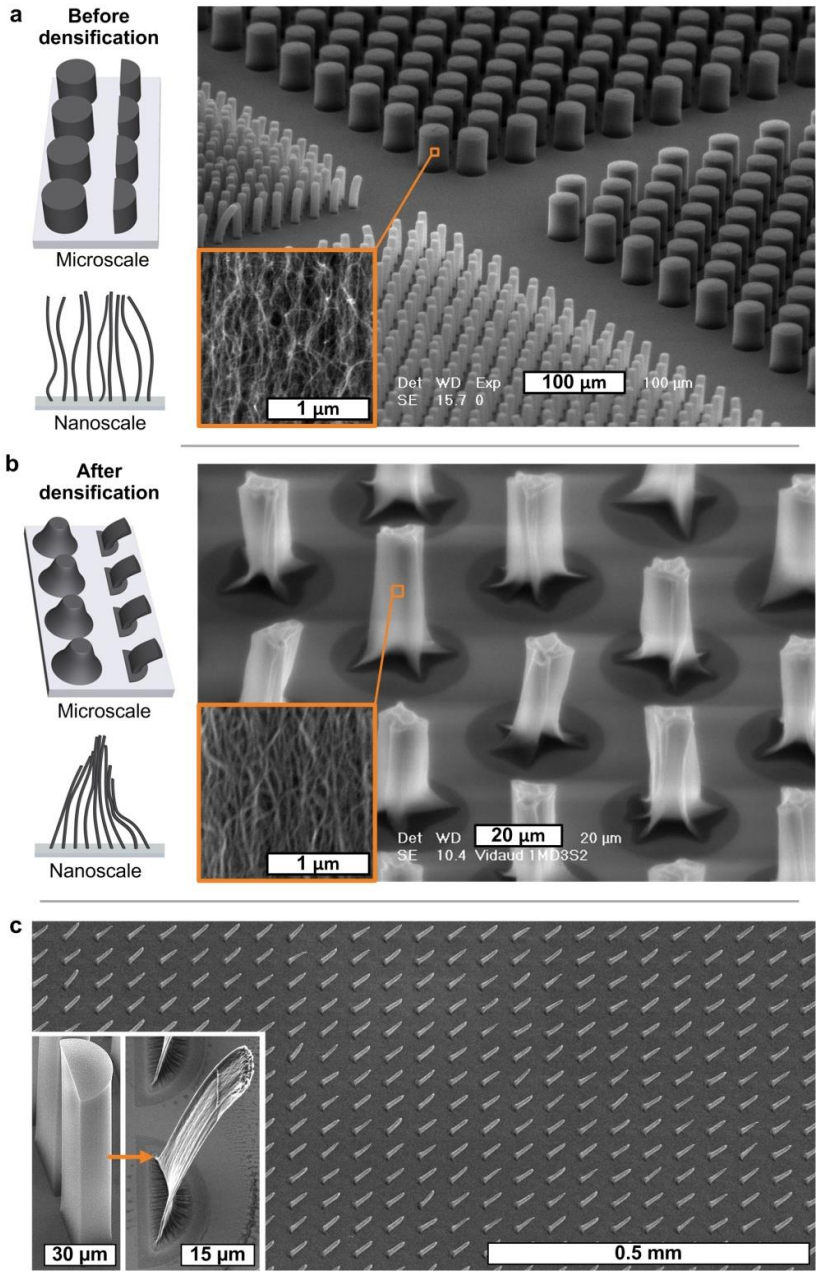

Figure 2-3. Exemplary CNT microstructures before and after capillary forming. Schematic and SEM images of array of cylindrical CNT pillars (a) before capillary forming, and (b) after capillary forming (image modified from De Volder *et al.* [85]). Insets show alignment and density of CNTs. (c) Semicylindrical CNT pillars densify and tilt during capillary forming, forming inclined beams (image modified from [88]).

The most important properties of CNT forests for densification and subsequent master mold formation are their alignment, packing density, and adhesion to the substrate. When CNT microstructures are etched by brief exposure to oxygen plasma, the top "crust" of tangled CNTs is removed. This crust constrains the CNT forest laterally, and therefore removing the crust enables greater densification of the CNTs, and increases the amount of slip that occurs among the CNTs during the densification step. Extended oxygen plasma etching, however, leads to drastically reduced surface adhesion of the CNT microstructures. By tuning the annealing conditions and optionally etching the CNTs, the densification factor can be tuned from approximately 5X to 30X [85]. The setup used to densify CNTs is shown in Figure 2-4.

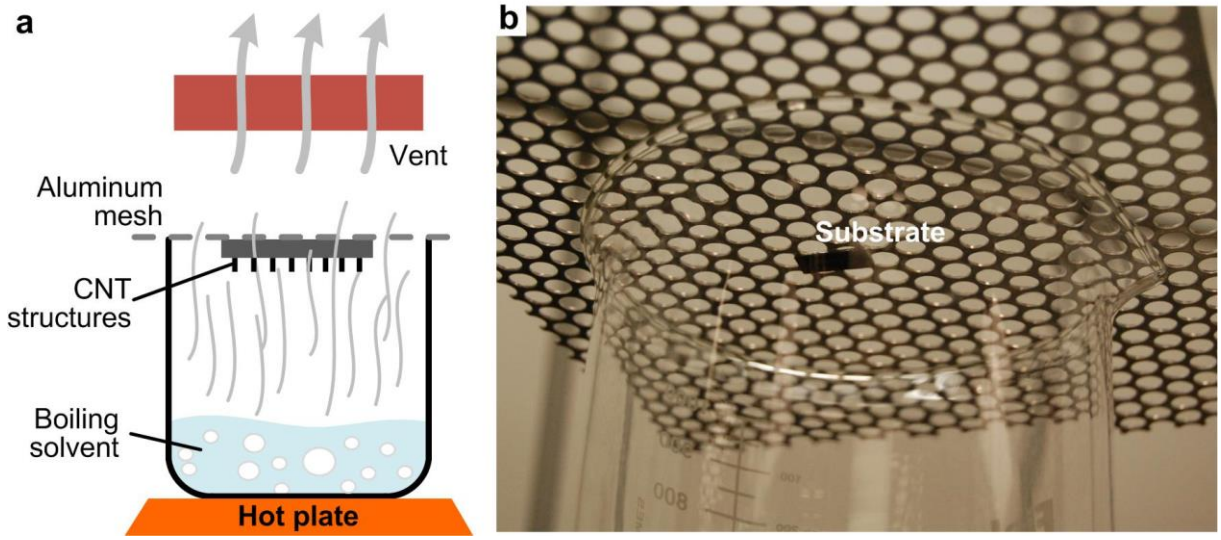

Figure 2-4. Setup used to densify CNTs via capillary forming. (a) Schematic of beaker setup for controlled condensation of solvent vapor onto CNT microstructures (image modified from [85]). (b) CNT sample substrate attached to aluminum mesh over boiling acetone.

CNT densification was performed following the detailed procedure below.

1. Apply a piece of double-sided tape to a 0.8mm thick aluminum mesh with 6.25mm diameter holes. Make sure the mesh is larger than the opening of a 1L beaker and the tape is approximately centered on the mesh.
2. Mount the silicon wafer piece with CNTs on the tape so the CNT microstructures are facing upward.

3. Pour 100ml acetone into a 1L beaker and place the beaker on a hot plate inside a fume hood. Set the hot plate to 150ºC. Wait until the acetone starts boiling.
4. Place the aluminum mesh on the beaker such that the mounted sample is facing downwards.
5. Note any rapid fluctuations in the vapor front rising up the side of the beaker and adjust the fume hood sash level to stabilize the vapor front.
6. Once the vapor front approaches the top of the beaker, observe the apparent color changes on the surface of the silicon substrate. Rainbow-like patterns will appear and sweep across the entire surface. This signifies a thin film of solvent forming on the surface when the vapor comes into contact with the cold surface.
7. Once enough solvent has been deposited, pick up the mesh and without changing the orientation of the sample, hold it away from the boiling solvent until the deposited solvent has evaporated away. The amount of time is determined empirically based on the size and spacing of the CNT structures. This is addressed further in the discussion.
8. Remove the mesh from the beaker, and carefully peel off the sample from the double sided tape, using a razor blade. Utmost care should be taken at this step as it is easy to break the sample during removal.

In order to achieve consistent CNT densification, one must avoid excessive solvent condensation on the substrate. Excessive condensation causes the CNT structures to be flooded, which can warp, flatten, or delaminate HAR microstructures. The required amount of condensation to fully densify the CNTs depends on both the height and density of the microstructures. In practice, the amount of solvent condensation is monitored by counting the number of “waves” of solvent that sweep across the substrate. The colorful waves represent optical interference patterns due to the thin film of condensed liquid on the substrate. For typical microstructures with dimensions 10-100 μm, between 1 and 5 waves are required in our setup. Therefore, the amount of solvent in the beaker may be chosen accordingly, or the sample may be removed from the beaker after the desired number of waves has passed.

2.2.4 CNT master mold fabrication

Master mold formation is highly dependent on SU-8 infiltration. SU-8 infiltration is easily achievable due to surface energies of both the CNTs and the SU-8 resulting in the wetting of the CNTs by the SU-8. Selection of the SU-8 viscosity and spin speeds determines the SU-8 volume fraction and the smoothness of the sidewalls of the master structure. SU-8 wicks into the individual CNT microstructures and, depending on the spacing between the structures, may also wick in the spaces between the CNT structures. This may result in a thin film of SU-8 remaining in between closely spaced structures, and the thickness of this film can be tuned by selecting SU-8 viscosity and spin speed. SU-8 infiltration mechanics are further discussed in Chapter 3. The stated spin speeds result in fully infiltrated structures with heights ranging from 10 to 300μm and with aspect ratios from 0.2 to 20. These process conditions preserve the surface texture of the CNT structures, i.e., the sidewalls and top surfaces do not bulge outward with excess SU-8. A further examination of the resulting structures is given in section 3.3. SU-8 infiltration of CNT microstructure was performed using the procedure detailed below.

1. Pool SU-8 2002 on the densified CNT microstructures. Spin the sample at 500rpm for 10s, then at 3000rpm for 30s.
2. Bake the sample at 65°C for 2 min and then at 95°C for 4 min.
3. Expose the sample to UV light with an irradiance of 75mW/cm^2 for 20s.
4. Bake the sample again at 65°C for 2 min, then at 95°C for 4 min.

The final CNT/SU-8 master mold structures are anisotropic nanocomposites having Young's Modulus of approximately 20 GPa under axial compression [2], compared to published values of 2.1 GPa for SU-8 [89]. The dense CNT/SU-8 composites prevent PDMS from infiltrating the master structures during the replication process.

2.2.5 Replica molding

Vacuum casting of the PDMS negative is a robust process and depends on the initial monomer to cross-linker ratio and the curing conditions. Vacuum casting of PDMS and SU-8 replica molding were performed using the procedure outline below.

1. If replicating delicate structures, place the master in a desiccator along with a glass vile of 100µL of (tridecafluoro-1,1,2,2,-tetrahydtoocyl)-trichlorosilane at 400mTorr for 12h.
2. Mix a total of 1g of PDMS (Sylgard 184), with a ratio of 10:1 monomer:cross-linker. For microstructures with a base size of a few micrometers and an aspect ratio of 10 or more use a ratio of 8:1.
3. Place the CNT master in an aluminum foil dish, and pour PDMS into the dish until the sample is submerged.
4. Place the sample in vacuum and degas at 400mTorr for 15 min. Once bubbles begin to form in the PDMS (typically after about 3 minutes) periodically increase the pressure rapidly to burst large bubbles.
5. Cure the negative at 120°C for 20 min. If the sample contains HAR structures, cure at 85°C for 5h.
6. Once cured, peel back the aluminum foil and separate the master from the soft PDMS negative by hand.
7. If replicating delicate structures, place the negative in a desiccator along with a glass vile of 100µL of (tridecafluoro-1,1,2,2,-tetrahydtoocyl)-trichlorosilane at 400mTorr for 12h.
8. Pour SU-8 2002 into the PDMS negative and degas at 400mTorr for 10min or preferably less, depending on the amount of observable bubbles.
9. Bake the sample (SU-8 filled negative) at 65°C for 4min, then at 95°C for 6h to evaporate the solvent from the thick layer of SU-8.
10. Expose the sample to UV light with an irradiance of 75mW/cm^2 for 20s and bake again at 65°C for 4min and then at 95°C for 8min.
11. Last, manually demold the SU-8 replica from the PDMS negative.

Key steps in this procedure are highlighted in Figure 2-5.

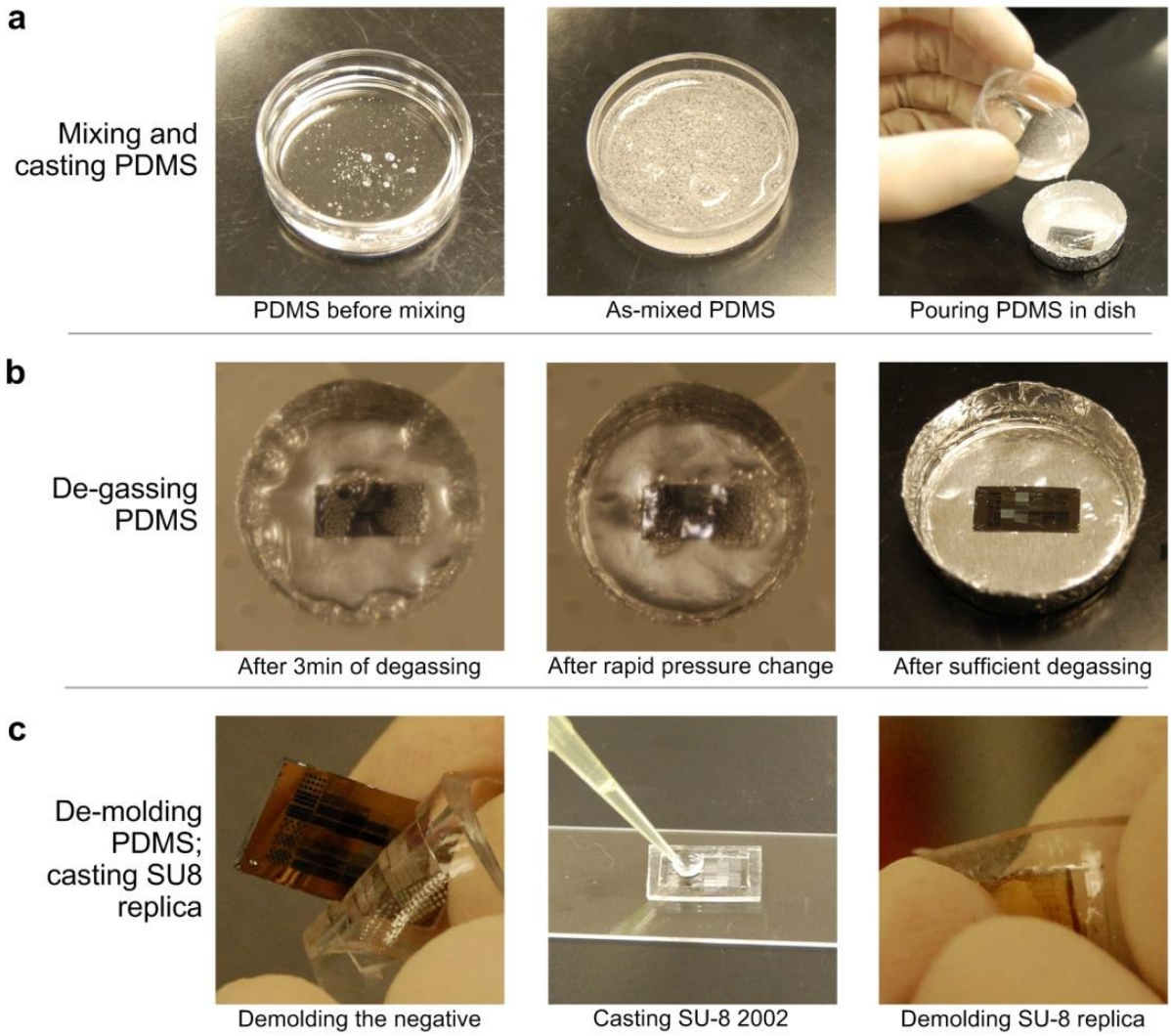

Figure 2-5. Key steps of CNT negative mold fabrication and replica casting. (a) Casting of PDMS negative mold. (b) Degassing of the negative mold. (c) Manual demolding of the negative and casting of the SU-8 replica.

The yield (i.e., survival) of microstructures through the process, and high-fidelity replication of the surface textures, are dependent on the polymer processing and curing conditions. Specifically, curing the PDMS negative slowly at a relatively low temperature ensures low shrinkage of the PDMS, which ensures low stress on the master structures during demolding of the negative. The ratio of cross-linker to monomer in the PDMS recipe affects the rigidity of the negative mold as well as its shrinkage. A stiffer mold more effectively replicated the surface texture of the master, exhibited low shrinkage, and less adhesion to the master. A ratio of 10:1

monomer:cross-linker is used for most castings; however, casting HAR structures (AR>10) with high yield or reentrant structures remains challenging. HAR structures require a mix ratio of 8:1 due to the increased stiffness and reduced adhesion of the negative.

Demolding of the SU-8 replica was assisted by applying a coating of fluorinated silane [57] to the negative as discussed in the methods section. The demolding agent did not compromise the fidelity of surface replication. When casting replicas, degassing may not be necessary due to the prolonged baking. Prolonged degassing was found to lead to inconsistent replication, due to non-uniform evaporation of SU-8 solvent. Finally it was found that completing the post bake procedure after demolding prolonged the lifetime of the PDMS negative, since PDMS oxidation, due to heating, causes it to become brittle and locally fracture during demolding.

2.3 Fabricated CNT/SU-8 nanocomposite microstructures and cast replicas

Polymer replicas of CNT microstructures are made by infiltration of vertically aligned CNTs with SU-8, followed by replication in SU-8 using PDMS transfer molding methods as detailed in the previous section. The process schematic along with exemplary step-by-step results is shown in Figure 2-6. The accompanying images of large substrate areas emphasize the ability to simultaneously replicate structures having different dimensions and spacing, while maintaining the fidelity of their individual shapes and textures.

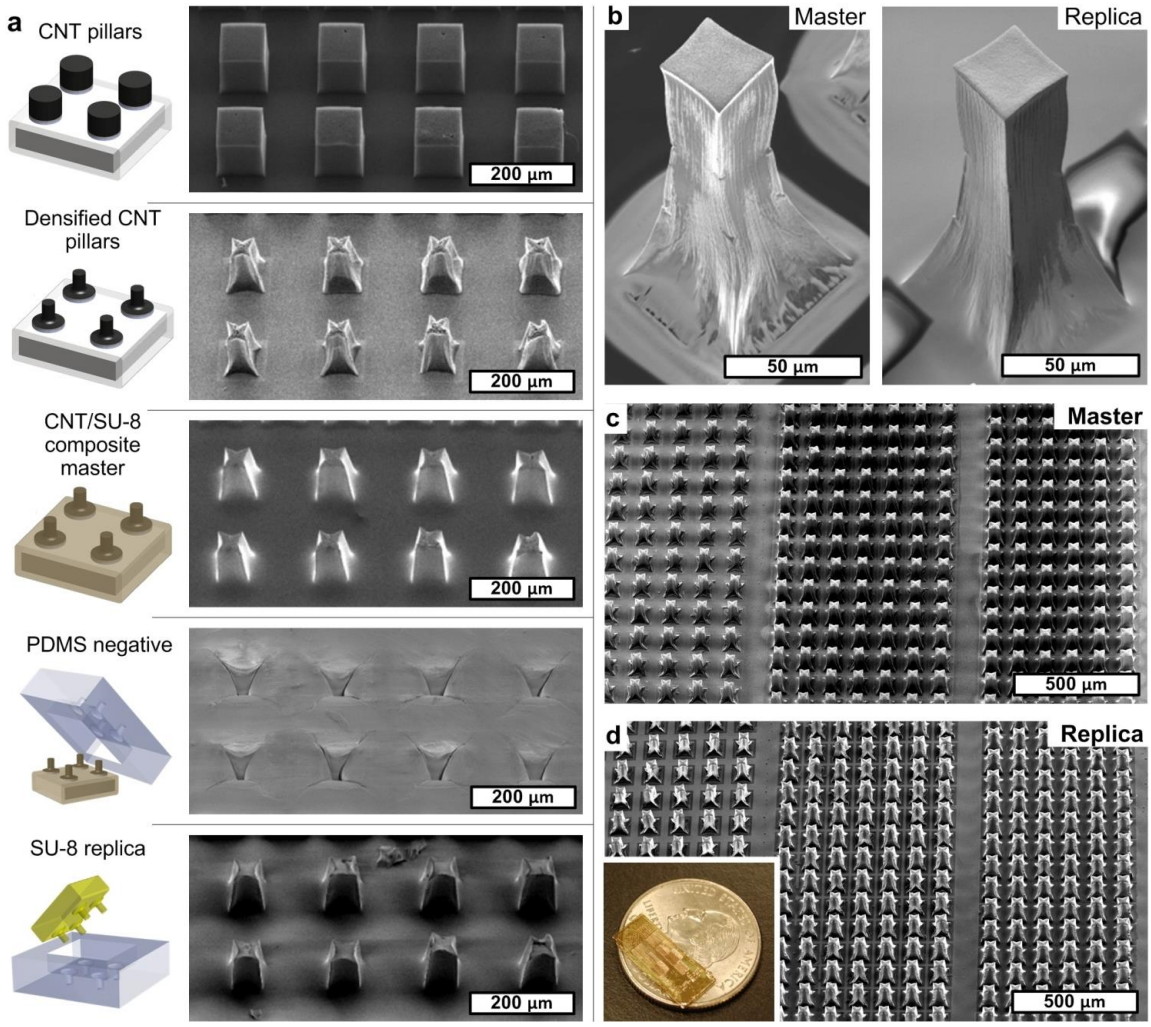

Figure 2-6. Polymer replication using CNT/SU-8 nanocomposite master molds. (a) Process steps and representative structures, starting from array of square CNT forest microstructures; (b) individual master and replica micropillars; (c,d) large array of master structures, and corresponding replica. Inset to (d) shows full replicated chip, placed on US quarter dollar coin (24 mm diameter).

Figure 2-7 compares individual microstructures from master, the first and fifth replicas cast from the first negative (N_1R_1, N_1R_5), and the first and fifth replicas cast from the fifth negative (N_5R_1, N_5R_5). Low magnification SEM images show the replication of microscale form and texture, while higher magnification images show correspondence between the anisotropic texture arising from the vertical alignment of the CNTs. While only a 25-fold sequence was tested, both the master template and the negative PDMS molds do not show noticeable signs of degradation, indicating that this process could facilitate mass production of complex microstructures using a single master template.

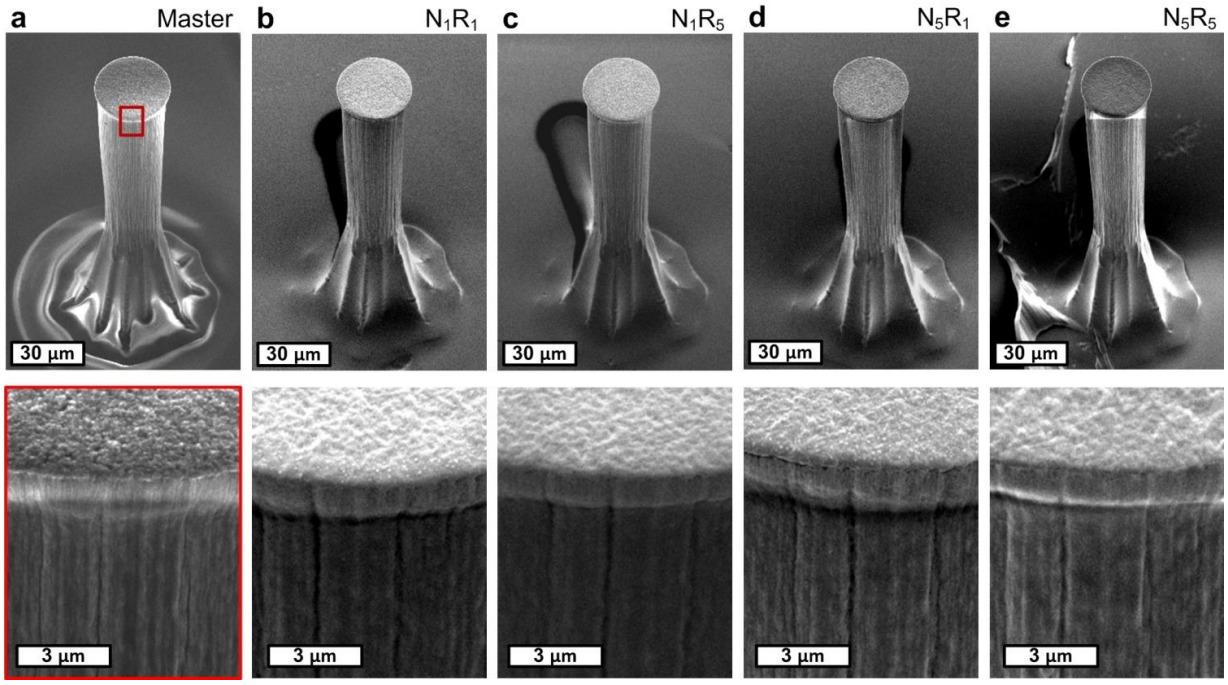

Figure 2-7. Repeated replica molding using CNT master molds, showing the same corresponding micropillar over a 25-fold sequence. (a) Master; (b) first replica cast from the first negative (N_1R_1); (c) fifth replica cast from the first negative (N_1R_5); (d) first replica cast from the fifth negative (N_5R_1); and (e) fifth replica cast from the fifth negative (N_5R_5). The bottom row shows the same respective area, per the red outline in (a), of each structure.

Atomic force microscopy (AFM) was used to compare the surface morphology of corresponding areas on master and replica pillars, and these scans are shown as 3D surface plots in Figure 2-8. It was found that the average roughness (R_a), and the root mean square roughness (R_q), of the master surfaces is slightly higher than the corresponding replicas. Therefore, the replica is not "filling" the smallest crevasses in the negative or the surface roughness is changed once the PDMS negative shrinks during curing. The nanoscale fidelity of replication depends on the curing conditions of the negative and replica, both of which control the shrinkage and warping of the mating surfaces [73]. The fidelity of replication could likely be further improved by studying the impact of curing parameters on the nanoscale texture of the replicas.

Figure 2-8 shows the smallest length-scale (sub-micron) of the hierarchical texture. The smallest length scale is due to the waviness of individual CNTs. The intermediate length scale (microns) is created by the kinks and wrinkles on the surface of the microstructures, while the largest length scale (tens of microns) is composed of the microstructures themselves. Adjusting parameters at various length scales may allow for design of complex hierarchical surface texture.

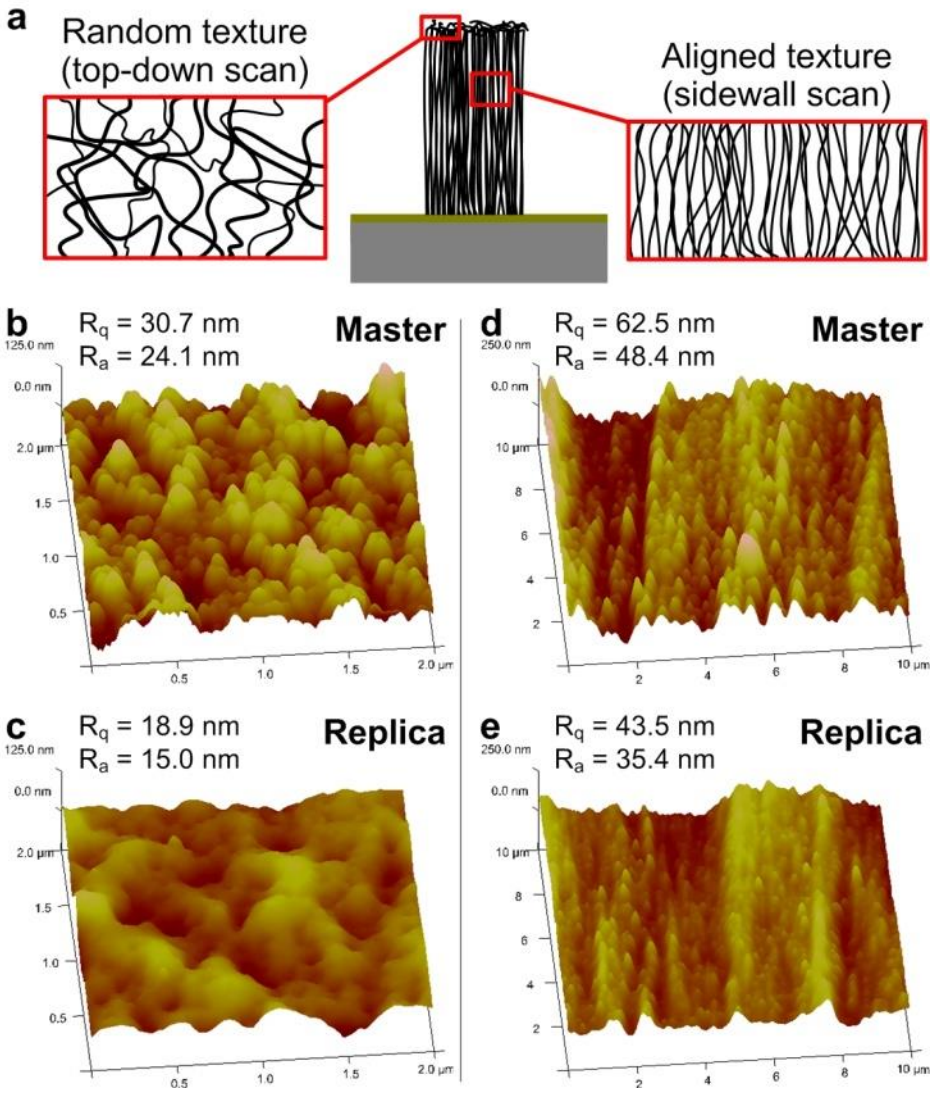

Figure 2-8. AFM analysis of texture replication. (a) schematic representation of scanned areas; (b,c) corresponding scans (2 × 2 μm) of top surface of master and replica pillar; (d, e) corresponding scans (10 × 10 μm) of sidewall surface of master and replica pillar.

One of the classical challenges of microfabrication is to create high-aspect-ratio (HAR) structures. To this end, we used capillary densification of large-area CNT forests containing arrays of lithographically patterned holes to produce "honeycomb" [2] master molds as shown in Figure 2-9. The walls shown have 400 nm width and heights of approximately 20 μm, representing an aspect ratio of approximately 50. While previous work has directly fabricated SU-8 structures with AR = 100 using UV lithography [80], and greater performance is shown by X-ray lithography [82, 90]. It is important to note that achievable aspect ratios decline for structures with critical dimension of 1 μm or less. Here, the honeycomb masters are made by

optical lithography using 1:1 masks, followed by resolution enhancement due to densification. With higher resolution lithography, these geometries could in principle be reduced to the width of a few CNTs. Overall, the capability to fabricate and replicate such tall and thin polymer features is aided by the mechanical robustness of the nanocomposite master, which prevents the walls from tearing during demolding.

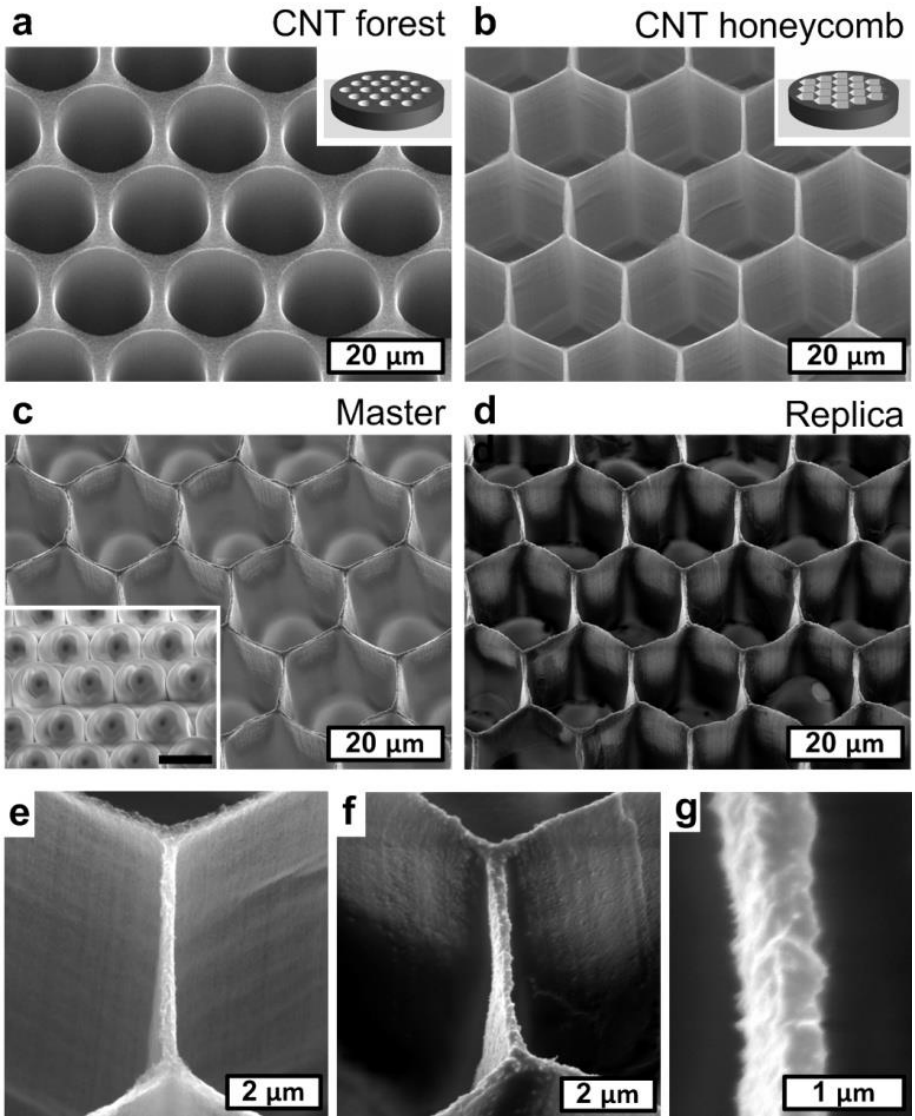

Figure 2-9. Thin-walled hexagonal lattice made by densification and replication of periodic CNT micropattern. (a) CNT forest template, with 20 µm diameter holes at 25 µm center-center spacing; (b) densified CNT pattern; (c) master, with inset showing PDMS negative; (d) replica; (e,f) corresponding wall sections of densified CNT pattern and replica; (g) close-up of replica wall, which is ≈400 nm wide and ≈20 µm tall.

The capability to fabricate and replicate HAR master molds also applies to isolated features as shown in Figure 2-10. Solid micropins (Figure 2-10b) are made using masters from tall CNT pillars with solid cylindrical cross-sections, for example having diameter as small as 5.32 μm and aspect ratio of 22. Hollow microneedles (Figure 2-10c) are made using tall CNT pillars with hollow cylindrical cross-sections, which densify into very thin walls and retain their hollow center. The geometry of the CNT forest and the master formation conditions determine the height, wall thickness, and diameter of the final needle. Processing of shorter hollow cylinders enables replica molding of sloped micro-wells with thin walls, which are shown in Figure 2-10d. This illustrates the unique ability of soft PDMS molds to replicate 3D structures, which we also demonstrate by the replication of bent micropillars (Figure 2-10e). In this case, the bent master structure was made from a CNT pillar that accidentally bent during growth. Indeed, we find that the straightness of the CNT forest microstructures primarily dictates the straightness of the master structures, and analysis of large numbers of pillars indicates that defects from CNT growth are amplified during densification and propagate through the later steps. Nevertheless, the sloped micro-wells and bent pillars shown here indicate that the CNT master molds could be used to fabricate a wider variety of quasi-3D structures, because the flexibility of PDMS allows demolding from sloped and partially re-entrant features.

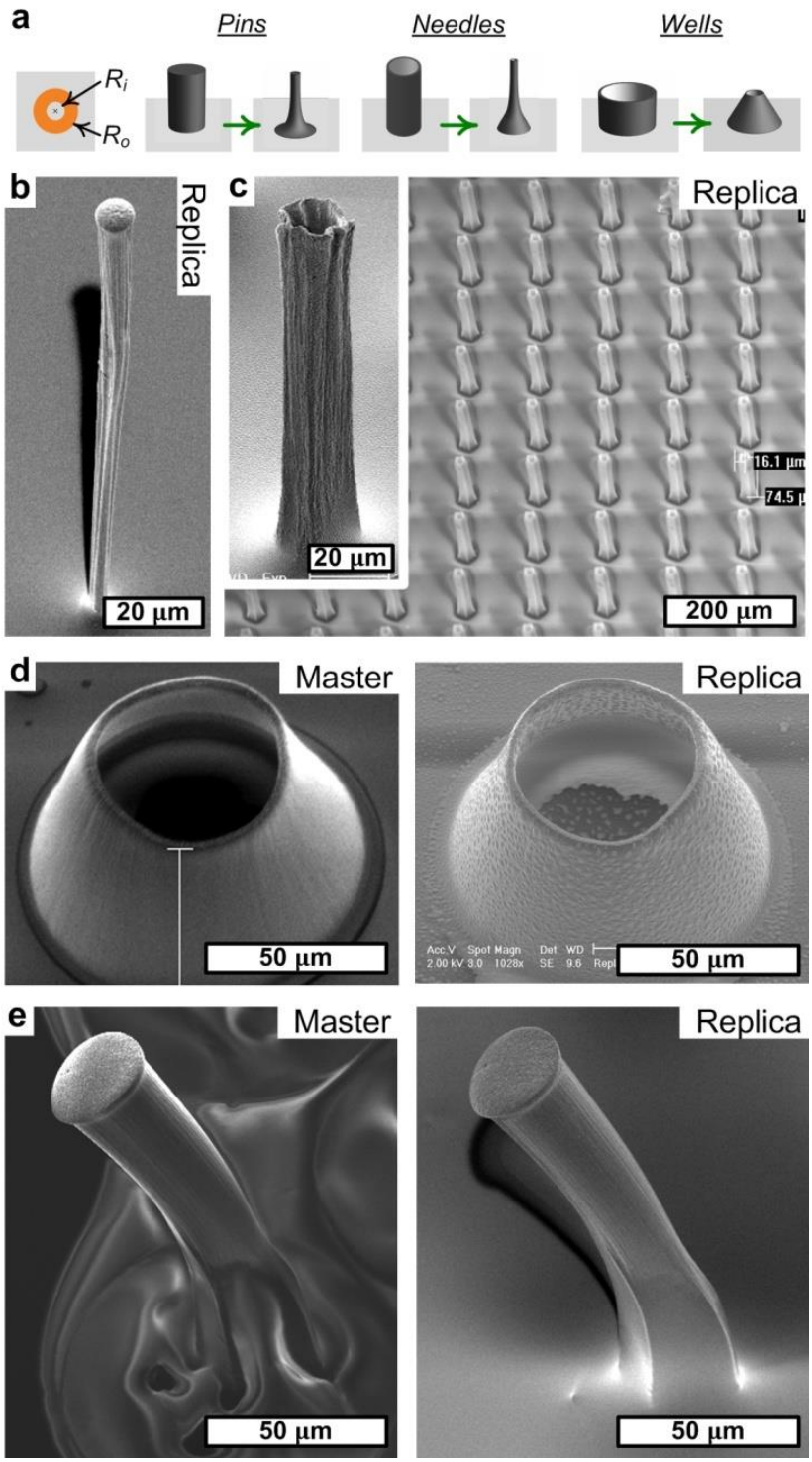

Figure 2-10. Replication of isolated thin-walled and sloped microstructures: (a) formation of CNT pins, needles, and wells by capillary densification of cylindrical CNT micropillars; (b,c) replicas of high-aspect-ratio pins and needles; (d) master and replica of slanted microwell; and (e) master and replica of bent micropillar.

The ability to fabricate and replicate twisted structures is shown in Figure 2-11 [60]. Fabrication of twisted structures is a serious challenge for standard photolithographic techniques.

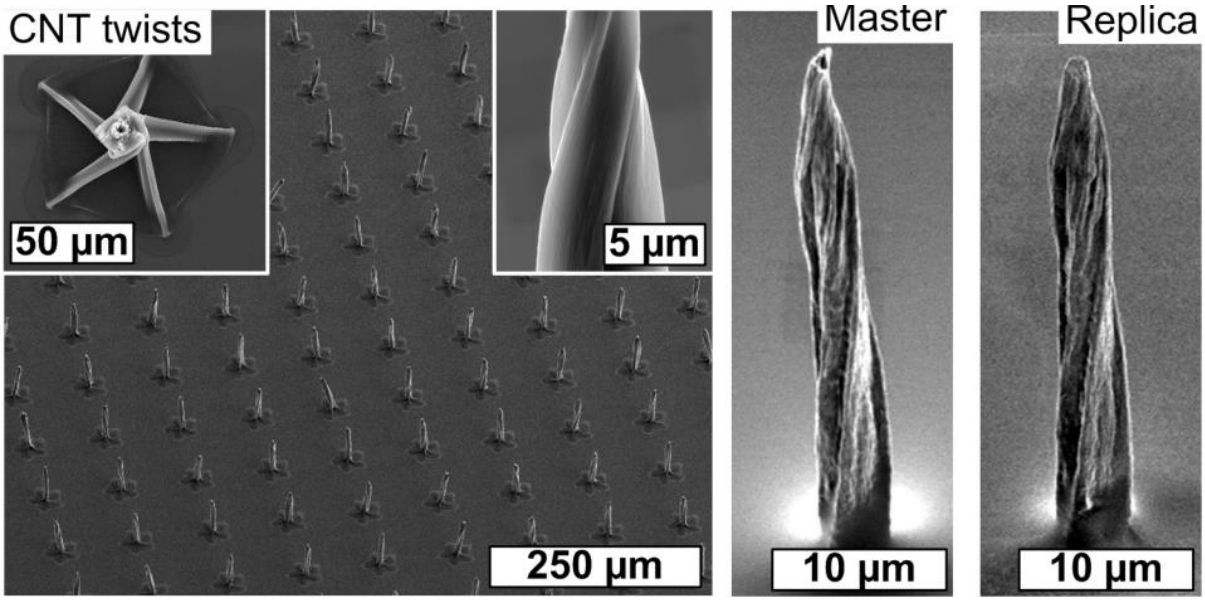

Figure 2-11. Densified twisted CNT micropillars, with master and replica of individual microstructures (image modified from [2]).

Last, as shown in Figure 2-12, we demonstrate casting of replica structures directly onto silicon, glass, and PDMS substrates. For instance, using CNT master molds, high aspect ratio SU-8 structures can be cast directly onto silicon wafers, therefore establishing compatibility with lithographic post-processing. This additional step also provides a means to fabricate novel geometries made using CNT master molds, whose fabrication involves high-temperature CVD, to chips containing Complementary metal–oxide–semiconductor (CMOS) circuitry or other structures requiring low temperature compatibility. One particular application may be micro-needles for integrated drug delivery, which could be integrated with microfluidic delivery and/or sensing and control electronics [80]. These micro-needles could be made from either hollow pillars or slanted wells cast on a flexible material, similar to microstructure arrays in Figure 2-12.

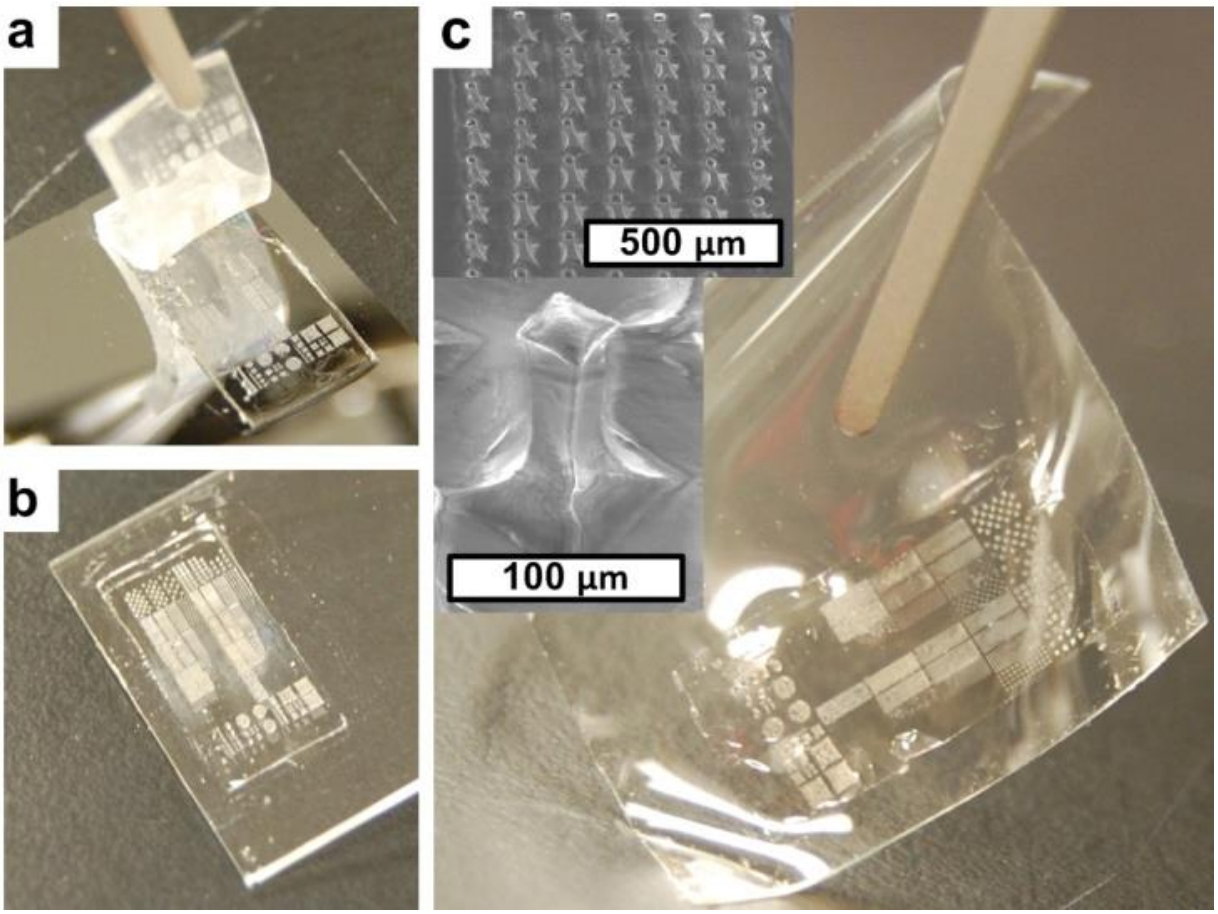

Figure 2-12. Direct casting onto alternative substrates using PDMS negatives made from CNT master molds. (a) Replica on silicon wafer; (b) replica on glass slide; and (c) replica on PDMS membrane, with inset SEM images showing micropillars on the PDMS membrane.

2.4 Conclusion

In conclusion, a versatile process to precisely form heterogeneous CNT microstructures using capillary forming, infiltrate them, and subsequently replicate them in SU-8 is shown. The fabricated nanocomposite CNT microstructures can be used as master molds for large-scale fabrication of polymer microstructures having anisotropic nanoscale textures and high aspect ratios. This novel bottom-up approach to master fabrication contrasts traditional techniques that require specialized deep etching and high-intensity exposure tools, and offers potential advantages in control of feature geometry, heterogeneity, and surface conditions. Further, because CNT master mold technology requires only standard optical lithography and thermal

processing, it could enable cost-effective fabrication of polymer micro devices requiring engineered wetting properties, integrated optical gratings, and controlled roughness for surface-enhanced spectroscopy. Additionally, I have also shown a HAR microwalls, micropins and needles, and 25-fold replication sequence without any damage to the negative or fidelity reduction in the replicas [91]. These devices could be fabricated in SU-8 as shown here, or in a variety of other polymers including PU, PMMA, PDMS, and even low temperature metals. Other CNT growth procedures and structures made from other nanoscale filaments (e.g., inorganic nanowires, biofilaments) could potentially serve as the framework of novel master mold architectures as well.

CHAPTER 3: MECHANICAL PROPERTIES AND ELECTRICAL INTEGRATION OF CNT-POLYMER NANOCOMPOSITE MICROSTRUCTURES

This chapter presents a model of liquid infiltration into and in between CNT microstructures in an effort to better understand the mechanics behind it and allow for control of excess amounts of fluid remaining entrapped. Further, this chapter showcases the stiffness and toughness of CNT microstructures infiltrated with SU-8 and PMMA. CNT-polymer nanocomposites are shown to be significantly stiffer then neat polymers. Lastly, electrical integration of CNT-polymer nanocomposite microstructures is shown.

3.1 Background

This chapter presents the mechanical properties of nanocomposite master structures. The focus is primarily on the stiffness and toughness of the fabricated microstructures as these are important properties lacking from many microstructured and active surfaces, yet are needed for integration into commercial applications. The nanocomposite fabrication is driven by capillary infiltration of SU-8 into the aligned CNTs, while spin-coating provides sufficient centrifugal force to remove excess SU-8 from the spaces in between the microstructures. Along with spin conditions, SU-8 viscosity determines both the expression of the sub-micron texture and the volume fraction of SU-8 in the master mold, which in turn affects the toughness of the master structures. In general, surface roughness is reduced when excess SU-8 remains on the surface of the CNTs. Figure 3-1 shows the impact of spin and time on the texture of infiltrated CNT microstructure along with the liquid level between microstructures. For example, the bottom panel of Figure 3-1a shows that closely spaced microstructures have significant amounts of

liquid trapped between them, while the same microstructures in the bottom panel of Figure 3-1c have no liquid between them at all. A detailed model for infiltration of SU-8 into CNTs is presented below as well as a model for the liquid level between the microstructures. With proper selection of SU-8 swelling during infiltration is kept to a minimum, while good texture replication is ensured.

Additionally, stiffness of infiltrated microstructures with a variety of polymers is shown. The contribution of microstructure size and densification along with infiltration conditions is briefly showcased. Lastly, the potential to use CNTs of the composite for electrical integration is shown.

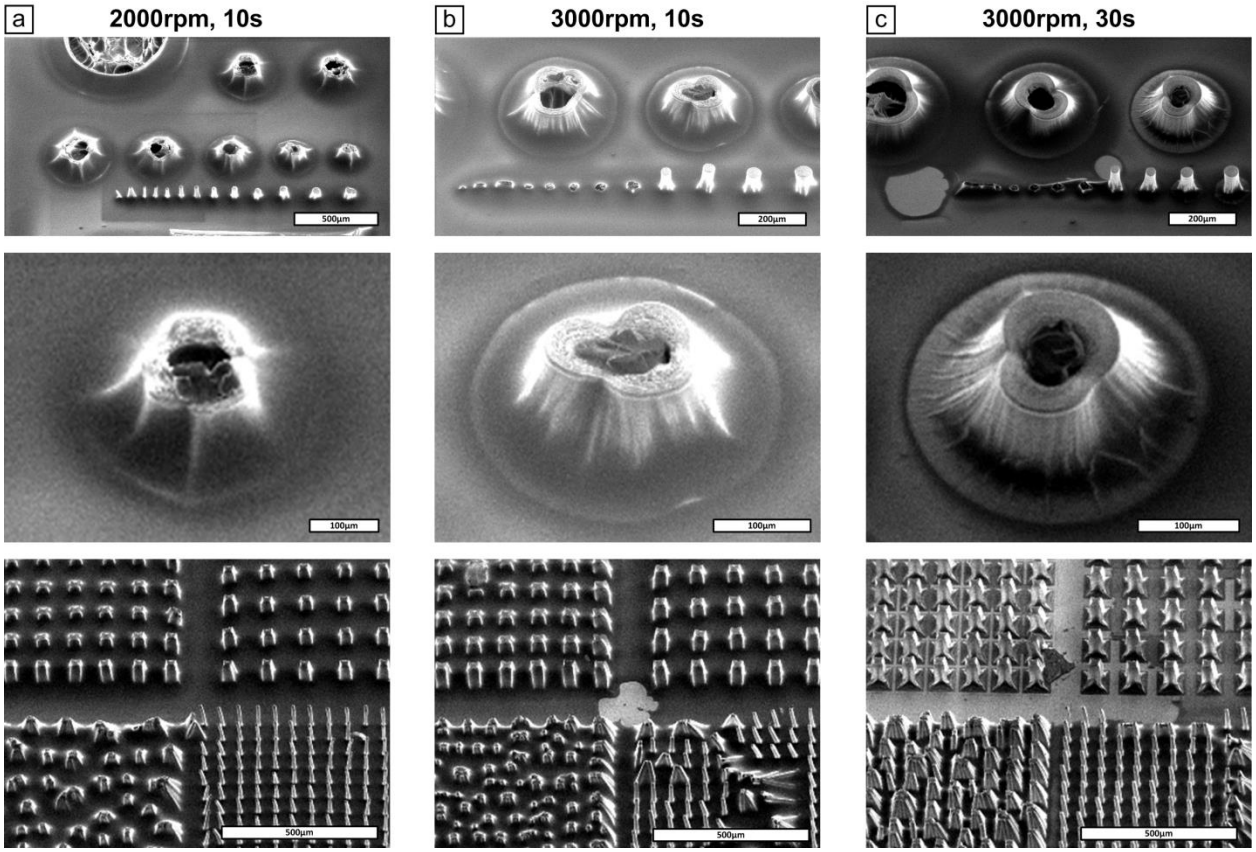

Figure 3-1. Impact of spin conditions on polymer infiltration of CNTs. Slower spin speeds and shorter spin times result in smoother texture and more liquid trapped between microstructures.

3.2 Spin-infiltration model for CNT-polymer composite microstructures

Formation of the nanocomposite master structures is driven by capillary infiltration of SU-8 into the aligned CNTs, while spin-coating provides sufficient centrifugal force to remove SU-8 from the spaces in between the structures. This behavior can be described by an established model of wicking in woven threads [92], wherein a thread is analogous to a CNT micropillar, and the filaments within the thread represent the CNTs within the pillar. If we consider that a CNT pillar is brought into contact with a pool of SU-8, the equilibrium height of SU-8 within the pillar is derived by writing a force balance between the interfacial forces and gravity. This capillary rise height is simplified to

$$h_{eq} = \frac{2\gamma_{SU-8}\cos\theta_c}{R_{mi}\rho g}, \tag{1}$$

where γ_{SU-8} is the surface tension of SU-8, θ_C is the contact angle between SU-8 and CNTs, ρ is the density of SU-8, g is the acceleration due to gravity, and R_{mi} is an equivalent radius calculated using

$$R_{mi} = \sqrt{\frac{\sqrt{3}}{4\pi} d_{spacing}^2 - \frac{d_{fiber}^2}{8}}. \tag{2}$$

Here, $d_{spacing}$ is the average spacing between CNTs within a pillar, and d_{fiber} is the diameter of the CNT pillar. Therefore, the free space in the nanotube network is treated as a set of parallel capillaries of mean radius R_{mi} [92]. Since this approximation works well for a variety of yarns, regardless of their fiber alignment it can be applied to the tortuous CNT network as well. Considering a limiting case of a partially wetting liquid (θ_C <90°) of equation (1), the model predicts that SU-8 can rise into a CNT pillar to several meters in height, if the pillar had such indefinite height. Since the pillars gown are typically not longer than a millimeter the SU-8 can be considered to fully infiltrate these pillars.

This highly favorable wicking behavior enables selective removal of SU-8 from the spaces between the pillars. To capture this behavior in a limiting geometry where the centrifugal forces of spinning are directly aligned with the CNTs, we modify equation (1) to include an effective gravity term ($g_{eff} = g + r\omega^2$). At 3000rpm, SU-8 can be retained in CNTs to centimeter heights, while the rise of SU-8 between pillars is on the order of microns. Further, using Washburn's Law

[93], which relates the infiltration depth of a liquid into a porous material to time and the liquid's viscosity and surface tension, and assuming that SU-8 only wicks into a pillar from the substrate, a 20 µm pillar would be completely infiltrated in 28.6ms. Figure 3-2 shows the results from this model for the liquid level inside a pillar and the liquid height between two pillars.

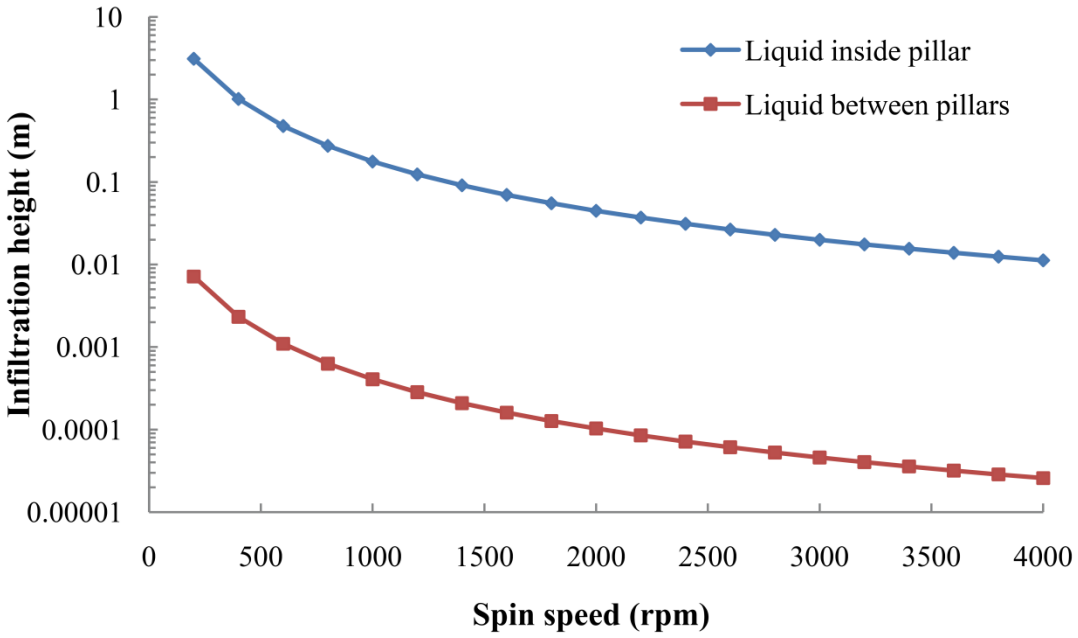

Figure 3-2. Comparison of liquid height inside a pillar and in between pillars spaced 100 µm apart.

Thus, this approach to infiltrating CNT microstructures is effective for self-directed polymer infiltration of isolated CNT microstructures with polymers, and should allow the choice of the SU-8 viscosity without consequence to the infiltration behavior, although the SU-8 viscosity determines both the expression of the sub-micron texture and the volume fraction of SU-8 in the master mold.

From this rudimentary approach it is apparent that the SU-8 height inside the pillar is not the limiting factor in achieving uniform well infiltrated CNT microstructures. Instead more work needs to be devoted to modeling the liquid level between microstructures in an effort to understand the impact of the infiltrating liquid and spinning conditions. To this end a more sophisticated model was built based on a deformable control volume (CV) with pressure contributions from spincoating, where in the centrifugal forces are balanced by the fluid's

viscous forces [94, 95]. Figure 3-3 shows the process phases throughout which the developed model is valid (a) and the pressures and velocity profiles applied to the deformable CV, where P_C is the capillary pressure due to the surface tension, V_1 and V_2 are the average velocities, while P_1 and P_2 are the pressures from the velocity profiles obtained via the spin coating force balance.

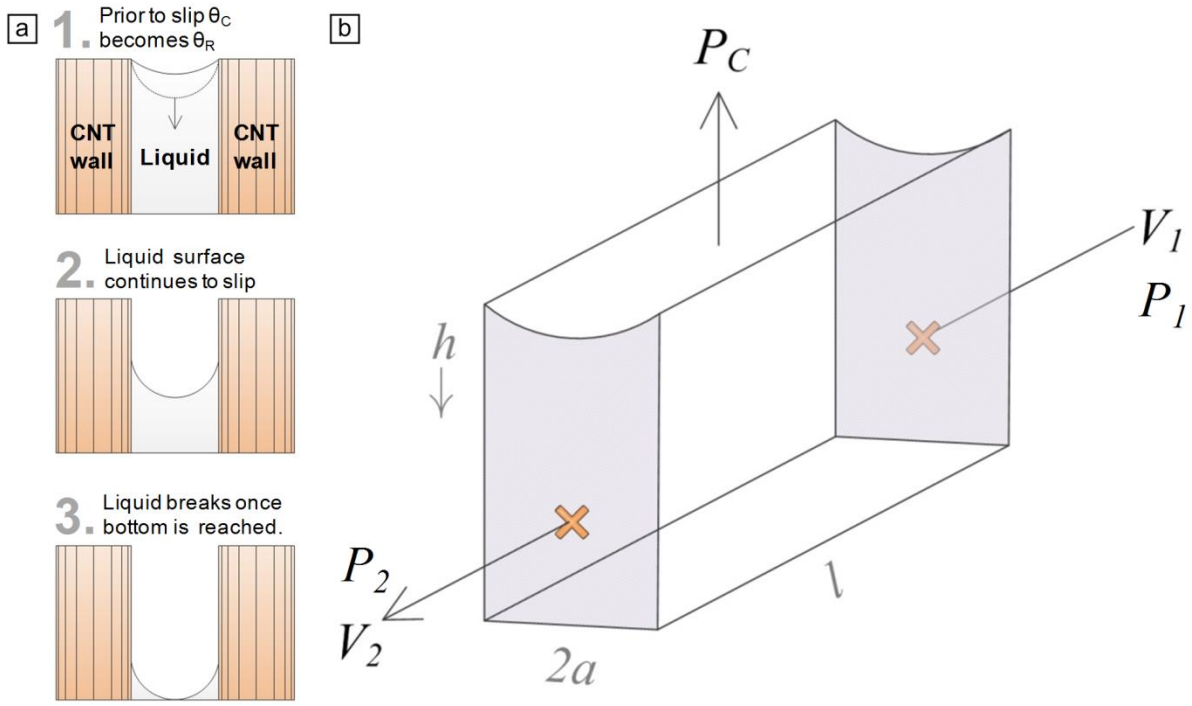

Figure 3-3. Regions through which the model is valid (a) and deformable CV model schematic (b).

In addition to the assumptions and restrictions imposed by both a deformable control volume and a one dimensional (axisymmetric) spincoating model, the model employs a limited number of simplifications and restrictions due to the assumed geometry, including rectangular channels, distance to center of rotation is significantly lager then the size of the microstructure, and that the fluid properties remain largely unchanged through the process.

Simply by applying the centrifugal pressures of the spincoating model and its predicted average velocities along with the capillary pressure and solving for the velocity of the top surface the following general solution is found:

$$\frac{dh}{dt}=\frac{\omega^6\rho^4 a\left(f_1 z^7+f_2\,h\,z^6+f_3 h^2\,z^5+f_4 h^3\,z^4\right)-\eta^2\omega^4\rho^2 a\left(f_5 h\,z^3\right)}{c_1\eta^3\cos\theta_r\gamma+\eta\omega^4\rho^3 a\left(c_2 z^4-c_3\,z^3+c_4 h^2\,z^2\right)}, \tag{3}$$

where ω is the angular velocity, ρ is the density, η is the viscosity, the *f* terms are functions of the distance from the center of the disk (*r*), the *c* terms are constants based on the microstructure dimensions, *a* is half the spacing between microstructures, and *z* is the microstructure height. Equation 3 has been rearranged such that the first set of terms in the numerator quantify the centrifugal contribution, the second set of terms represent the viscous contribution, and the denominator represents the combined capillary and viscous contribution to the change in liquid height. Substituting in the *f* and *c* terms into equation 3 results in

$$\frac{dz}{dt}=\frac{\left(\omega^6\rho^4 a\right)f_1(r,dr)\left(45z^7-315\,h\,z^6+756h^2\,z^5\right)-630\omega^6\rho^4 a\;f_2(r,dr)h^3\,z^4-1120\eta^2\omega^4\rho^2 a\;f_3(r,dr)h\,z^3}{1680\eta^3\cos\theta_r\gamma+\left(70\eta\omega^4\rho^3 a\,r^3\right)\left(z^4-4h\,z^3+4h^2\,z^2\right)}, \tag{4}$$

where $f_1(r,dr)=\left(r^2+r\,dr+\frac{1}{3}dr^2\right)dr$, $f_2(r,dr)=\left(r^2-\frac{2}{3}r\,dr+\frac{1}{3}r\,dr^2+\frac{1}{3}dr\right)dr$, and $f_3(r,dr)=\left(r-\frac{1}{2}dr\right)dr$. Substituting SU-8 2002 properties into equation 4 and solving for the liquid height results in the family of curves shown in Figure 3-4.

Figure 3-4a shows the impact of spin speed on the liquid height between 100µm square microstructures which are separated by a 100µm gaps. These predictions are useful in understanding the tradeoff between spin speed and time. This is relevant for reducing the shear on the CNT microstructures during spincoating while achieving the desirable liquid level. Figure 3-4b shows the liquid height between 100µm square microstructures which are separated by select distances. The shown curves are relevant when creating heterogeneous microstructures in close proximity is desirable and show that the liquid level may vary by orders of magnitude between adjacent structures depending on the spacing. Future developments to the model should add in the pillar geometry, applied fluid shear, and surface adhesion to not only predict the liquid height, but also determine if the structures will be damaged or sheared off the substrate.

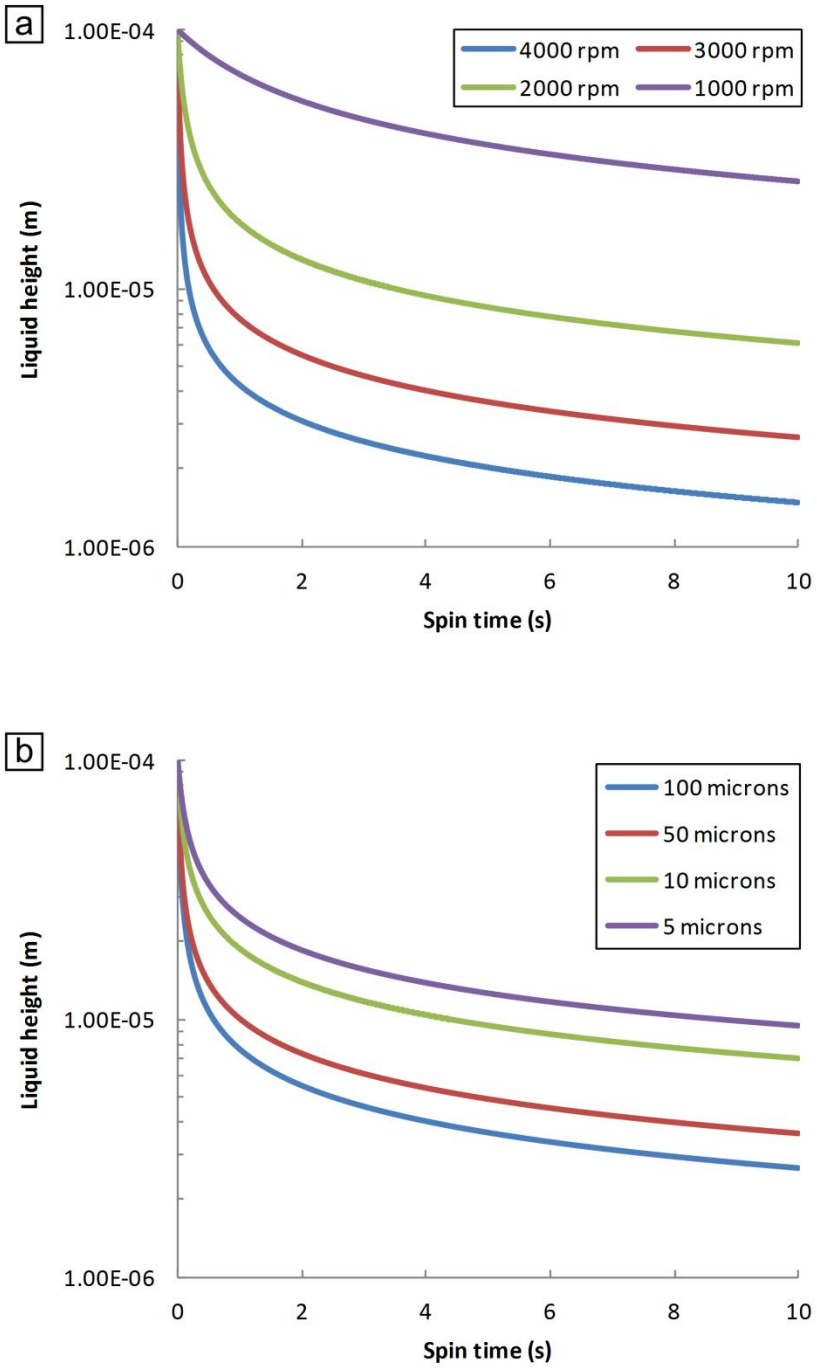

Figure 3-4. SU-8 height between CNT microstructures. Impact of (a) spin speed on liquid height for 100µm large square microstructures separated by a 100µm gap and (b) impact of structure spacing of 100µm large square microstructures at a spin speed of 3000rpm.

3.3 Mechanical properties of CNT-polymer nanocomposite microstructures

Using the procedure detailed in Chapter 3 and the presented model above, CNT microstructures were densified (capillary formed) and infiltrated with a variety of polymers. Compression of these structures was performed using the setup in Figure 3-5a by Dr. Sameh Tawfick [2]. Figure 3-5b shows the stiffness of as grown nanotubes, while Figure 3-5d shows the stress-strain curves for all fabricated microstructures along with their stiffness. The densification of CNTs increases their stiffness by two orders of magnitude to 5GPa, which supports the qualitative observation that as-grown CNT microstructures are not robust enough to be used in replication or infiltration. CNT-SU-8 nanocomposite microstructures are shown to have a stiffness of 18GPa, which is 3.5 times higher than that of SU-8 replicas. Additionally, the stiffness of CNT-PMMA microstructures is 25GPa, which is the most significant increase in stiffness as bulk PMMA has a stiffness of 3GPa.

As discussed in section 1.3, the increase in stiffness is expected as many other groups have shown an increase in mechanical performance of polymers with the addition of small amounts of nanotubes [35-39]. However, in most cases this consists of addition of bulk CNT powders to polymer melts, which are then extruded or spun. Many composites show a sharp degradation in mechanical properties once a large volume fraction of CNTs have been added. This degradation is due to CNTs beginning to phase separate and form microscale domains, which are effectively microscale stress concentrations responsible for the lowering of composite strength [51, 52]. The advantage of forming engineered nanocomposites is that the CNT morphology can be controlled to ensure no phase separation takes place. In the case of microstructures this is easily accomplished, but scaling this up may present challenges. A potential approach to address these challenges is to assemble larger structures from infiltrated microstructures. Infiltrated microstructures could be stripped from the surface, suspended in a solution and then cast or pressed into a mold.

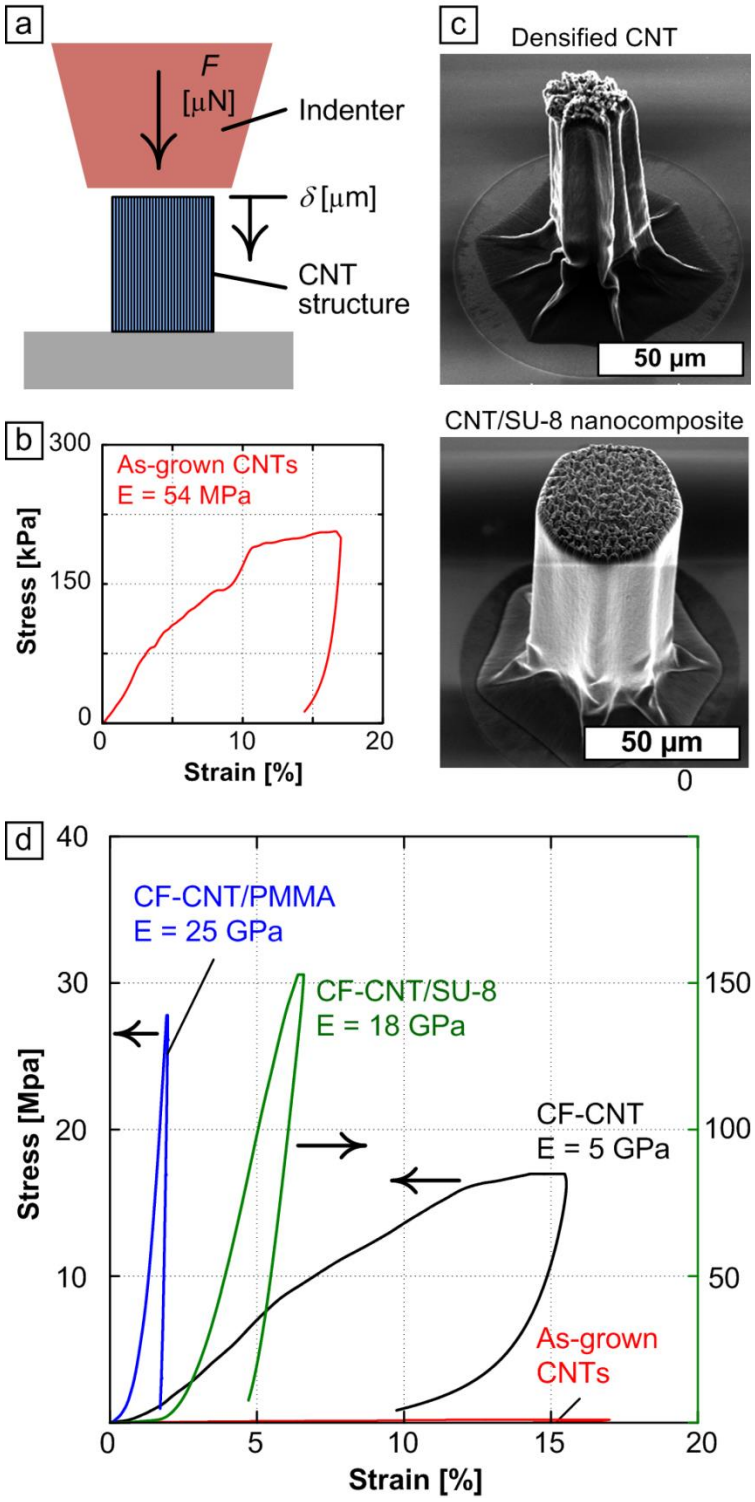

Figure 3-5. Stress-strain curves of various CNT-polymer composite microstructures. (a) Indentation setup, (b) Stress-strain curve of grown forest, (c) sample microstructures, and (d) Compression of CNT-polymer nanocomposite microstructures. Figure adapted from ref [2]. Data collected by Dr. Sameh Tawfick.

To further study the stiffness of these CNT-polymer composites, CNT pillars of various sizes were grown, densified, and infiltrated with SU-8 2002. During densification pillars with a 300µm densified to have an 84µm, while pillars with a 100µm densified to have a 34µm. The reduction in pillar cross section corresponds an increase in CNT density. CNT-SU-8 microstructures with a diameter of 84 µm and 34 µm have an increased density of 13.3 and 8.7 times, respectively. Since the as grown forests have an approximate volume fraction of 1% CNTs, this increase in density is impressive. Additionally, since the structures are not observed to swell, they have a 13% and 8% CNT volume content. This large volume fraction of CNTs would be expected to reduce the properties of the fabricated composites if they were fabricated using bulk mixing, but because the composites are structured from a nanoscale up a significant increase in performance is observed.

Figure 3-6 shows (a-b) sample microstructures, (c) the stiffness for 84µm diameter pillars, and (d) the stiffness for 34µm pillars. Regardless of the spin time the large infiltrated microstructures, which were spun at 3000rpm, are stiffer than the densified CNTs, but softer then the SU-8. Large microstructures, which were spun at 1000rpm, are stiffener than both SU-8 and densified CNTs microstructures. The stiffness of these composites is 8.77 GPa, where as SU-8 has a stiffness of 4.95GPa. Surprisingly, the smaller infiltrated CNT microstructures are stiffer at 13.53 GPa even though they have a smaller CNT content and were spun at 3000rpm. This suggests that the processing conditions have a different impact depending on the size of the structure in addition to determining its surface roughness and trapped liquid level. For comparison, microstructures infiltrated with the dip method developed by Garcia et al [96] had stiffness of 11GPa; however, their CNT volume fraction was on the order of 2%.

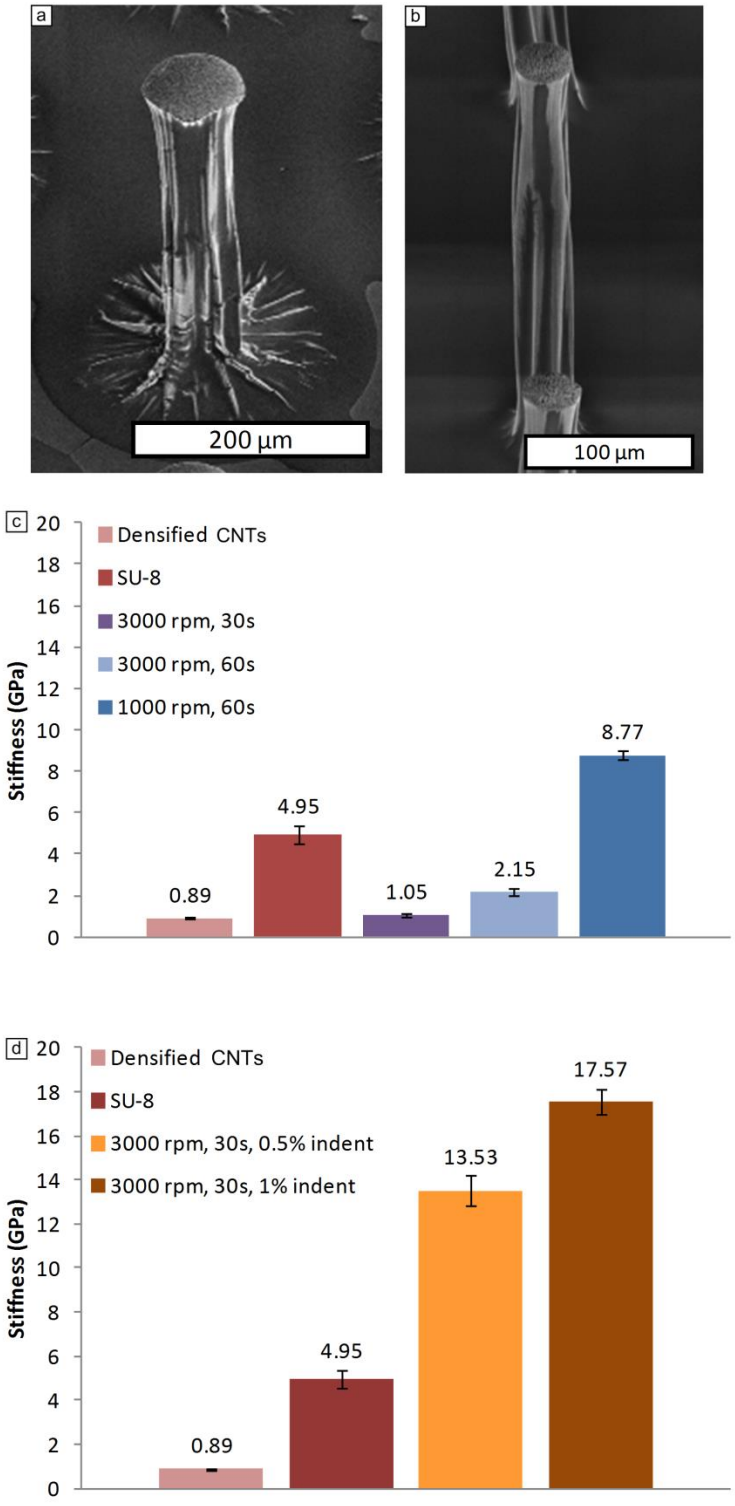

Figure 3-6. Impact on SU-8 processing conditions on nanocomposite microstructure stiffness. (a-b) Sample infiltrated microstructures. Stiffness for circular micropillars with (c) 84µm and (d) 34µm diameter. Data collected by Anna Brieland-Shoultz.

3.4 Electrical integration of CNT-polymer nanocomposites

CNT microstructures can be infiltrated with a hydrogel monomer which is then polymerized, using a similar procedure to the one detailed in Chapter 2. These composite microstructures swell anisotropically when exposed to a stimulus which swells the hydrogel and can be used as microactuators or sensors. Figure 3-7 shows SEMs of the microwells swelling with increasing humidity as well as finite element analysis (FEA) simulations capturing the swelling behavior. The CNT-hydrogel microwells were fabricated by Dr. Michael De Volder [97]

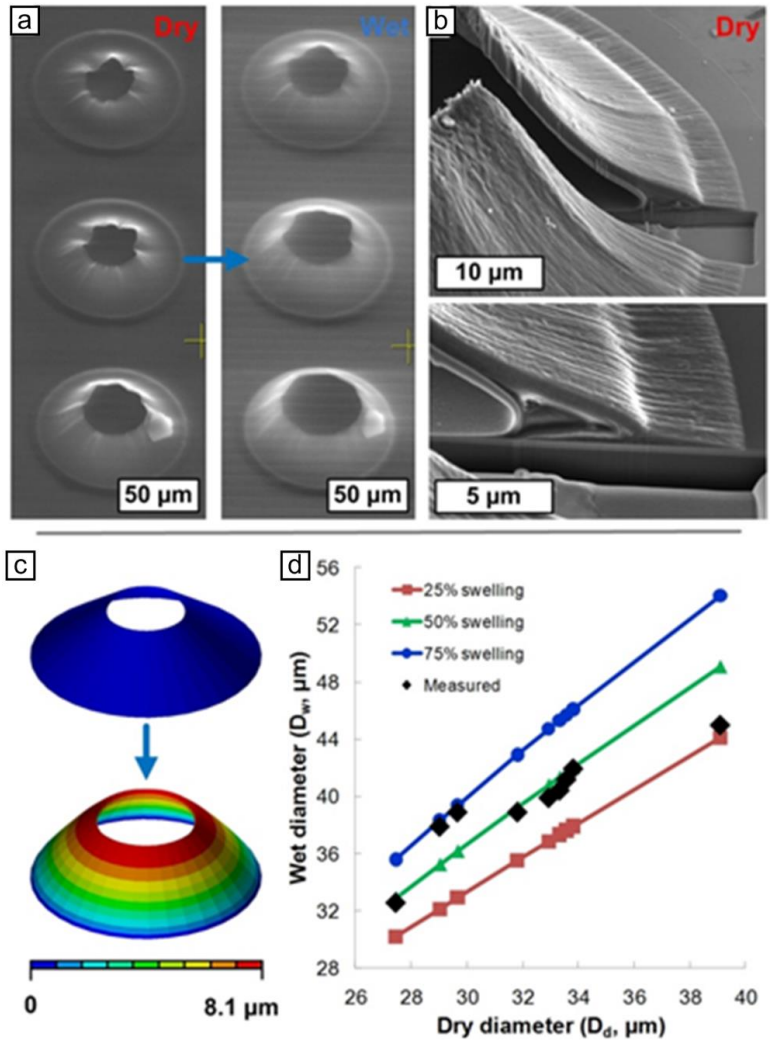

Figure 3-7. Actuating CNT-hydrogel microwells. (a) CNT-hydrogel wells expand upon wetting, (b) cross section view of microwell, and (c-d) FEA simulations of CNT-hydrogel microwell nanocomposite. Figure taken from [97], wells created by Dr. Michael De Volder.

As these actuators swell the resistance within the CNT networks changes. This was employed to fabricate the sensors shown in Figure 3-8. An as-grown CNT pillar on TiN electrodes is shown in Figure 3-8a, while Figure 3-8b shows the same microstructure infiltrated with polyhydroxyethylmethacrylate (pHEMA). A functional sensor is show in Figure 3-8c. Vertically running parallel electrodes are connected by CNT-hydrogel composite walls.

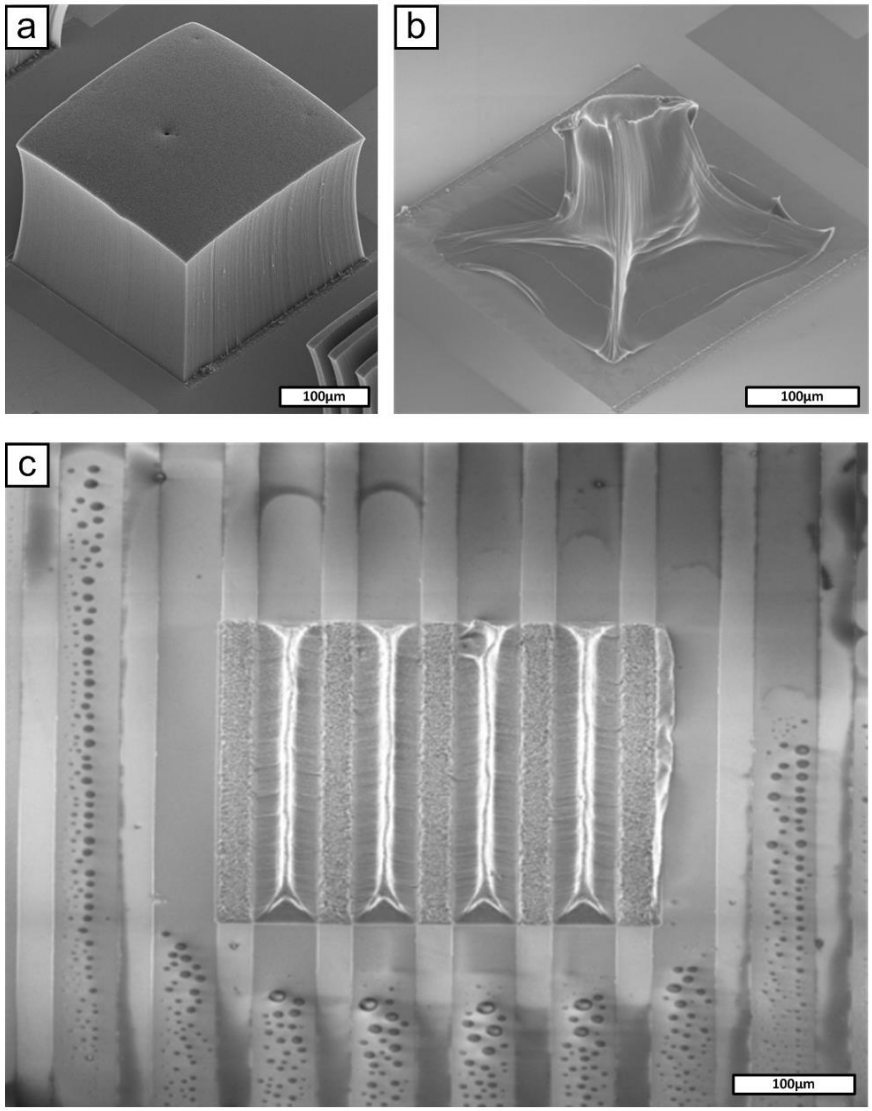

Figure 3-8. CNT-hydrogel sensor integration. (a) As-grown CNTs on TiN electrodes, (b) infiltration with hydrogel causes densification, and (c) CNT-hydrogel sensor array.

The transduced electrical signal upon wetting is shown in Figure 3-9a, while Figure 3-9b shows the resistance change upon a temperature driven pHEMA phase transition.

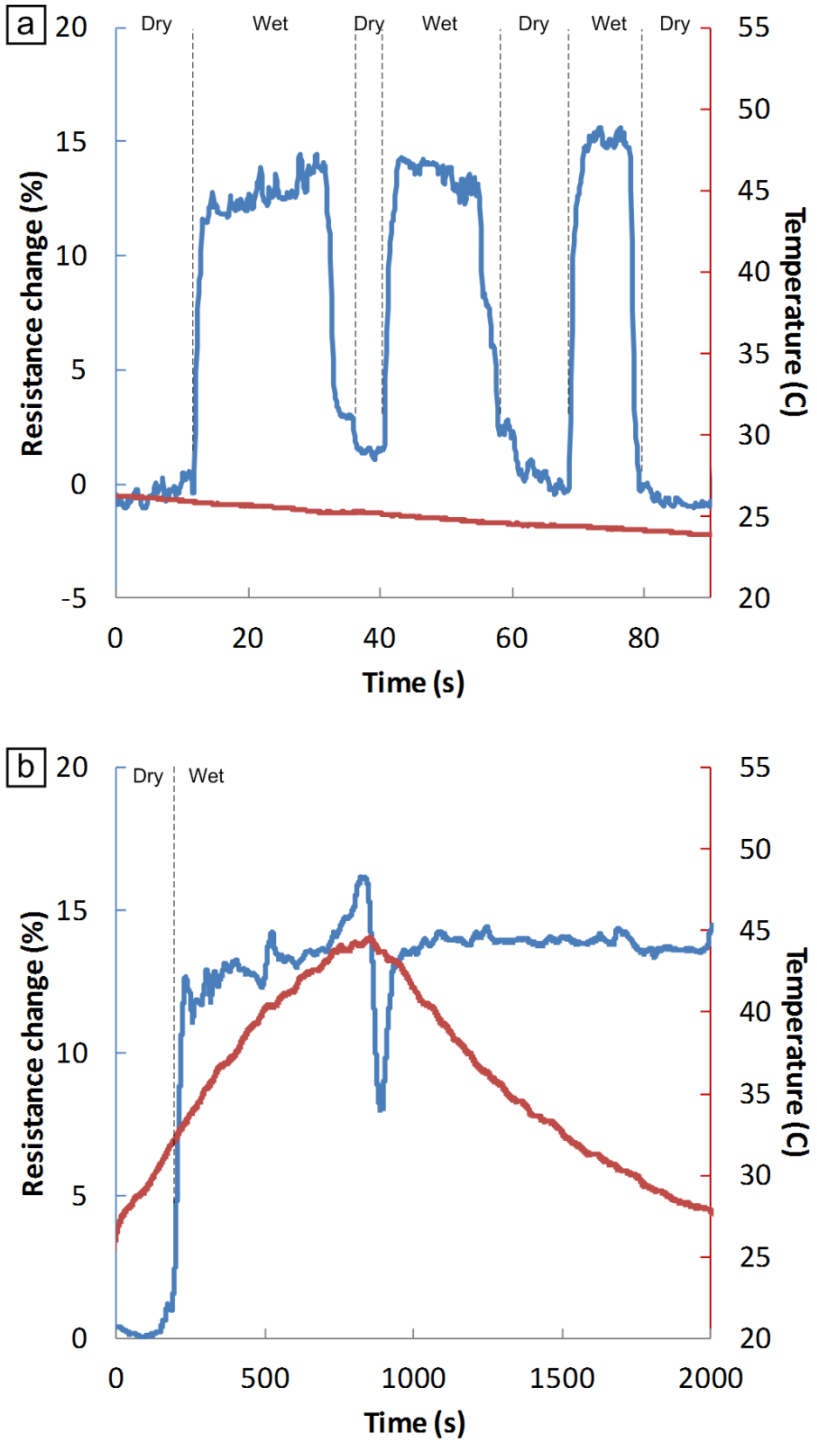

Figure 3-9. Resistance change of CNT-hydrogel sensor array upon wetting (a) and upon temperature change (b).

The change in resistance is comparable to results shown in literature [98]. However, due to the significantly smaller size of the sensor shown in Figure 3-8, the response in Figure 3-9 occurs

at least two orders of magnitude faster. Since the pHEMA undergoes a phase transition at 44ºC and becomes hydrophobic, expelling the absorbed water, the fabricated sensors are also temperature sensitive. This temperature sensitivity does not create a useful temperature sensor, but rather showcases the ability to use the hydrogel to transduce another signal besides it wetted state. This is useful as hydrogels are sensitive to a variety of environmental stimuli, including pH [25], ion concentration [25], temperature [26], solvent composition [26], and electric potential [27], all of which would be transduced using the fabricated sensor.

3.5 Conclusion

This chapter presented an infiltration model for polymer infiltration of CNT microstructure to allow for processing at slowest spin speeds in an attempt to reduce microstructure delimitation or warping during processing. It is shown that creating heterogeneous microstructures in close proximity inevitably results in varying amounts of liquid remaining between them. Improvements in stiffness of infiltrated structures were also shown for a variety of polymers. . CNT-SU-8 nanocomposite microstructures are 3.5 times stiffer then SU-8, while CNT-PMMA nanocomposite microstructures are 8.3 times stiffer then PMMA. Lastly, electrical integration of the CNTs is shown in CNT-hydrogel microstructures. The CNTs to serve as embedded sensors to transduce the microactuator motion. In this case capturing wetting behavior and changes in temperature.

CHAPTER 4: FABRICATION AND MECHANICAL PROPERTIES OF CNT-PARAFFIN NANOCOMPOSITE SHEET ACTUATORS

Significant portions of this chapter with additional editing were published in: D. Copic, A.J. Hart, 19th International Conference on Composite Materials, Montreal, Canada, 2013, ref [61].

4.1 Background

Among active materials, paraffin wax is attractive for use in actuator devices due to its large stroke and simultaneous large stress output [99], high energy density [100, 101], and, depending on its thermal mass, relatively fast actuation. For example, at 150°C paraffin undergoes a volumetric expansion of 20% under 200MPa [100] and has an energy density similar to that of shape memory alloys.

Paraffin wax has previously been used in microscale pumps [102], valves [103], and actuators [104]. However, miniaturizing these designs requires multiple soft lithography steps to fabricate the necessary sealed microfluidic channels, reservoirs, and heaters to build the actuation system. The complexity of integration of paraffin microactuators and the limited geometries that have been employed thus far have perhaps prevented their wider adoption as elements of micro-scale active material systems.

Moreover, it is challenging to integrate paraffin as an actuator because confinement of the paraffin is necessary to extract its volume change into useful work. Recently, Lima et al. confined paraffin wax inside CNT yarns. The strong wetting of CNTs by paraffin prevented it from leaking out of the CNT network upon heating, instead causing the CNT yarn to expand radially. The yarn's twisted configuration coupled the radial expansion to a 8% contraction in length [105]. Their actuator exhibited excellent tensile performance and was actuated electrically, chemically, and photonically.

However, micro-scale actuation using CNT-paraffin composites have not been explored. Previously, the interaction between anisotropic mechanical properties of CNT forest microstructures and an isotropic active polymer, such as a hydrogel, was shown [97]. A high-stroke film actuator is fabricated and tested using paraffin-infiltrated aligned CNT forests, which are pre-compressed to enable expansion of paraffin to cause directed expansion of the nanocomposite sheet. The CNT-paraffin films expand reversibly by 20% in the vertical direction upon heating to 175°C, and this performance is repeatable over several cycles.

4.2 Fabrication process

First, CNT forests were grown using CVD from a thin film catalyst (1nm Fe supported on 10nm Al_2O_3) deposited by sputtering on a SiO_2/Si wafer. The catalyst-coated substrate was annealed in a 400:100 sccm H_2:He gas mixture at 775°C for 20 minutes, and then exposed to a 400:100:100 sccm H_2:He:C_2H_4 mixture for 2-3 minutes for CNT growth. Rapid cooling of the CNT forest in the growth atmosphere is crucial for strong adhesion to the substrate, which prevents the detachment of the film the substrate during subsequent processing. A detailed description of the catalyst patterning and CVD CNT growth procedure is given in Chapter 2.

Schematics of the fabrication process along with the experimental setup used for both sample fabrication and mechanical characterization are shown in Figure 4-1. To fabricate a CNT-paraffin film, a CNT forest (attached to the growth substrate) was placed on a hot plate at 100°C and compressed by a desired amount (typically 10-50% of the initial height) using a vertical precision actuator. This is crucial since it allows a modulation of CNT stiffness via modification of the forest morphology on a nanoscale. As the forest is compressed the CNTs bend/buckle and make contact with adjacent CNTs forming new junctions. While maintaining this temperature, molten paraffin wax was added to the silicon substrate, and promptly wicked into the CNT forest, which was constrained from expanding vertically upon infiltration. Constant load was applied during cooling, which varies based on the CNT growth batch, but is generally between 10 MPa and 15 MPa. This is the load required to compress a forest to 50% of its height. Further shrinkage along the forest takes place during cooling. Last, the sample was placed on a spin coater and exposed to 75mW/cm^2 of ultra violet (UV) light for 35 seconds prior to spin coating. Excess paraffin was then spun away at 3000 rpm for 30 seconds while the UV light was

maintained. The light is absorbed by the CNTs and converted to heat, causing melting of the paraffin prior to and during spin coating.

All sample fabrication and indentation experiments were performed using a single axis precision actuator with both PID position and load control, which is driven using a voice coil actuator. The motion was measured using a linear optical encoder, while the load was measured using a S-beam load cell (Futek).

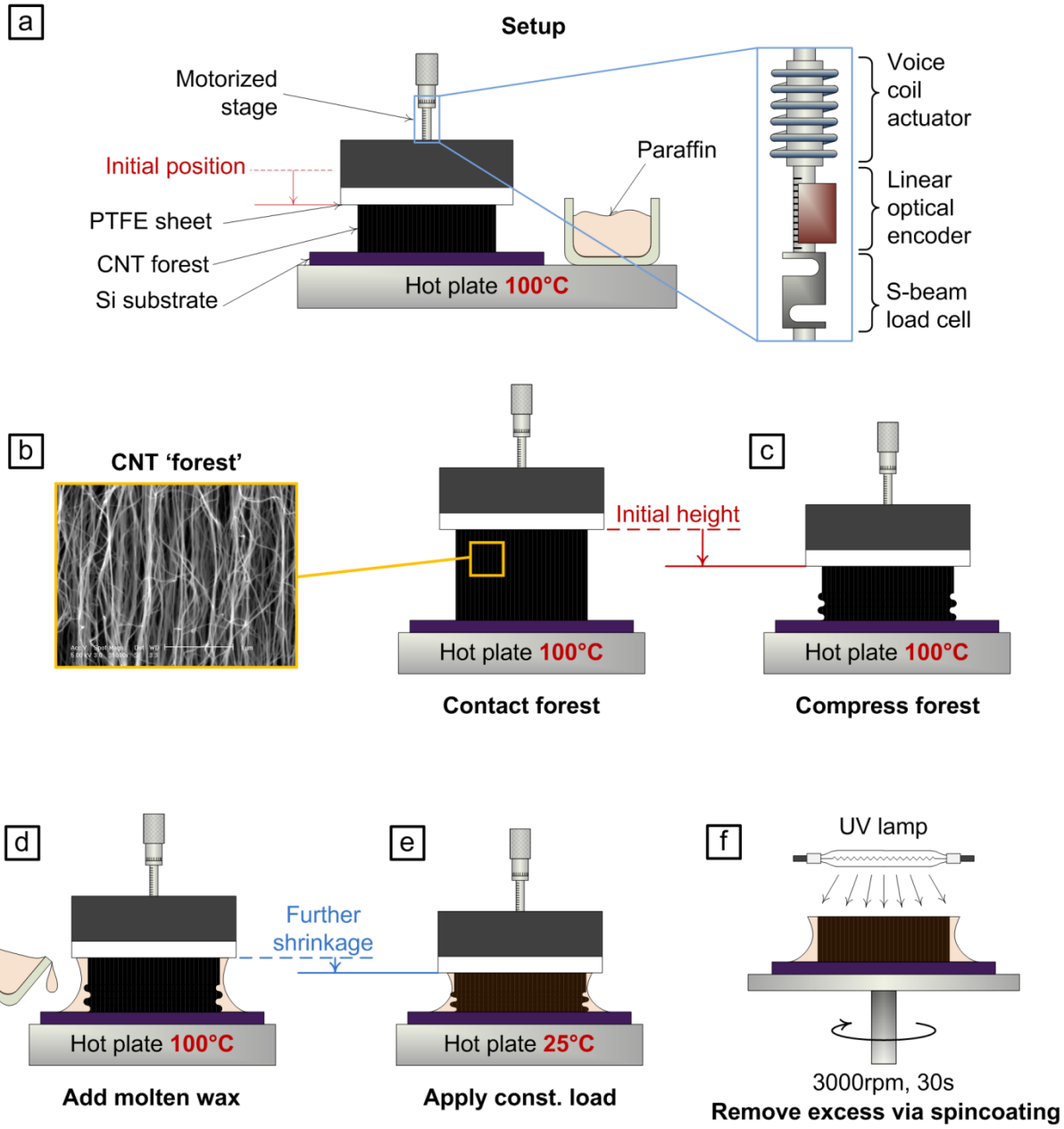

Figure 4-1. CNT-paraffin thin film fabrication process. (a) Setup used in actuator fabrication and testing. CNT forest compression is performed using a stage with displacement PID control. (b)

Contact is made with the top of the forest. (c) CNTs are pre-buckled. (d)Molten wax is poured and rapidly wicks in the CNT forest. (e) Further shrinkage of the actuator takes place during cooling under constant load. (f) Spin coating is done under UV to remove excess wax from composite.

4.3 CNT-paraffin actuator performance

Figure 4-2a shows a mirrored optical image of the CNT-paraffin actuator side view at 25°C and extended by 17% at 150°C. The CNT-paraffin actuators were instrumented with thermocouples attached to the top surface of the silicon CNT substrates to monitor temperature during actuation. They were then placed on a PI controlled hotplate and the position of their top surface was monitored. The optics setup used for this consisted of a collimated light source backlighting the sample, while the light was collected using a telecentric lens. This optical setup produces a high contrast image with an orthographic view, eliminating any contribution of perspective to the measurement of the actuator strain. The high contrast in the image allows for precise real time determination of the thermal strain.

Three consecutive cycles of a CNT-paraffin actuator under no load are shown in Figure 4-2b. The thermal strain increases rapidly after the paraffin melts, and then increases linearly as the wax undergoes linear thermal expansion after melting. The expected melting point for the paraffin used in these samples is 53-57°C. Some thermal expansion is also observed before the onset of melting. There is good agreement between the thermally generated strain over the three cycles with the exception of the initial heating.

The isotropic thermal expansion of the paraffin combined with the anisotropic CNT mechanical properties results in anisotropic thermal expansion along the film thickness. At elevated temperatures, the strong surface energy of the molten paraffin wax prevents it from flowing out of the CNT forest and instead the increasing pressure of the molten wax does work against the stiffness of the forest, causing the material to expand. Strong adhesion between the CNT forest and its substrate prevent the forest from expanding laterally and from shearing from its support substrate. As a result, the motion of the actuator, powered by the volumetric expansion of the melting paraffin wax, is restricted to an extension along the CNTs. Since the CNTs have anisotropic mechanical properties, the exhibited actuation is also anisotropic.

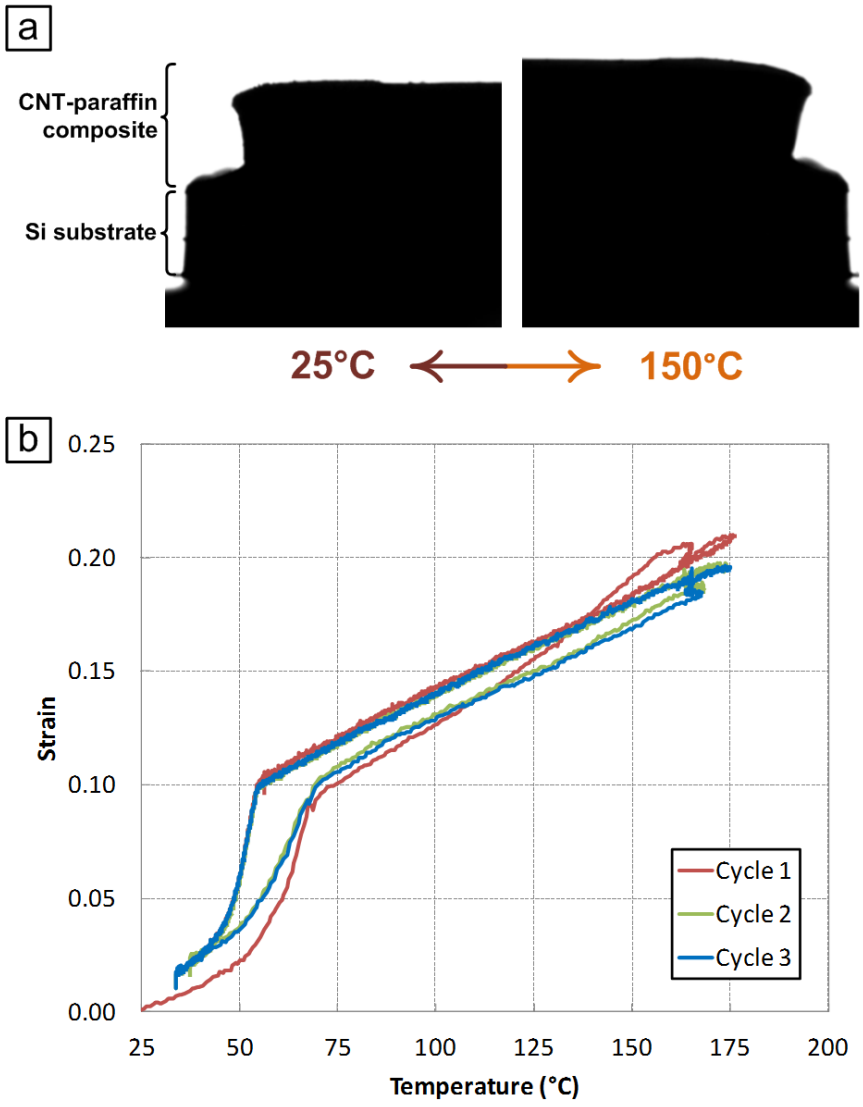

Figure 4-2. Thermally generated strain of the CNT-paraffin actuator under no load. Mirrored images of actuator cross section at 25°C (left) and at 150°C (right), showing a strain of 17%. (b) Thermal strain of CNT-paraffin actuator versus temperature, for three identical sequential heat-cool cycles.

SEM images of a CNT forest crushed to 50% of its original height before paraffin infiltration are shown in Figure 4-3a and Figure 4-3b (close-up). The characteristic wavelike buckling of vertically compressed CNTs near the substrate is observed, as previously shown by Cao *et al.* [106] and others. However, unlike Cao *et al.* the buckling in the base of the forest is not recovered when the load is removed, because the induced elastic deformation energy is overcome by the van der Walls forces between additional CNT contacts created during compression of the forest. Furthermore, Cao has shown that the morphology of his forests

changes based on the number of loading cycles. Our forest morphology after a single indentation resembles that of Cao's forests after 200 indentations. This is not surprising, since the forests he grew likely have significantly different mechanical properties then the ones grown using the procedure detailed in chapter 2. Additionally, Cao performed up to 2000 indentations, resulting in a forest with significantly shaper bends in the wave-like structure. This evolution of forest morphology over thousands of cycles may have implication for the performance of the fabricated CNT-paraffin actuator.

The forest shown in Figure 4-3a expands vertically during infiltration, as shown in Figure 4-3c. Figure 4-3d shows a SEM image close-up of the previously buckled region significantly expanded in height after infiltration. The expansion upon infiltration varies between forests grown in different batches, but generally is between 80% and 100%. The paraffin has fully infiltrated the CNTs, as indicated by the contrast and charging of the SEM image. Forests that are allowed to expand during paraffin infiltration develop large cracks on their top surface upon cooling after spincoating instead of undergoing a retraction in height. During cooling the wax exerts compressive forces on the forests. Whether the forests will compress axial, as desired for the actuators, or laterally depends on its relative stiffness. Pre-buckling of the forest lowers its axial stiffness relative to its lateral stiffness and the cooling wax compress it axially. On the other hand, the crack formation in unconstrained forests is caused by local capillary aggregation of CNTs as the excess paraffin is spun out of the forest. During heating, cracked actuators do not have significant vertical strain, instead the cracks were observed to shrink, which may have interesting applications. These applications however are not related to actuators, since cracked forests are unable to do large amounts of useful work. Forests that were restrained during infiltration have significantly less paraffin content prior to spin-coating and do not crack upon subsequent cooling. Only forests that were constrained vertically during infiltration result in functional actuators.

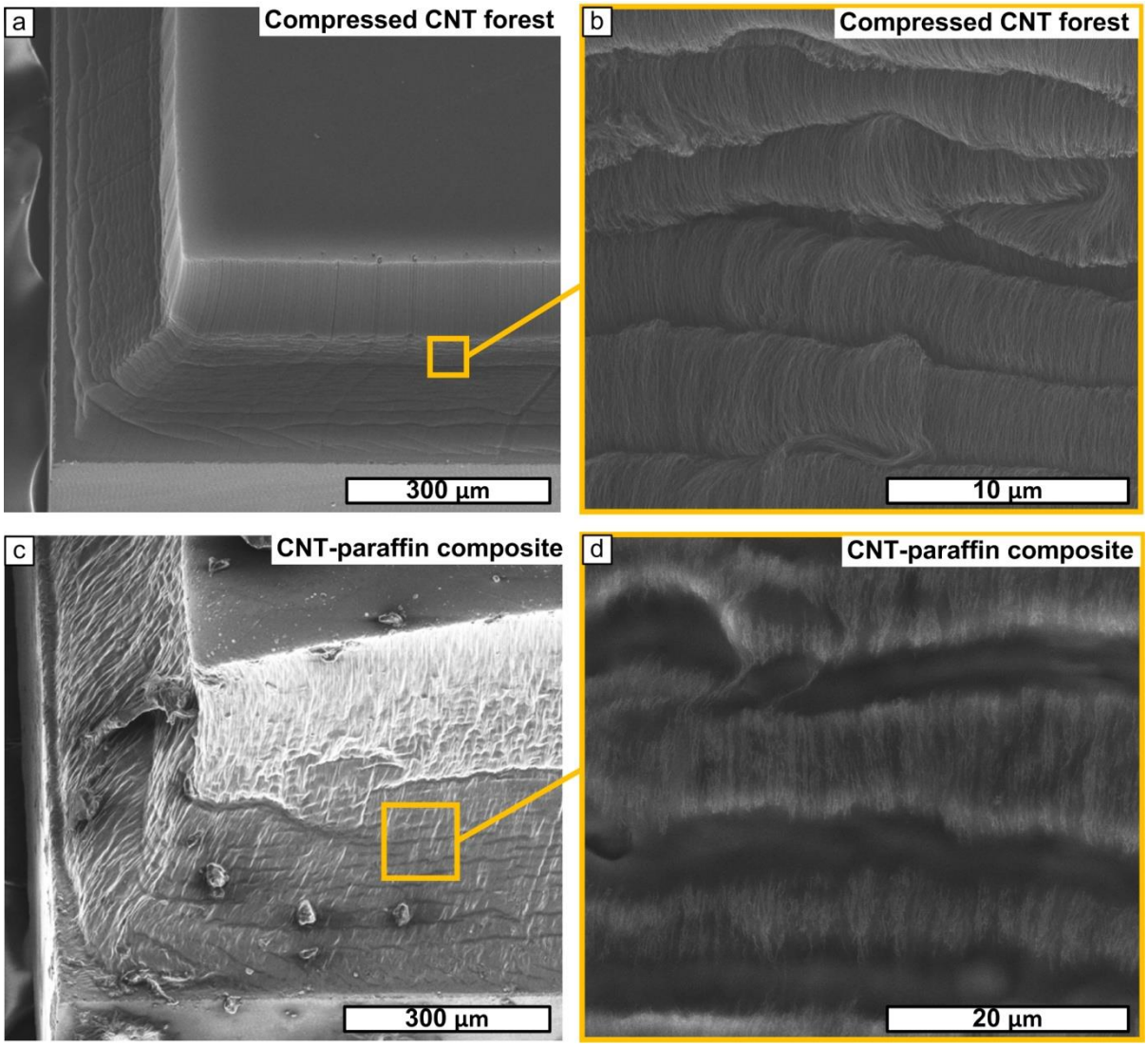

Figure 4-3. SEM image of crushed and infiltrated forest. Pre-buckled forest (a) and close up of buckled region (b). SEM image of CNT-paraffin composite (c), which was not constrained during infiltration and close up of buckled region (d).

The dependence of the thermally generated strain on the amount of forest compression before/during paraffin infiltration is shown in Figure 4-4a. All of these CNT-paraffin actuators were tested by applying a constant load while in contact with the top surface and then heating. The thermal strain curves of all three samples can be considered to have three regions: (1) low thermal strain below the melting point, (2) rapid expansion during melting, and (3) further expansion driven by the increased pressure of the molten paraffin wax. As previously mentioned, forests not constrained during infiltration do not extend vertically upon heating. A larger forest compression results in larger thermally generated strain. In some cases, the thermal strain curve

for the forest compressed by 10% deviates significantly from the linear thermal expansion of pure paraffin and that of other shown actuators at elevated temperatures. This is due to the forest reaching full recovery to its pre-compressed height at about 150°C.

It is interesting to note the nonlinear impact of the compression on the observed thermal strain in Figure 4-4. As the pre-compression increases from 10% to 25%, an increase in the thermally generated strain of less than two times is observed. On the other hand, as the pre-compression increases from 25% to 50%, significantly more than two times more thermal strain is observed.

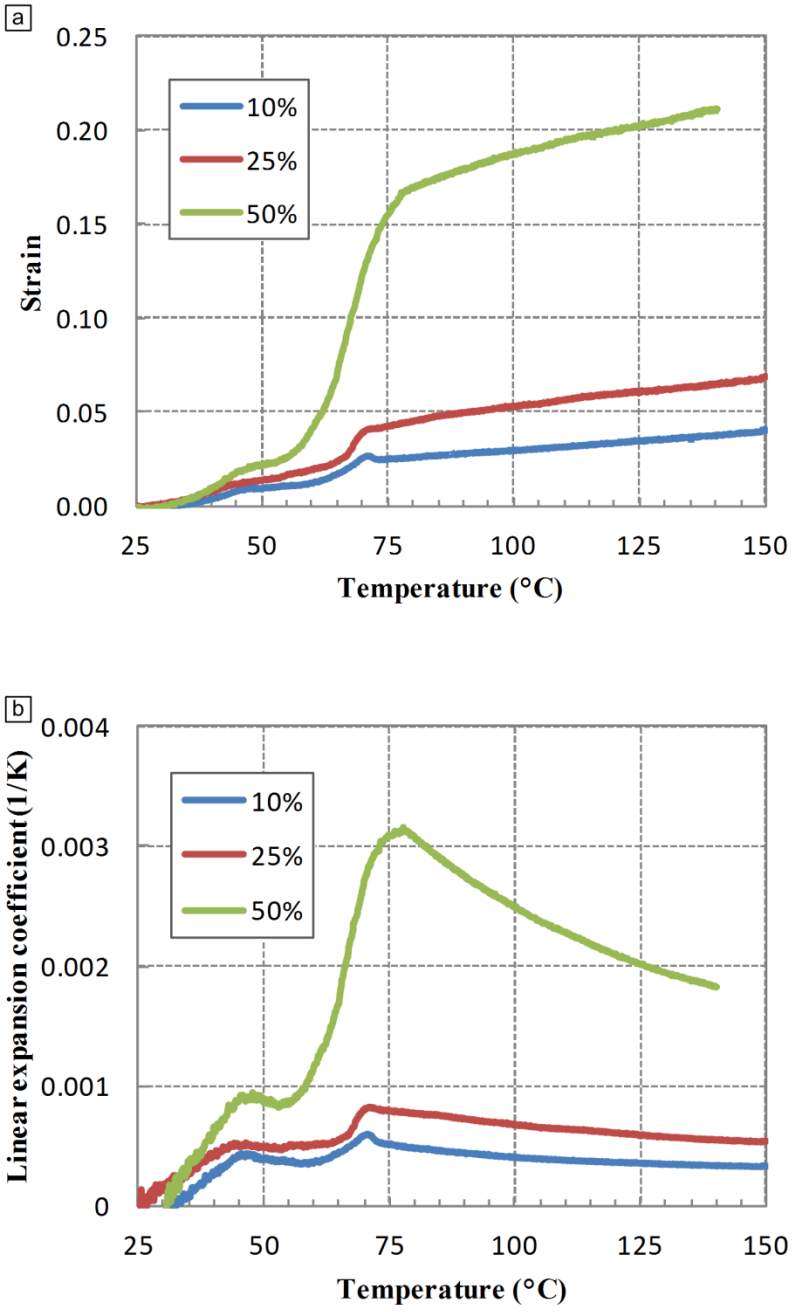

Figure 4-4. Impact of pre-buckling on thermally generated strain. (a) Comparison of the impact of pre-infiltration forest compression to the thermally generated strain. (b) Linear thermal expansion coefficient for each sample.

Thermal strain curves for a sample under constant load are shown in Figure 4-5. Maximum strains of 26% are reached at 148°C under 0.01kPa. The stop load for the actuator is between 1kPa and 10 kPa. Surprisingly, the strains reached under load surpass those reached in the no

load condition. This is due to run-to-run variation in the density of CNT forests [84], which influence their mechanical properties and therefore influence the actuator performance. An increase in density is expected to correspond to a larger actuator stiffness at the expense of lowered maximum strain. This tradeoff is due to the work density of the process powering the shape change, in this case the phase transition and thermal expansion of paraffin, remaining largely unaltered by the CNT density. An increase in CNT density would change the spacing between the CNTs which would result in an increase in the capillary pressure of the wax.

The actuators tested under constant load as low as 0.1 kPa exhibit a more gradual expansion after the wax melting point, as compared to the actuator under no load. Additionally, actuators under load exhibit a slower and smaller thermal expansion before the wax melting point and a larger expansion afterwards. This is further evident in the thermal strain curve at 10kPa of pressure. Under these conditions the actuator expands up to 63°C, then collapses to zero strain at 70°C. The actuator continues to contract until approximately 100°C, after which it expands approximately linearly. After the removal of the load the actuator recovers and is not damaged.

The sudden collapse is explained by a rapid reduction in stiffness at 60°C once the wax is completely melted. The expansion after this is solely due to the pressure inside the wax increasing and doing work against the stiffness of the forests to expand it further. The stiffness of the actuator at select temperatures is shown in Figure 4-6. Event at room temperature the stiffness of the actuator is 18.6 GPa, which is 15 times larger than of the CNTs which have been compressed, but are not infiltrated. Furthermore, the actuator stiffness increases to 46.7 GPa at 40°C. As expected the stiffness drops dramatically at 60°C to 4.5GPa, while at 100°C the stiffness of the actuator drops below the stiffness of the CNTs. I hypothesize that the reason for this is that the wax lubricates the CNTs which increases the relative slip between them. Due to an increased slip the nanotubes are able to move relative to one another, reducing the overall stiffness of the network as they are no longer to laterally support each other.

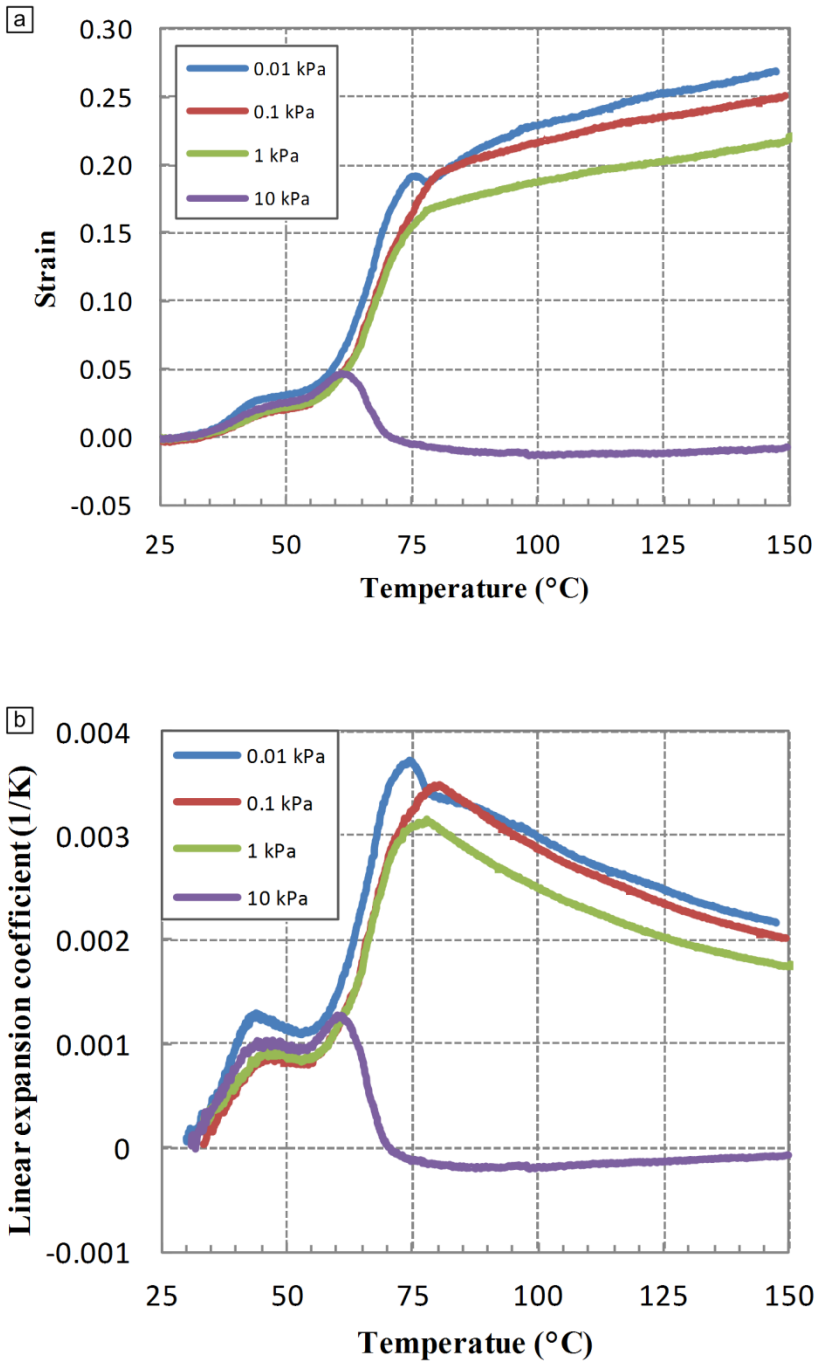

Figure 4-5. Thermally generated strain under constant load for a CNT-paraffin actuator compressed by 50% prior to infiltration. (a) Thermally generated strain under various loads. (b) Linear expansion coefficient under various loads.

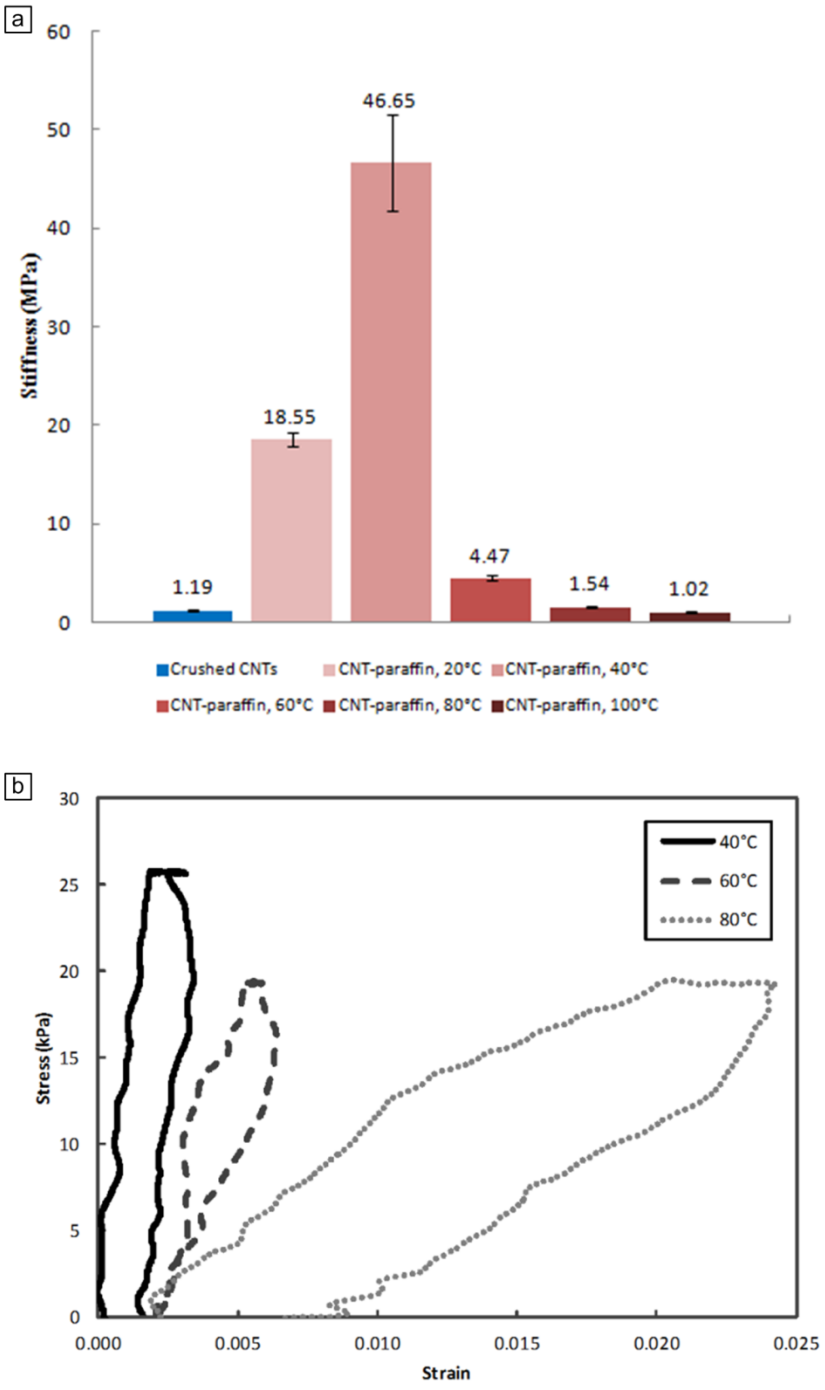

Figure 4-6. Temperature dependent stiffness of CNT-paraffin sheet actuators. Stiffness of pre-buckled CNTs is shown for comparison. Inset shows sample stress-strain curves for the sheet actuator.

The measurements of the CNT-paraffin actuators show similar characteristics as the standard pressure-volume-temperature data for paraffin wax having larger molecular weight [100] than

the one used in our experiments (Figure 4-7). Because our actuator geometry couples the volumetric expansion of paraffin wax to a linear expansion in film thickness, the thermally generated strain of CNT-paraffin composite films can be directly compared to the volume change from the standard pressure-volume-temperature data.

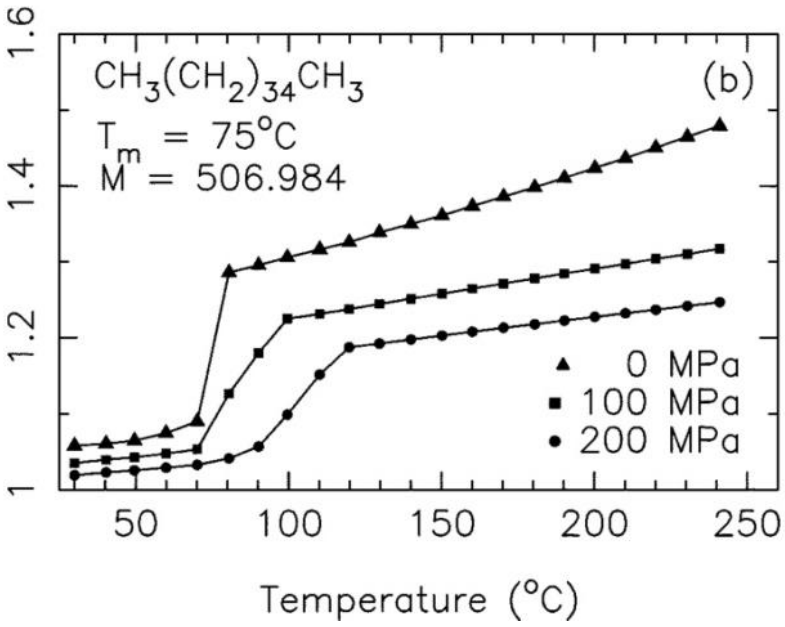

Figure 4-7. Standard pressure-volume-temperature curve pure paraffin of larger molecular weight. Chart taken from [36].

From the thermally generated strain under various loads in Figure 4-5 it is evident that some strain is generated even before the wax melting point. This suggests that the fabricated actuator has two regimes of actuation: (1) a low temperature and strain, but high stiffness regime below the wax melting point and (2) a high temperature and strain, but low stiffness regime above it.

The regime division is shown in Figure 4-8a. The behavior of the actuator in regime 1 could be explained by considering the vertical displacement during sample cooling and the temperature dependence of the stiffness. From the displacement data collected during sample fabrication, the actuator undergoes shrinkage during sample cooling. This rapid shrinkage coincides with the solidification of the wax, which means that at room temperature the CNTs are under compression. As the composite heats up the wax softens before melting and allows the CNTs to spring back, releasing the elastic potential energy stored during wax freezing. This energy does work against the viscous forces in the wax and lifts the applied load upwards. As the wax melts

all of the potential energy is released and the CNTs are no longer under compression. This behavior is analogous to shape memory materials where stored potential energy is released during heating, resulting in a shape change. However, unlike most shape memory materials, upon cooling the wax pulls the CNTs back to their original shape.

In regime 2, the wax has undergone melting and has significantly expanded the CNT forest from its crushed height. The individual CNTs within the forests are being straightened as the wax continues to expand and does work against them. If the CNTs are straighten to the point where their major contribution to the resistance against the work the wax is doing is their axial stiffness, the wax would be pushing against straight CNTs loaded in tension, which have a stiffness on the order of 1 TPa. In this case, the wax would not be able to axial extend the CNTs and would either deform the network laterally or the pressure inside the wax would overcome the capillary pressure keeping it confined to the forest and the wax would flow out. This behavior would be preceded by thermal expansion coefficient approaching zero, which is not the case here as seen in Figure 4-4b and Figure 4-5b. However, the linear thermal expansion coefficient in all cases is reduced exponential upon heating past the wax melting temperature.

In general, the straightening of the CNTs is accompanied by a reduction in compressive stiffness. This is expected since CNT network will have fewer junctions as the individual CNTs are straightened. These junctions allow touching CNTs to be locally pinned to each other and be supported laterally. For a fixed length nanotube, the higher number of these junctions, the shorter the unsupported effective length CNT length between them. A short effective unsupported CNT length increases the load required to buckle this region. In an extreme case a straight single CNT might be 15nm in diameter and a millimeter long. This CNT would be modeled as a column with one end fixed to the substrate and the other end free to move, which would result a critical force of 12 femtoNewtons using Euler's column buckling equation. On the other hand, a CNT within the forest may have a hundred junctions over its length. This would reduce the free length significantly and each unsupported length (treated as a column hinged at both ends) could withstand 49 nanoNewtons. However, these sections would not be supporting the load axially, since they would meander from one adjacent tube to another, reducing their likelihood to catastrophically buckle further. In our experiments, if the load is increased sufficiently in region

2 the CNTs will catastrophically compress back to their buckled state. The thermally generated strain under 10kPa in Figure 4-8 showcases this behavior.

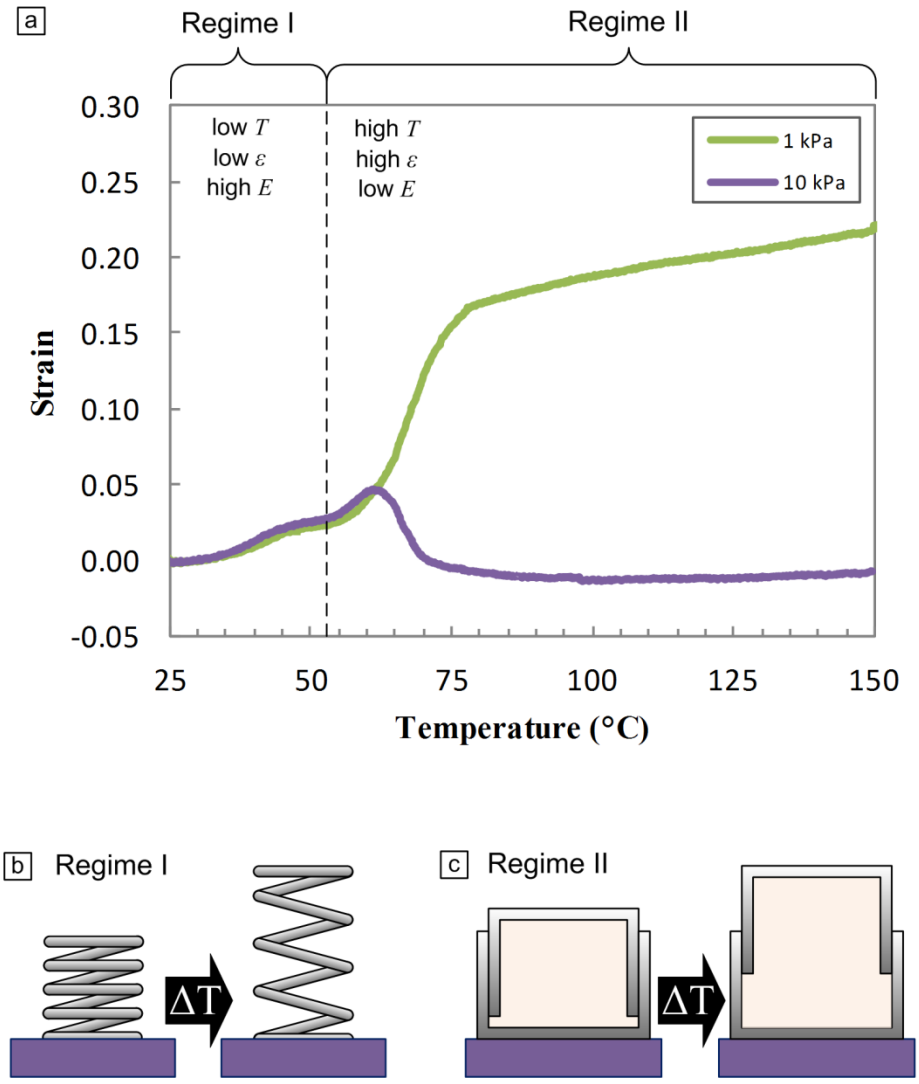

Figure 4-8. Multiple regimes of CNT-paraffin actuation. (a) Thermally generated strain under load with separation between regimes indicated. Also, shown are analogous models for regime I (b) and II (c).

4.4 CNT-paraffin actuators as thermal switches

Thermal switches are devices and materials whose thermal conductivity varies with temperature. An ideal thermal switch has a near zero thermal conductivity when not engaged and upon crossing a temperature threshold has a large thermal conductivity. These devices and

materials are used as smart switches to control the cooling of various devices when heat management is at a premium. One such application is the cooling of electronics and other components on satellites [99], where the only way to remove the generated heat is to radiate it out with a specialized antenna.

The fabricated CNT-paraffin actuators are an excellent candidate material for the use as a thermal switch, especially since custom made paraffin actuators are already used on satellites. The CNT-paraffin actuator would extend upon heating and engage with the heat sink to conduct heat away, then upon cooling would retract again. A unique aspect of the actuator is that the temperature at which it would engage the heat sink can be controlled in multiple ways. The separation between the top surface of the actuator and the heat sink or the CNTs compression during fabrication could be used to control the temperature at which the heat sink is engaged. Figure 4-9 shows (a) a schematic of the setup used to measure the thermal conductivity of the CNT-paraffin actuators and (b) the measured thermal conductivity.

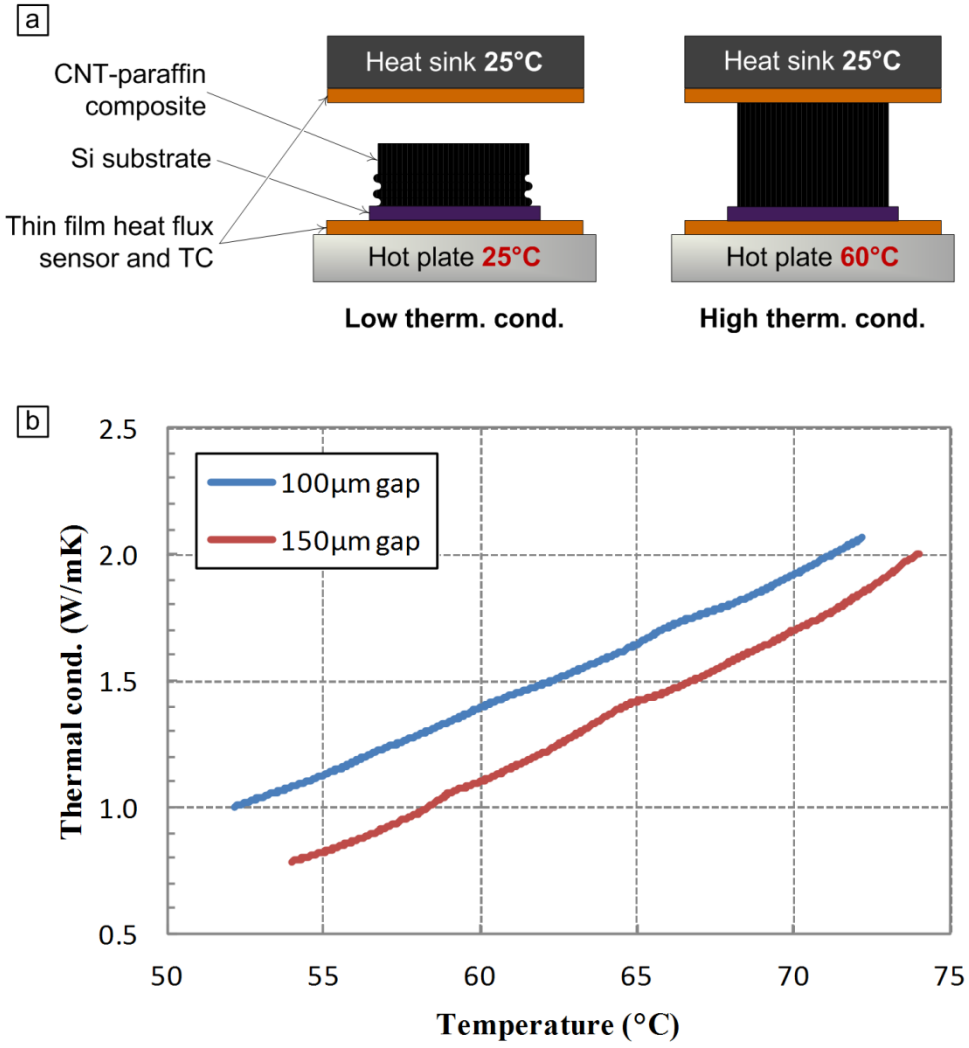

Figure 4-9. CNT-paraffin actuators as thermal switches. (a) Setup used to measure thermal conductivity of CNT-paraffin sheets. (b) Thermal conductivity of actuator for two gap spacings.

The measured thermal conductivity (Figure 4-9b) compares favorably to that of other CNT-polymer composites, at the lower temperature range [107, 108]. The thermal conductivity is approximately one order of magnitude higher than that of paraffin itself, but this order of magnitude is expected since the CNTs constitute about 4% of the composite and have a thermal conductivity of 3500 W/mK [31], which is three orders of magnitude higher then paraffin.

4.5 Conclusion

CNT-paraffin film actuators were fabricated and tested, exhibiting up to 20% thermal strain at 175°C. This high-stroke vertical actuation is enabled by strong capillary interaction between paraffin and CNTs, and engineering of the vertical compliance by compression of the CNT forest prior to and during paraffin infiltration. Two mechanistic regimes of the CNT-paraffin actuator are proposed: a high stiffness, low strain mode below the melting point and a low stiffness, high strain mode above the melting point. The excellent thermal strain and thermal conductivity may allow this actuator to function as a good material in thermal switches.

CHAPTER 5: THERMALLY AND OPTICALLY ACTIVE LCN SHEETS AND MICROSTRUCTURES

Significant portions of this chapter with additional editing were published in: D. Copic, A. Ya'akobovitz, A.J. Hart, 19th International Conference on Composite Materials, Montreal, Canada, 2013, ref [62].

5.1 Background

Surfaces with dynamic micro- and nanoscale textures can potentially be used to manipulate friction drag, optical reflection, thermal transport, and other properties as previously discussed in Section 1.2. However, in order to realize these applications, surfaces must be made consistently over large areas, and integrated with existing laminate and skin materials for use in larger applications such as vehicles or aircraft.

Liquid crystal polymers are good candidate materials for use in active surfaces due to their tunable mechanical properties [109-111], anisotropic expansion upon heating [58], and opportunity for optically directed actuation [112-114]. For example, thin sheets made from stiff glassy optically active azobenzene based LCN have been shown to oscillate at 30Hz with a tip displacement amplitude of 170° [115]. An important distinction is that the term liquid crystal polymers refers to both liquid crystal elastomers (LCE) [116, 117], which are materials with low cross link density that experience large strains and low stiffness, and liquid crystal networks [112, 118], which are highly cross linked glassy polymers that exert low strains, but maintain a high stiffness during actuation. The work in this chapter focuses on LCN, due to their larger potential for useful work output.

LCN actuation is based on the volume change in the material induced by the disruption of the order of a liquid crystal phase. For thermally active materials, this is readily achievable since an increase in temperature will provide sufficient thermal energy to overcome the intermolecular forces between adjacent LC moieties inducing the LC order.

The photomechanical transduction in LCN materials is achieved by providing sufficient light to achieve a molecular shape change of stiff moiety responsible for disturbing the LC phase. The LC monomers used in this work employ the optically driven isomerization of azobenzene moieties for disturbing the order of the thermally active host LCN, which is cross linked in a nematic phase [115, 119, 120]. If a photon with sufficient energy is absorbed (typically blue-green light is used) by azobenzene it enables the rotation of about a double bonded nitrogen, effectively changing the configuration of the molecule from a straight state (trans isomer) to a bent state (cis isomer). This isomerization induces a bathochromic shift in absorbance (typically centered near 450 nm), an increase in polarity, and a change in the molecular axis of the rigid rod-like azobenzene moiety from 9 to 5.5 Å [121, 122]. The buildup of the cis isomer is responsible for disturbing the host LC order and the associated contraction along the LCN director.

The LCN material used in the following studies (Figure 5-1a) can be actuated optically by UV light to drive the trans-cis isomerization or by polarized blue light capable of providing sufficient energy to drive both the trans-cis and the cis-trans isomerization of azobenzene [115, 119, 120], due to an overlap between the cis and trans isomer absorption spectra [123]. The azobenzene trans isomer moieties absorb significantly less polarized light if they are oriented perpendicular the polarization, gradually creating a statistical buildup of such isomers. This buildup disturbs the nematic phase, reducing its order and achieving a volumetric shape change (Figure 5-1b). This shape molecular shape change or reorientation can be used to alter either the height of a micropillar if the director is oriented along its axis (Figure 5-1c) or the pillar cross section if the director is oriented perpendicular to it. Because the actuation is based on a reduction in the order of the nematic LC phase, having good alignment prior to cross-linking the LC monomers is crucial. Although the maximum generated stress of LCN materials are lower than that of other comparable polymers, below it is shown that LCN materials can be cast into a verity of useful microstructures.

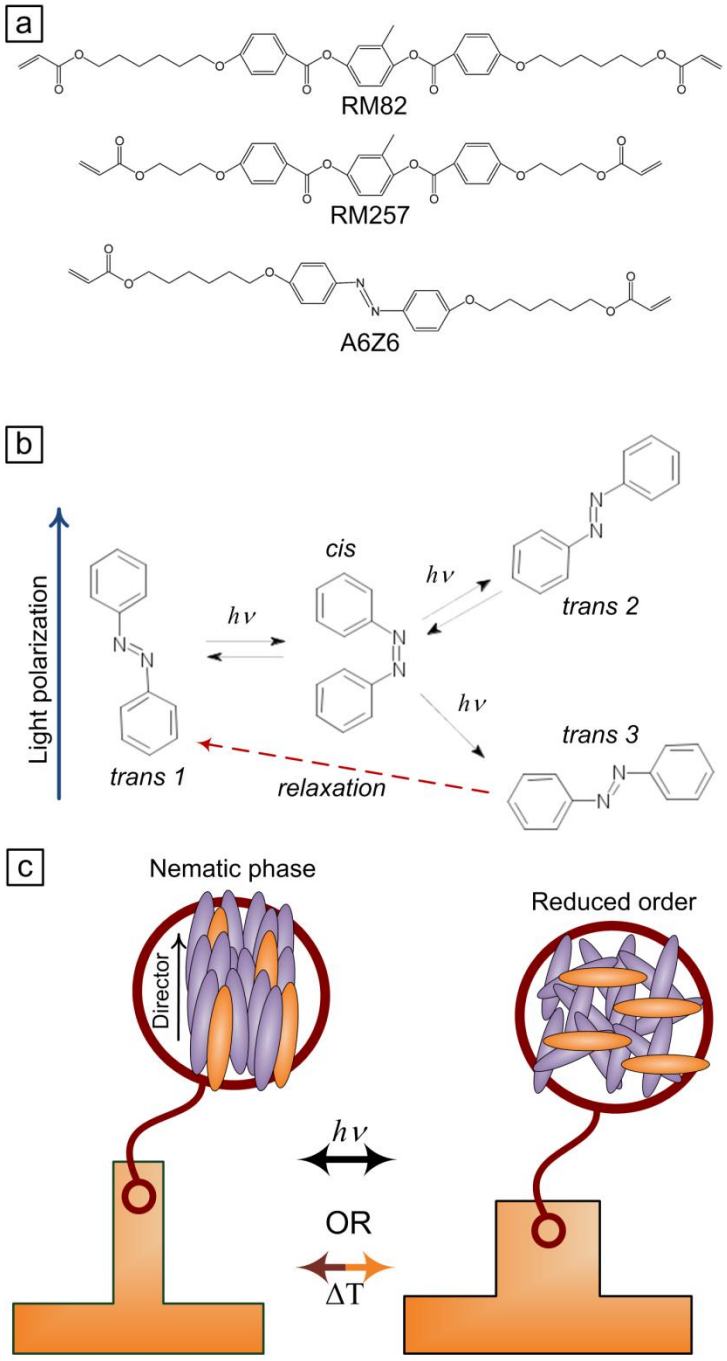

Figure 5-1. Chemical structures of used compounds and LCN actuation mechanics. (a) Chemical structure of LC monomers. (b) Azobenzene reorientation under polarized light via trans-cis-tans isomerization. (c) Microstructure actuation mechanics based on azobenzene reorientation.

This chapter presents a REM fabrication technique [91] to obtain high fidelity thermally and optically active surface bound glassy LCN microstructure actuators over large areas. Thermally active LCN sheets and microstructures exhibit strains from 1% to 6%, depending on the

processing conditions used. The necessary LCN alignment for actuation was obtained via curing in a magnetic field, while removal of oxygen during curing was critical to achieve high-fidelity microstructure replicas with smooth surface texture while. Cast microstructures had lateral dimensions of a few microns and AR up to 15:1. A gradient based edge detection algorithm [124] was used to quantify the photodriven LCN microstructure actuation, which was on the order of 0.25% strain.

5.2 Fabrication process

LCN microstructure arrays and sheets were fabricated by REM within a magnetic field in a controlled atmosphere. The experimental setup includes a custom magnetic circuit designed to straighten and confine a magnetic field through the sample. The magnetic yoke was placed inside a vacuum jar, whose aluminum base was in contact with a hotplate and is shown in Figure 5-2a. A green LED light source, used to initiate polymerization, was located outside of the vacuum jar. When a powder mixture sensitive to ambient light was used the setup was located in a darkroom. In the case where UV active initiators were used, the sample was placed under a UV light (75 mW/cm^2) for curing.

Master templates used in the casting of LCN microstructures or sheets can be fabricated using standard silicon dry etching processes, or alternatively CNT-SU-8 nanocomposite microstructures may be used to fabricate complex geometries as detailed in Chapter 2. From the master, a PDMS negative was cast and used to create the LCN replicas. For the following experiments, the PDMS was vacuum cast over the DRIE patterned silicon master and cured at 120°C for 20min to form the negative mold (Figure 5-2c).

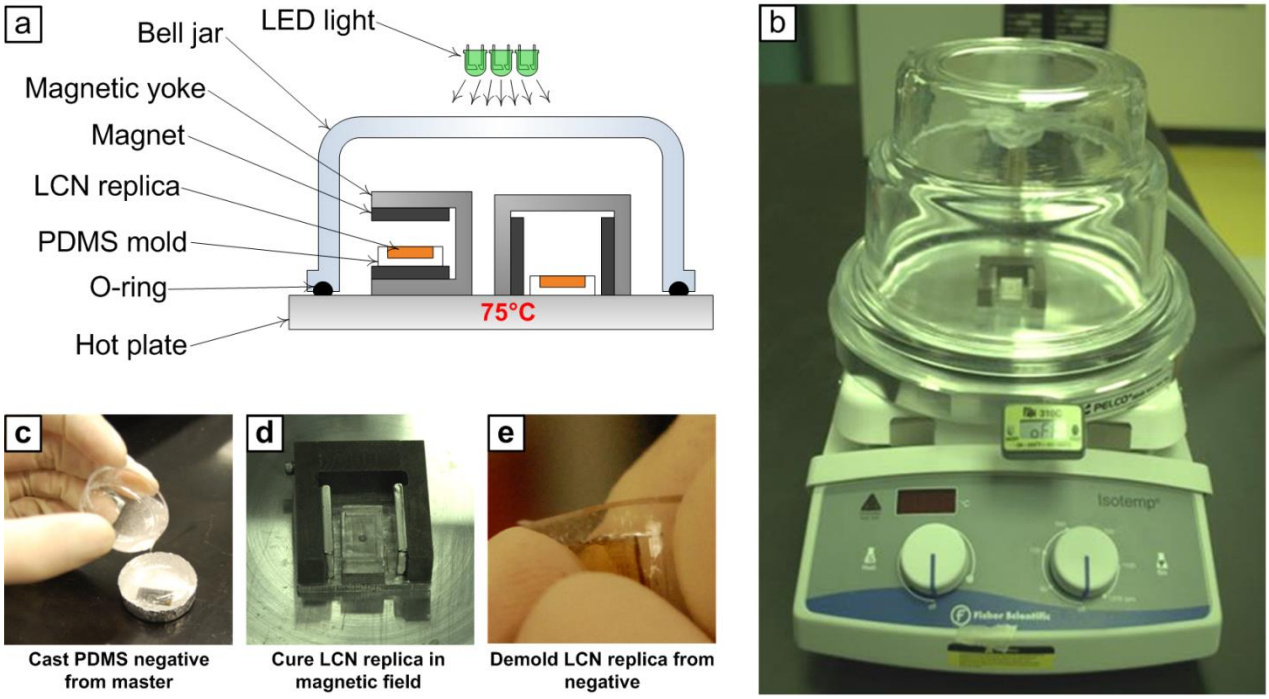

Figure 5-2. Setup used for casting and curing LCN microstructures. (a) Schematic of setup with call outs. (b) Photo of setup. Key steps of procedure are alos shown including (c) casting of PDMS negative, (d) LCN replica curing in magnetic field, and (e) demolding of replica.

Generally, a powder mixture containing the LC monomers and initiator is synthesized or purchased. The powder mixture is then dispensed onto the PDMS negative, located in the setup (Figure 5-2d). The powder is melted by increasing the temperature above the LC isotropic transition temperature (typically 110ºC) for 10 to 30 min. The powder melt in many cases has either large visible air bubbles or appears foggy even after prolonged heating. In either of these cases, degassing is performed to remove the air bubbles. The liquid LC monomer is brought down to 1 Torr for 20min, which causes the majority of the bubbles to burst. Any remaining bubbles can be burst by rapidly increasing the pressure. At this point the vacuum may be broken and a backing may be added to the PDMS negative, such as a glass or silicon chip, before lowering the pressure again to vacuum cast the replica.

The magnetic field (0.3T) applied by the fixture causes benzene containing LC monomers to align in a cooperative fashion along it. The cooperative alignment of benzene rings inside a magnetic field was first suggested by de Gennes [125] and successfully demonstrated for use in liquid crystal elastomers by Buguin et al. [58] The mixture was then cooled to 75°C or 25°C at 1°C/min resulting in a LC in the nematic phase with its director aligned along the magnetic field.

Placing the sample in a strong magnetic field, which has been straightened via a magnetic yoke, and cooling it slowly achieves the necessary order and alignment for actuation. Depending on the contents of the formulation, the sample was then exposed to either green light (540 nm wavelength) for 40 min or to UV light for 30sec to 2 min, in both cases this initiates cross-linking of the ordered LC monomers into a stiff glassy polymer network. After cooling to room temperature the LCN replica was manually demolded from the soft PDMS negative (Figure 5-2e).

For use in thermally active microstructure and sheet replicas the commercially available RMM491 mixture was employed (EMD Chemicals). According to the manufacturer RMM491 consists of no more than 25 wt% RM82, an unstated amount of an UV photoinitator, and the remaining fraction of RM257. For optically active microstructure replicas, a LC powder mixture composed of 20 wt% optically active 4,40-bis[6-(acryoloxy)hexyloxy] azobenzene monomers (A6Z6 from BEAM Co.), 78 wt % thermally active RMM491 monomer mixture (EMD Millipore), and 2 wt % I-784 photoinitiator (Ciba) was employed [109]. The constituents of the RMM491 mixture and the optically active LC monomer, labeled A6Z6, are shown in Figure 5-1a.

The thermally generated strain of LCN sheets is generally large enough to be easily observed by cameras and measured by commercially available software. Although the same measurements can be applied to observe the thermally active LCN microstructures, their imaging must be done using a highly sensitive scanning electron microscope. For optically active microstructures, a custom-built microscope was used to image their actuation (Figure 5-3) in conjunction with a custom edge tracking algorithm [124]. This microscope employs a linearly polarized blue light and a white light source to characterize the LCN response. To trigger the mechanical response in these materials, the samples were exposed to linearly polarized blue light (~440 nm wavelength) aligned parallel to the LC director for 3-5 minutes. After actuation the sample was exposed to visible light for 15 minutes or heated to 90°C causing it to relax and recover its original shape. Azobenzene moieties predominantly take on the *trans* isomerization during the relaxation and the polymer network recovers its initial higher order.

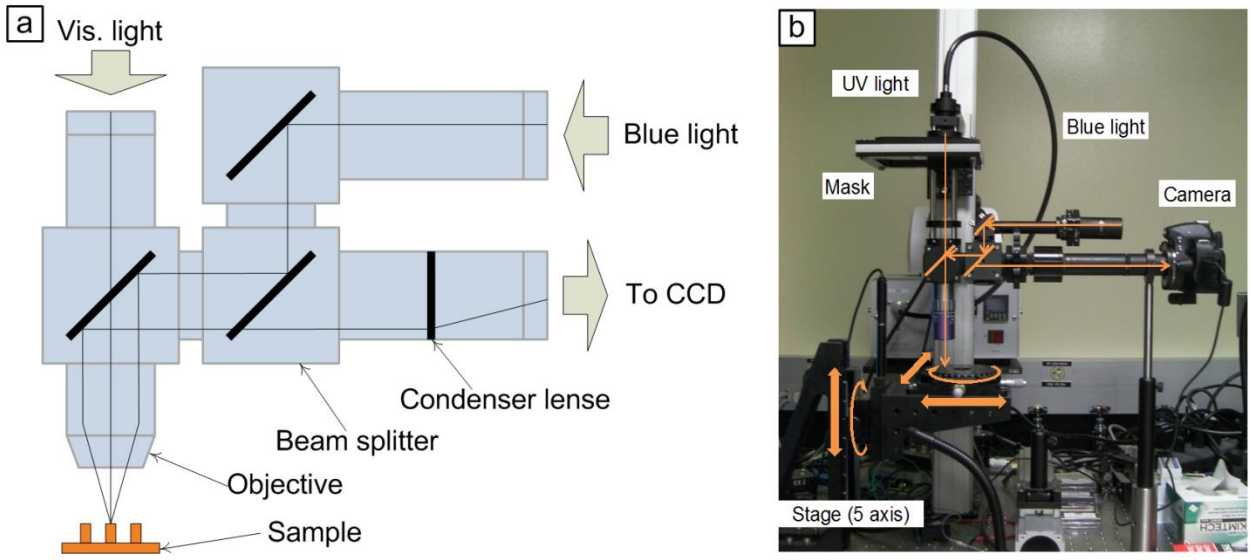

Figure 5-3. Custom built microscope used to actuate and measure the strains of optically active LCN microstructures. Microscope was designed and built by Ryan Oliver. (a) Schematic overview and (b) photo of the setup.

5.3 Thermally active LCN sheets and microstructures

Since the actuation of LCN materials is based on a reduction in order on a molecular scale, it is crucial to fabricate sheets and microstructures with high initial order. The molecular order in these LCN materials is induced via co-operative reorientation of benzene rings of the LC monomers as discussed above. Both the order parameter and the rate at which this order is established are dependent on the strength of the magnetic field used. Toward this effort a two dimensional finite element simulation was built to simulate the field strength and uniformity of the flux lines of a set of magnetic yoke designs. A select design is shown in Figure 5-4.

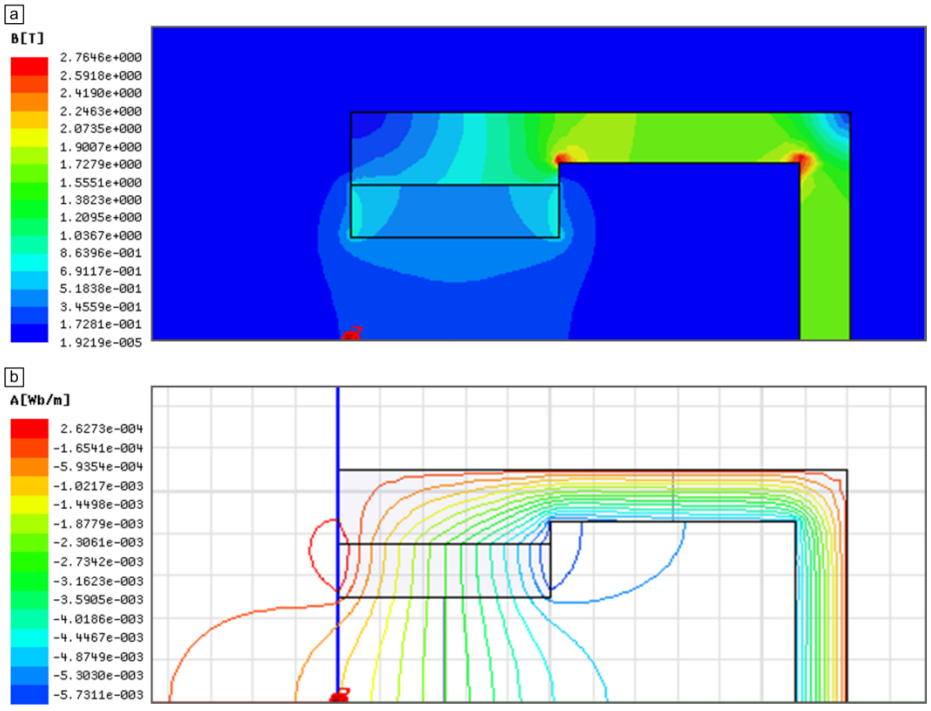

Figure 5-4. A two dimensional finite element simulation of a magnetic yoke design in half symmetry. (a) Magnetic field strength and (b) flux lines of a select yoke design.

A uniform and straight field allows for all cast microstructures of one replica to have the same director alignment and order which yields to a uniform actuation performance. The co-operative LC alignment to the magnetic field is based on the competition between intermolecular forces, thermal vibrations, and the force applied via the field. Thermal vibrations are responsible for lowering the LC order, while the magnetic field is inducing a cooperative ordering. As the temperature of the sample is decreased the thermal vibrations are overcome by the force induced by the magnetic field and molecular forces to transition the material from an isotropic phase to a higher order phase. If the material is quenched, however, an isotropic phase can be obtained even at lower temperatures. Therefore, a stronger field allows for LC alignment to be obtained at a higher curing temperature, which would lower the processing time per sample and allow for scaling up of this process. Additionally, a stronger magnetic field may also allow for faster curing, while maintaining the same degree of order.

The alignment of the thermally active LCN is confirmed by comparing the thermally generated strain of a sample sheet cast from RMM491 inside the magnetic field to a sample cured out of the magnetic field (Figure 5-5). Upon heating, the sample cured without a magnetic field shows isotropic behavior, since the primary strains exhibited are identical (Figure 5-5a).

This suggests that the material did not have global order during sample curing, which means that the resulting sample is a polydomain LCN. On the other hand, Figure 5-5b shows the thermal strain of a sample cured in the magnetic field. The aligned sample shows no actuation along the director and significant actuation perpendicular to it, which is the expected behavior.

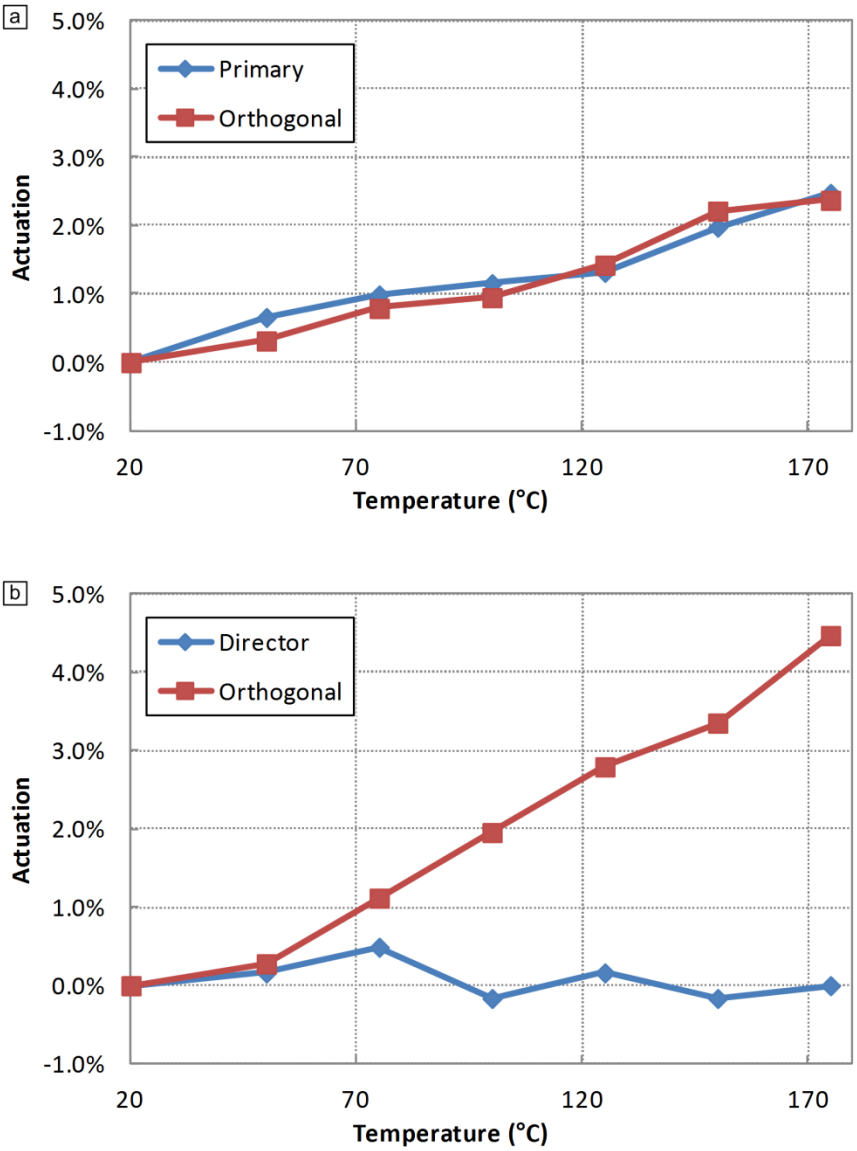

Figure 5-5. Actuation of thermally active LCN sheets cast (a) outside and (b) inside the magnetic field.

The thermal strain of a RMM491 sheet, cast using the above discussed procedure, along with select images is shown in Figure 5-6. The cast sheet is 5mm wide, 25 mm long, and about 500 µm thick and was cured such that the H field was pointing along its width. Since the director is aligned along the width the extension along the sheets length is observed. The sheet was cast

from a PDMS negative to verify that the components of the RMM491 mixture did not diffuse into the mold or otherwise damage it. The exhibited thermal strain in Figure 5-6 is highly nonlinear, since the material exhibits a large increase in thermal expansion between 50 ºC and 60ºC. The maximum achieved thermal strain is 1.4% at 100ºC.

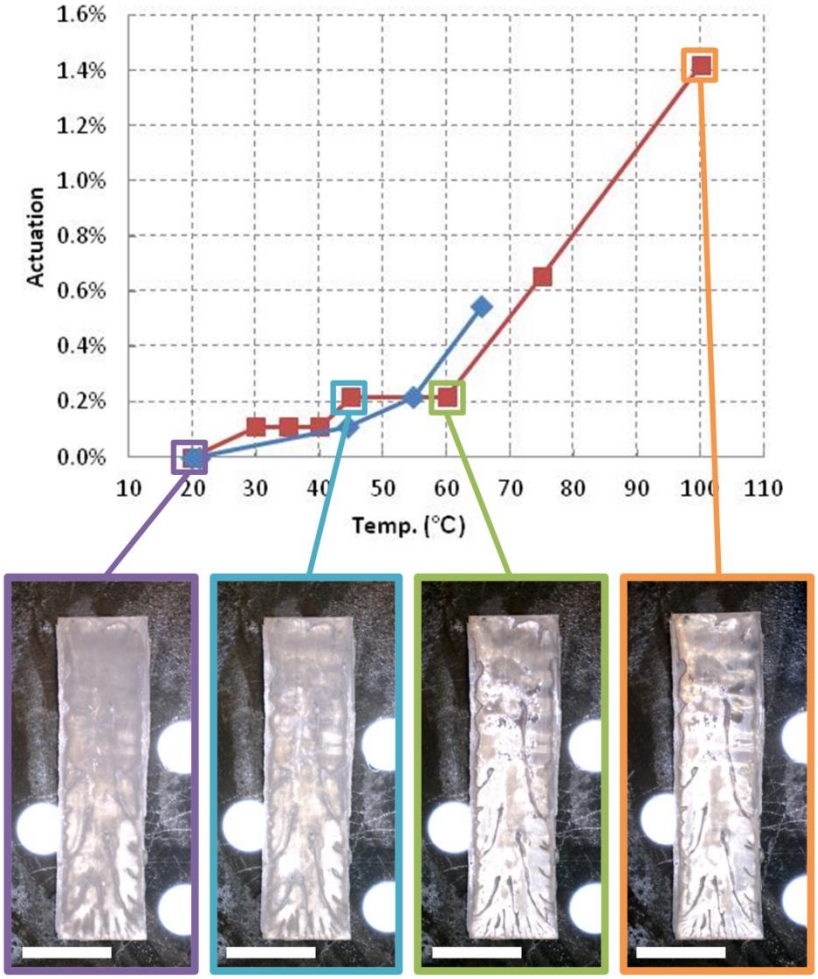

Figure 5-6. Actuation of thermally active LCN sheet on hotplate. Scale bar is 5mm.

Using the same thermally active LCN mixture an array of microstructures was cast similarly to the previously shown sheet. This sample was then placed on a thermal stage inside an environmental scanning microscope and imaged during heating. The thermally generated strain of one of these microstructures is shown in Figure 5-7. In this case, a rapid expansion after 150ºC is observed, which coincides with heating the LCN past the LC isotropic transition temperature.

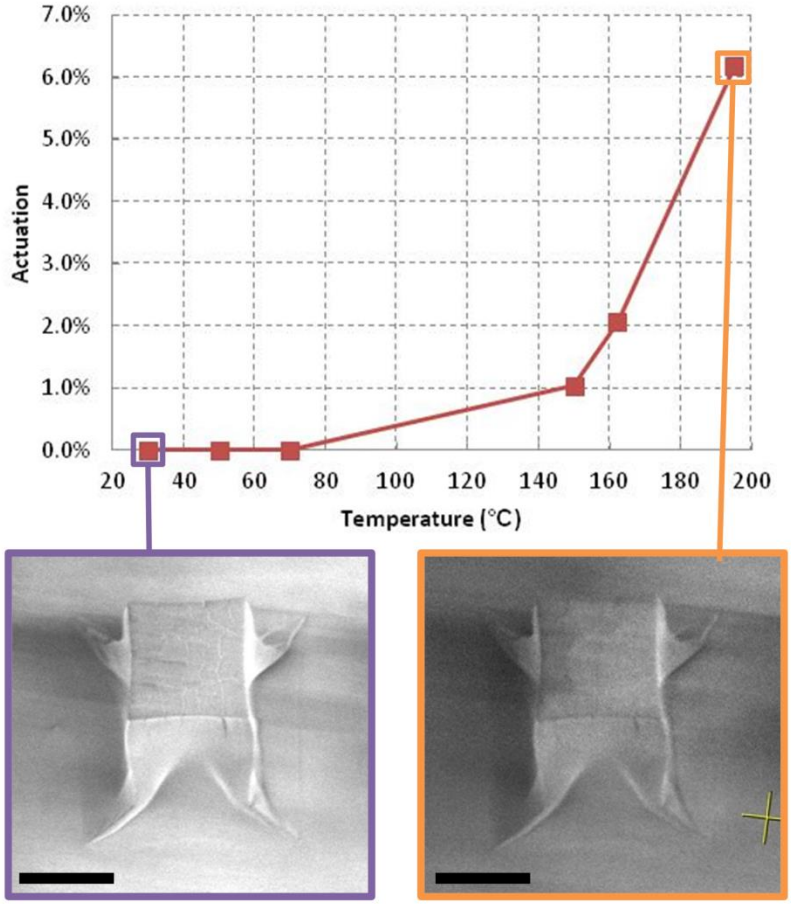

Figure 5-7. Actuation of thermally active LCN microstructure heated inside environmental SEM. Scale bar is 30µm.

5.4 Optically active LCN microstructures

Casting optically active LCN mixtures provided unique challenges in terms of material processing to achieve high quality replicas with any observable actuation. While LC mixture RMM491 was not significantly impacted by the presence of oxygen during casting, it was found that removal of oxygen was crucial for achieving low surface roughness high fidelity LCN replicas containing LCN monomers with an azobenzene moiety. Samples cast without degassing have large voids due to air bubbles trapped in the molten powder mixture and have very large surface roughness (Figure 5-8a). Figure 5-8b shows a sample that was vacuum cast at 1 Torr to remove air bubbles from the molten powder mixture, after which air was reintroduced during curing. The bottom part of the SEM image shows the sample edge that was exposed to the air.

Microstructures closer to the exposed edge have significantly larger surface roughness, suggesting that oxygen exposure impacts the phase behavior of the LCN. Samples with large surface roughness were found to have significantly reduced, if any, photogenerated strains.

Using these findings to drive process improvements, high fidelity microstructures with a variety of sizes and shapes, with both small and large aspect ratios were cast (Figure 5-9). Large microstructures with different cross-section shapes are shown in Figure 5-9a, while large arrays of HAR structures are shown in Figure 5-9b. The semi-cylindrical micropillars are 55 μm tall and have an AR of approximately 15:1. The size, scale, and yield of the fabricated microstructures is for the first time sufficient enough to become useful for active surfaces.

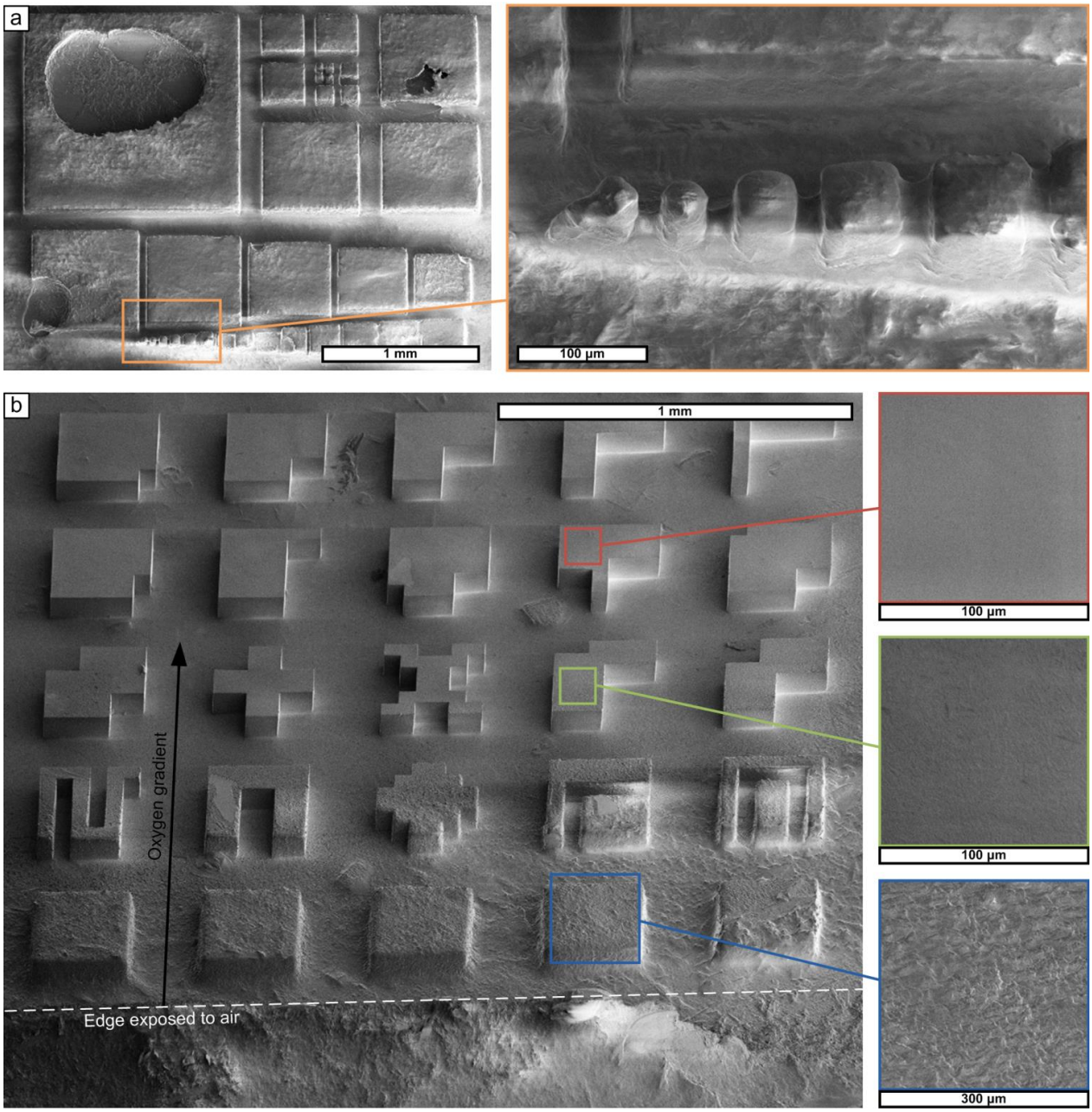

Figure 5-8. Contribution of oxygen to surface roughness and defects of cast microstructures. (a) LCN replicas cast without degassing of the molten LC mixture. (b) Degassed replica that was exposed to air during curing with close up images of selected regions, showing increased surface roughness in the presence of oxygen.

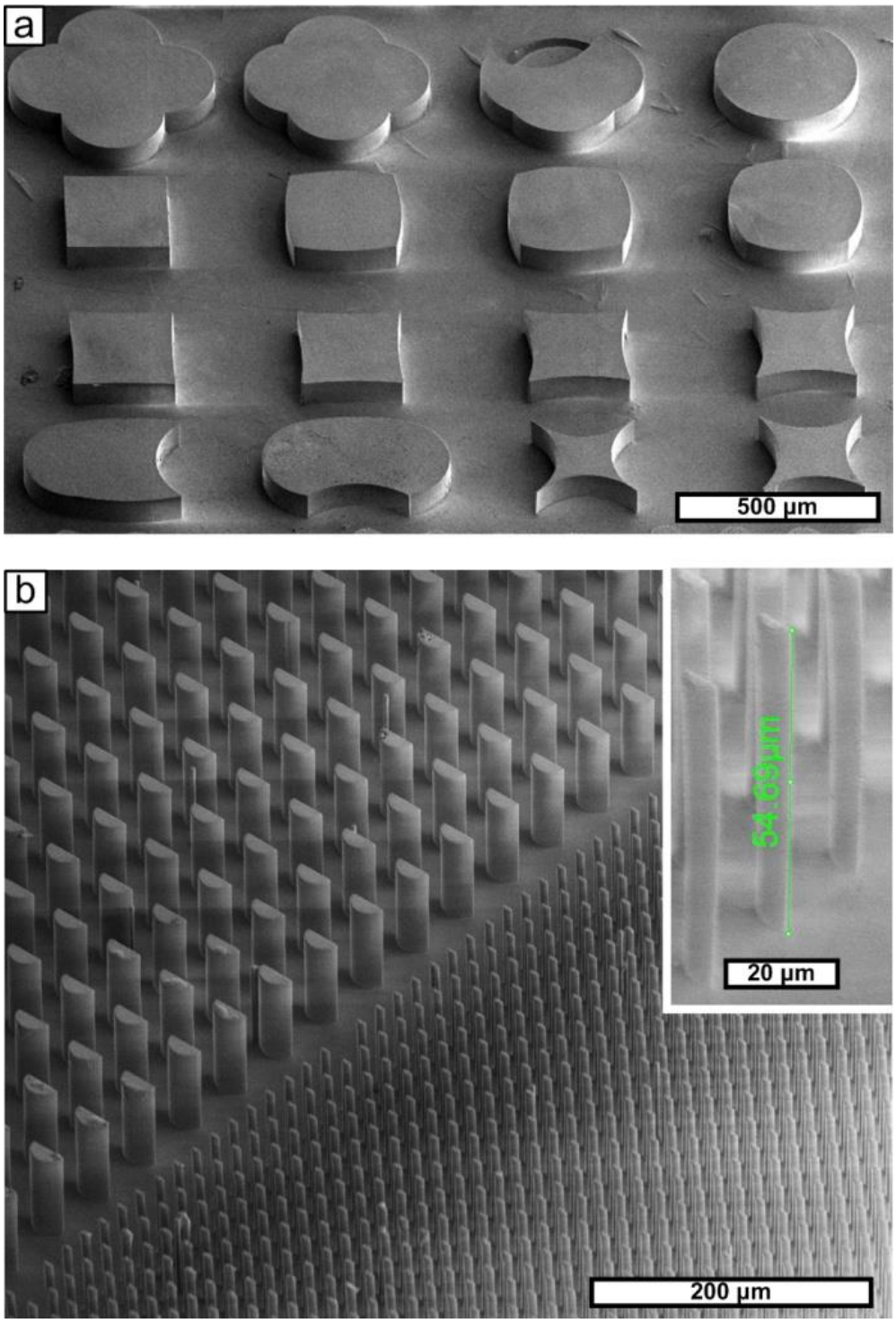

Figure 5-9. Successfully cast optically active LCN microstructures. (a) Heterogeneous low aspect ratio optically active LCN microstructures. (b) High yield, large area array of asymmetric microstructures. Inset shows close up image of microstructure.

An interpolation-based edge tracking algorithm [126] was implemented to optically resolve the optically generated strain of cast LCN micropillars with sub-pixel resolution. The algorithm

was developed by Dr. Ya'akobovitz and is schematically represented in Figure 5-10a. The algorithm operates similarly to other edge detection procedures only in that a threshold must be specified just above the pixel intensity of the edge. A value of an adjacent pixel is then used to draw a line intersecting the threshold; this intersection is the location of the edge. As the edge moves the grayscale value of the aforementioned adjacent pixel will change and with it the intersection representing. A rigorous demonstration and qualification of this algorithm is given in reference [124]. Figure 5-10b shows the tracking of a slow moving edge of optically actuated LCN microstructure.

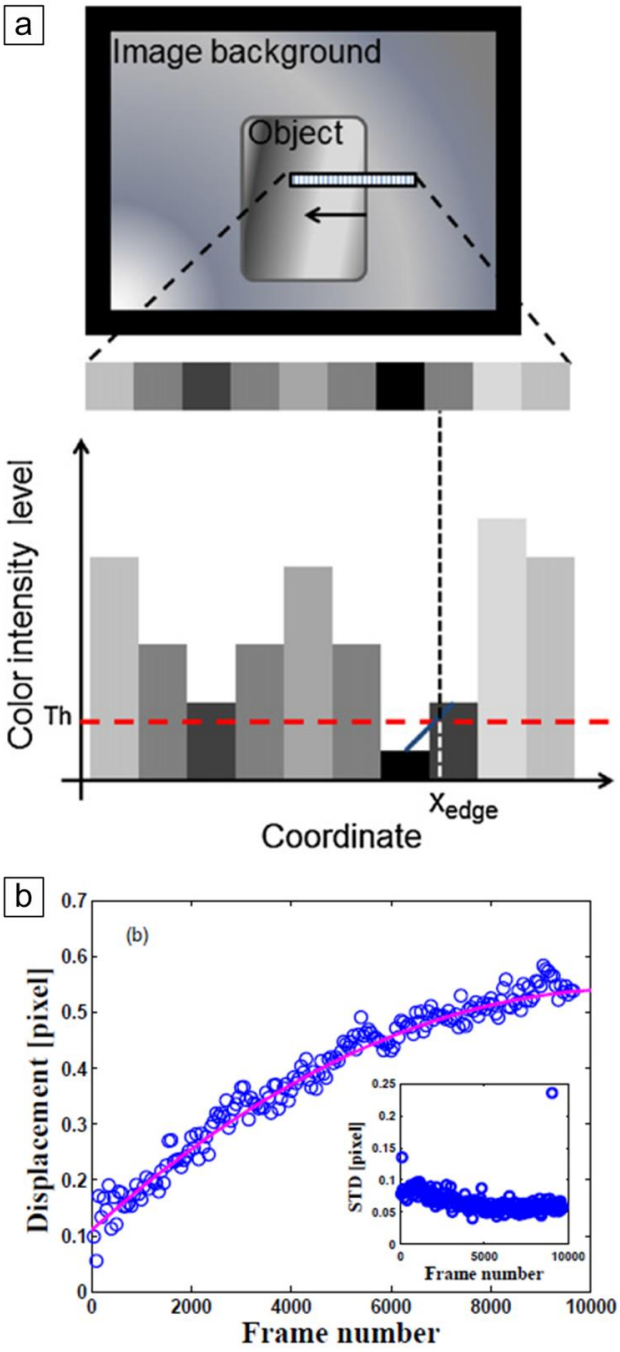

Figure 5-10. Custom gradient based edge detection algorithm used in measuring actuation of optically active LCN microstructures. (a) Illustration of detection method. (b) Measurement of slowly moving edge. Image adapted from [124].

This algorithm was employed in measuring the optically generated contraction along the director of a LCN micropillar and an expansion perpendicular to it. A SEM image and a top-down optical image of the optically active LCN microstructure are shown in Figure 5-11a and Figure 5-11b, respectively. A photogenerated strain of 0.25% orthogonal to the LCN director and

a 0.11% contraction along it after 5 min of exposure to linearly polarized blue light oriented perpendicular to the LC director was measured (Figure 5-11c). The contraction along the director occurs because the rod-like stiff LC moieties gradually rotate away from it. As expected, samples cured without the magnetic field showed no actuation. Previous studies with similar LCN compositions have measured a photogenerated strain along the director of 0.15% and a stiffness of 1.8 GPa using dynamic mechanical analysis (DMA) [120]. Larger strains could potentially be achieved via use of UV light, by achieving improved LCN alignment during the replica molding process, and by composition reformulation at the expense of reduced stiffness [109].

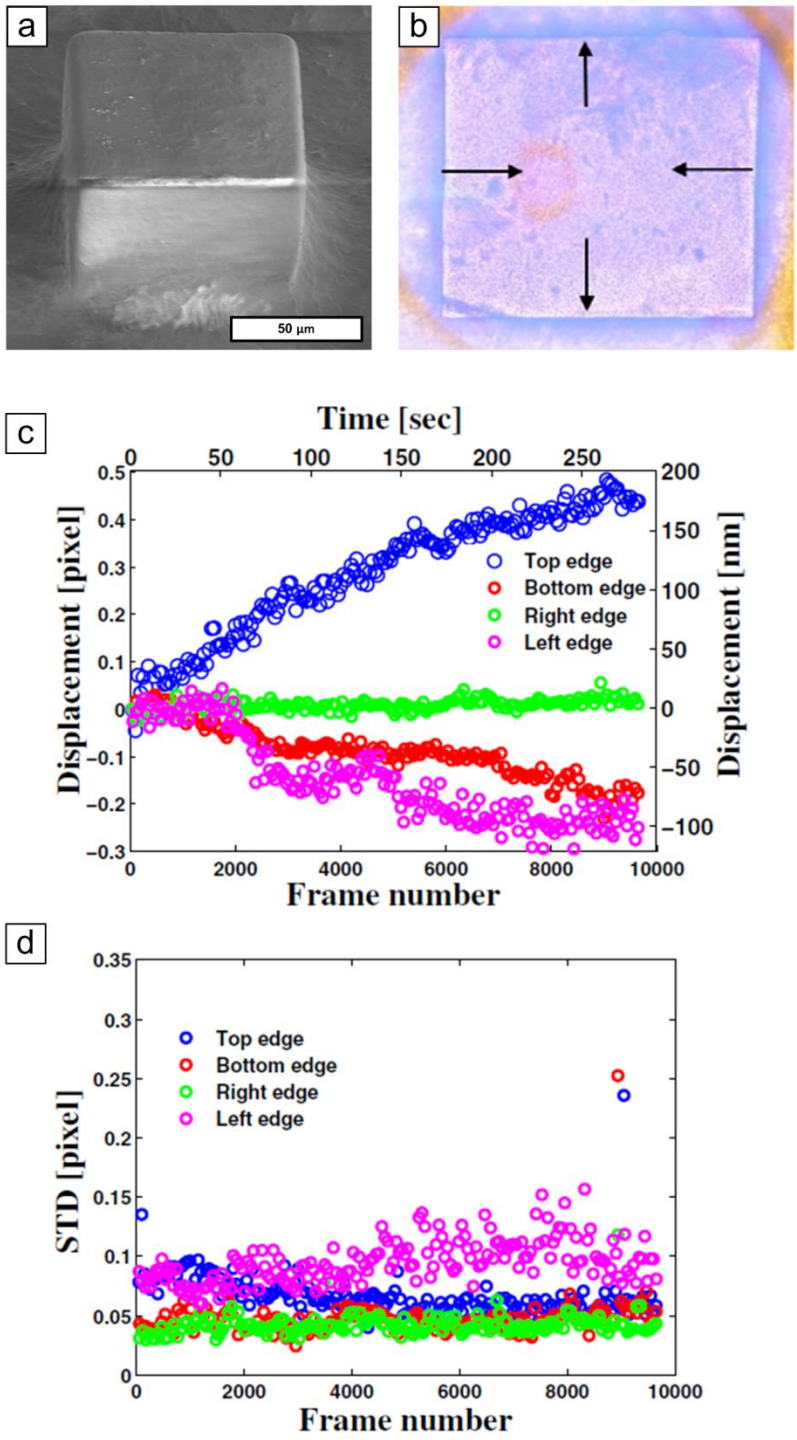

Figure 5-11. Edge tracking of optically active LCN microstructure. (a) SEM image of optically active LCN micro-pillar. (b) Sample optical image of the top-down view from a custom microscope used in for edge tracking. Arrows indicate strain direction. (c) Results of gradient based edge tracking algorithm, showing edge movement [124]. (d) Standard deviation of the per 20 frames which were averaged in the computation of the displacement.

In an attempt to study the casting of LCN microstructures and provide an increase in the photogenerated strain a custom vacuum chamber was designed to provide a temperature controlled stage in a magnetic field. The chamber was designed in a compact configuration to allow in situ imaging of the LC crystallinity using polarized optical microscopy (POM) [127-129].

In POM a sample is illuminated with linearly polarized light, while the reflected or transmitted light from the sample is linearly polarized perpendicular to the incident light. If the material of the sample does not interact with the light, all light will be blocked by the perpendicular polarizers. On the other hand, if a material interacts strongly with the light, as is the case with birefringent materials such as highly ordered liquid crystals, the polarization of the incident light changes such that it is not entirely blocked out by the analyzer (polarizer of the reflected or transmitted beam).

Figure 5-12a shows the CAD cross section view of the custom vacuum chamber designed to provide the thermal and environmental conditions for curing LCN microstructures while enabling in situ imaging using a POM setup. Figure 5-12b shows the thermal FEA simulation of a stage designed to minimize the thermal gradient across it, while Figure 5-12(d-e) show the ability to rotate the magnetic field in relation to the PDMS negative. The ability to rotate the initial LC alignment relative to the cast microstructure is desirable as it enables further control of deterministically programming the microstructure motion. Figure 5-13 shows the optical setup used in in situ measurements of the LCN order.

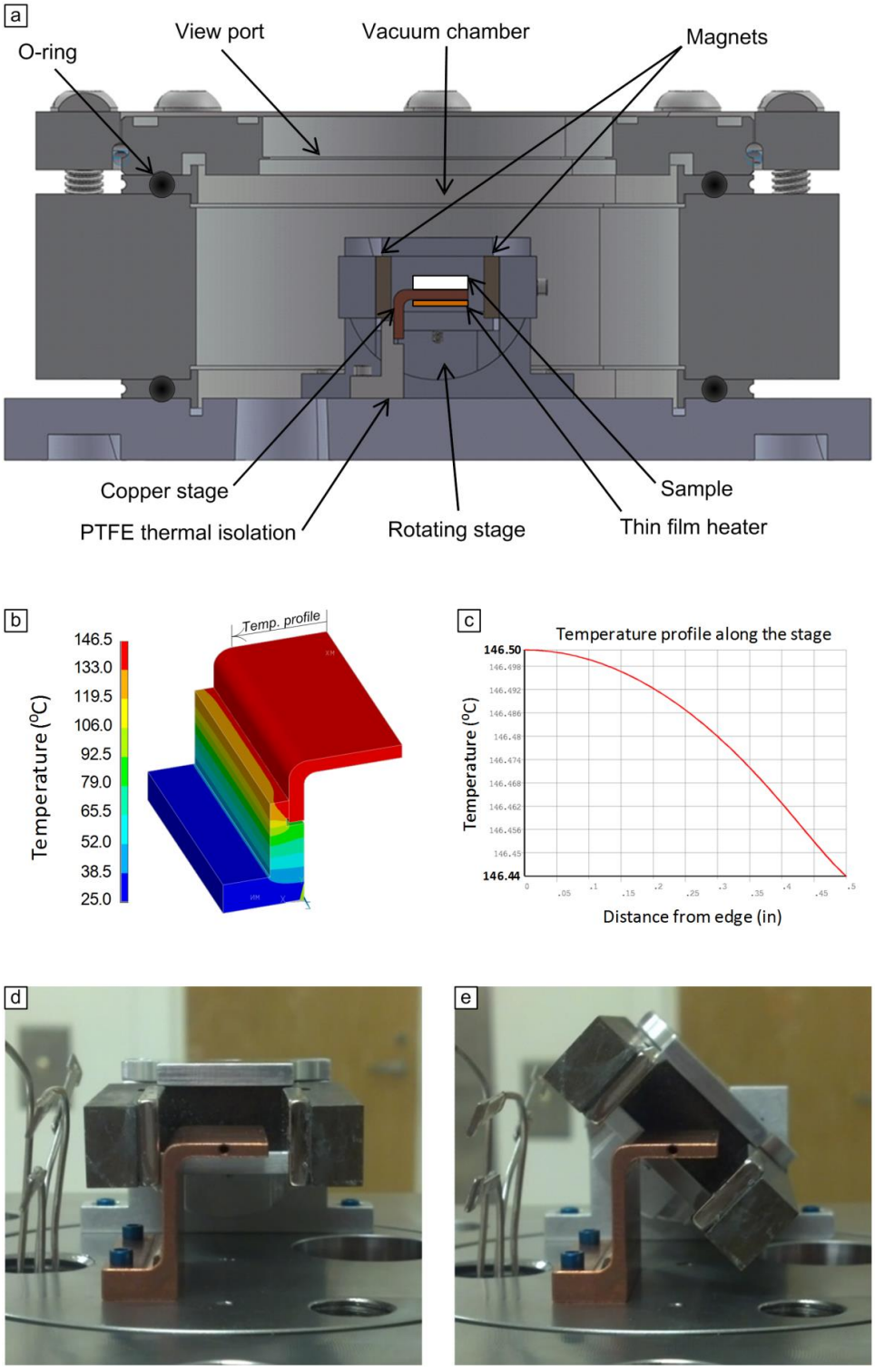

Figure 5-12. Design of new thermal stage, magnetic yoke, and vacuum chamber for casting and in situ imaging of LCN microstructures. (a) Cross section view and callouts of new vacuum chamber. (b) FEA thermal simulation of stage designed to minimize thermal gradients. (c) Simulation of temperature profile along stage edge. Stage designed to maximize thermal gradient in magnetic field with (d) 0º rotation and (e) 45º rotation.

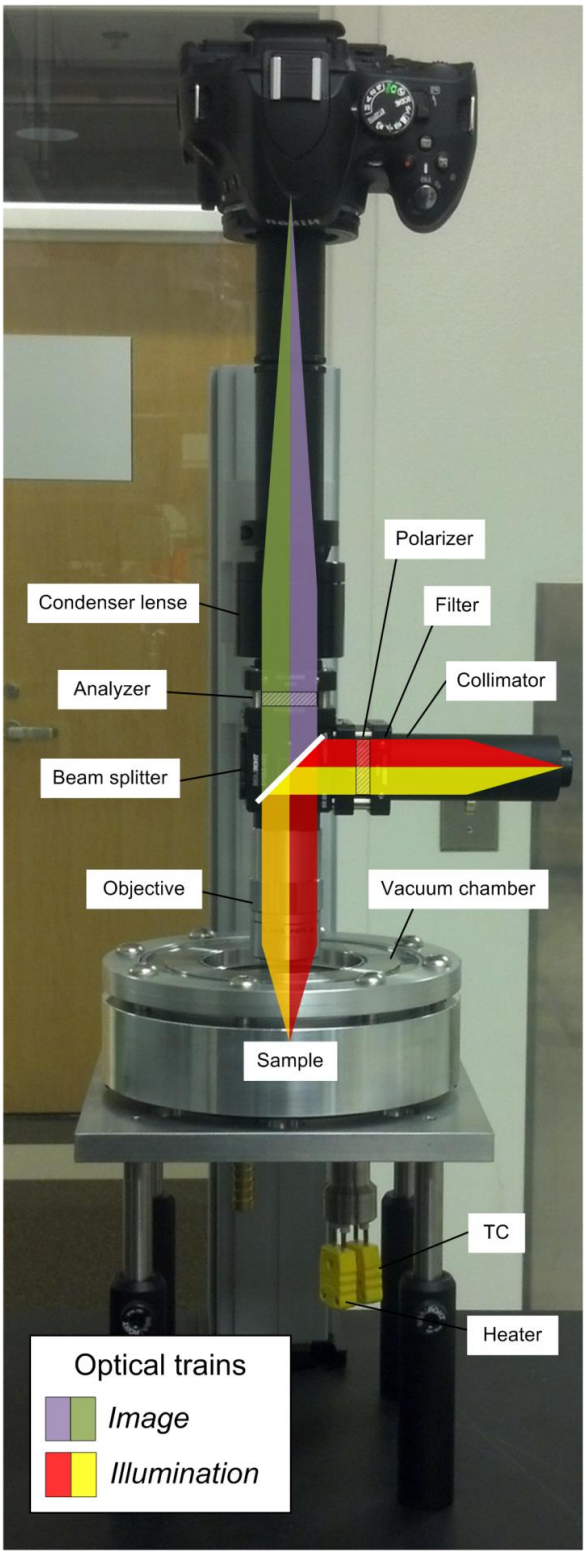

Figure 5-13. Optical setup designed in conjunction with new vacuum chamber to monitor LCN crystallinity in situ.

Select images from a sample video of a rapidly cooled sample (−50ºC/min) consisting only of one component (RM257) are shown in Figure 5-14. This is an in situ top-down view through the new optical setup; the rectangles are 30×30 μm recesses in the negative, which would form microstructures. Samples made from RM257 are thermally active and represent the simplest LCN system studied herein. As is typical with all studied samples the powder melt was degassed and heated above its isotropic transition temperature. Panel 1 shows the POM image of the isotropic powder melt. Since the molten LC monomer is not birefringent, any reflected light keeps the incident polarization which is perpendicular to the analyzer resulting in a predominantly black image. As the temperature drops LC domains begin to nucleate at defect sites in the mold (panel 2). Further reduction in temperature results in spontaneous nucleation of domains (panel 3). Oswald ripening takes place, increasing the domain size at the expense of the number of domain (panel 4). The domains then grow large enough to make contact with the mold and become less mobile (panel 5). Finally, domains grow lager as defects heal before the temperature drops below the glass transition temperature, immobilizing the domains (panel 5). Panel 5 shows a typical 'Schlieren' pattern observed of LC materials from POM images [130].

From the video and specifically panel 5 of Figure 5-14 several important observations can be made. The Schlieren pattern indicates that the alignment is not uniform across the imaged surface; this is expected since the cooling rate of −50ºC/min is too rapid (cooling rates on the order of −1ºC/min are typically used). Significant reduction in the streaks is observed during the last phases of sample cooling and upon subsequent heating. This can be used to develop an annealing method to further increase the uniformity of the alignment across the surface. Lastly, dark spots are seen predominantly located in the recesses. These areas remain dark regardless of sample orientation, meaning they are nonbirefringent, and are being further investigated in terms of their phase and order.

Two additional optically active mixtures are further examined using the same procedure and are compared in Figure 5-15. Mixtures containing the optically active LC monomer, labeled 2azo, have a significantly larger presence of the previously observed dark areas. The presence of a magnetic field does reduce the amount of nonbirefringent areas slightly, but does not appear to significantly change the location of the smidges, which are still predominantly located in the recesses. The presence of compound RM23 in the mixture exasperates the presence of nonbirefringent areas.

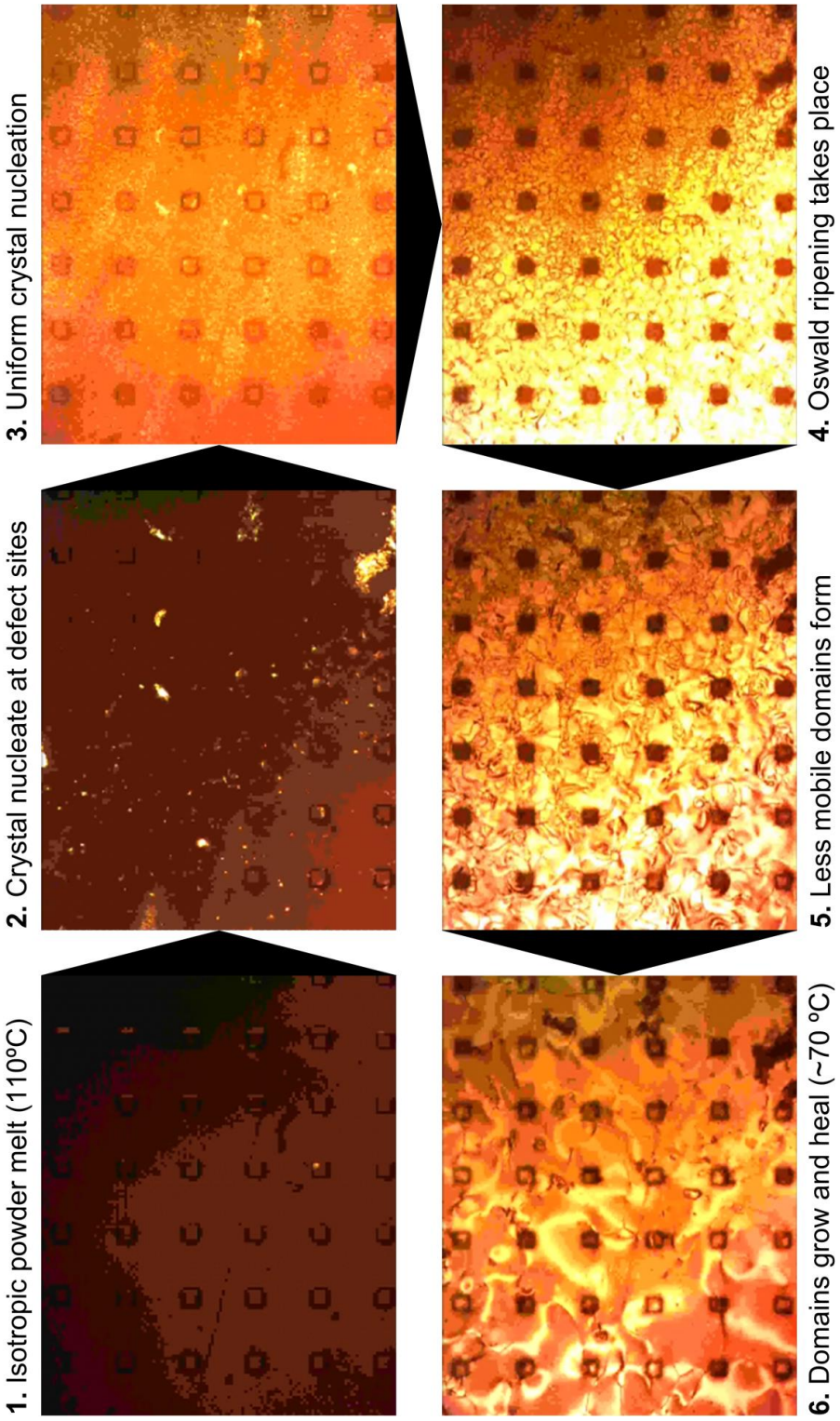

Figure 5-14. Still frames from in situ video showing, for the first time, the LCN schlieren texture of the namatic phase and present defects in the sample during microstructure casting. Each frame corresponds to a distinct stage in the curing process.

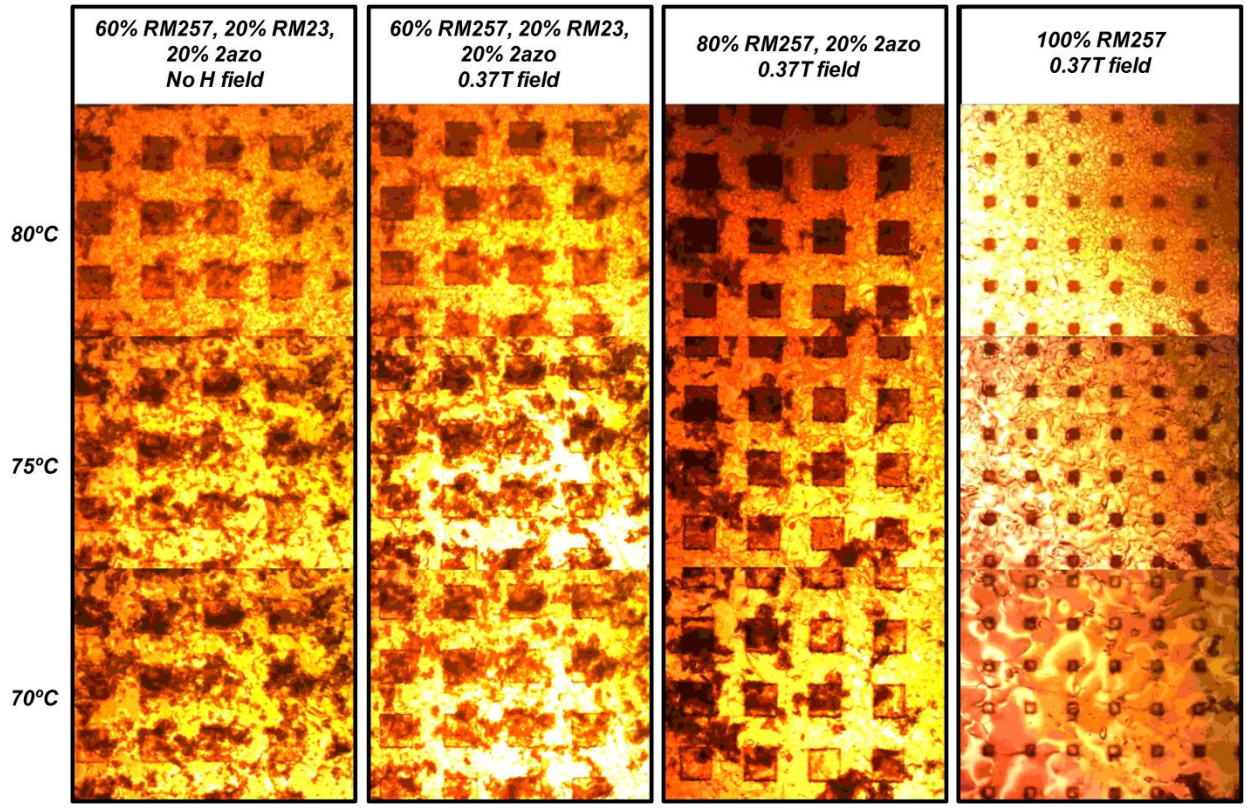

Figure 5-15. Qualitative comparison of LCN order at various temperatures for select LCN compositions.

The presence of nonbirefringent areas based on the cooling rate is observed in Figure 5-16. The nonbirefringent areas are largely formed in the same locations regardless of cooling rate; however, slower cooling rates do have an impact on the defects within structures showing no dark areas. This along with the constant location of nonbirefringent areas and their dependence on the composition of the mixture would suggest that these areas may be material that is precipitating out of the LC mixture at the defect sites in the PDMS mold.

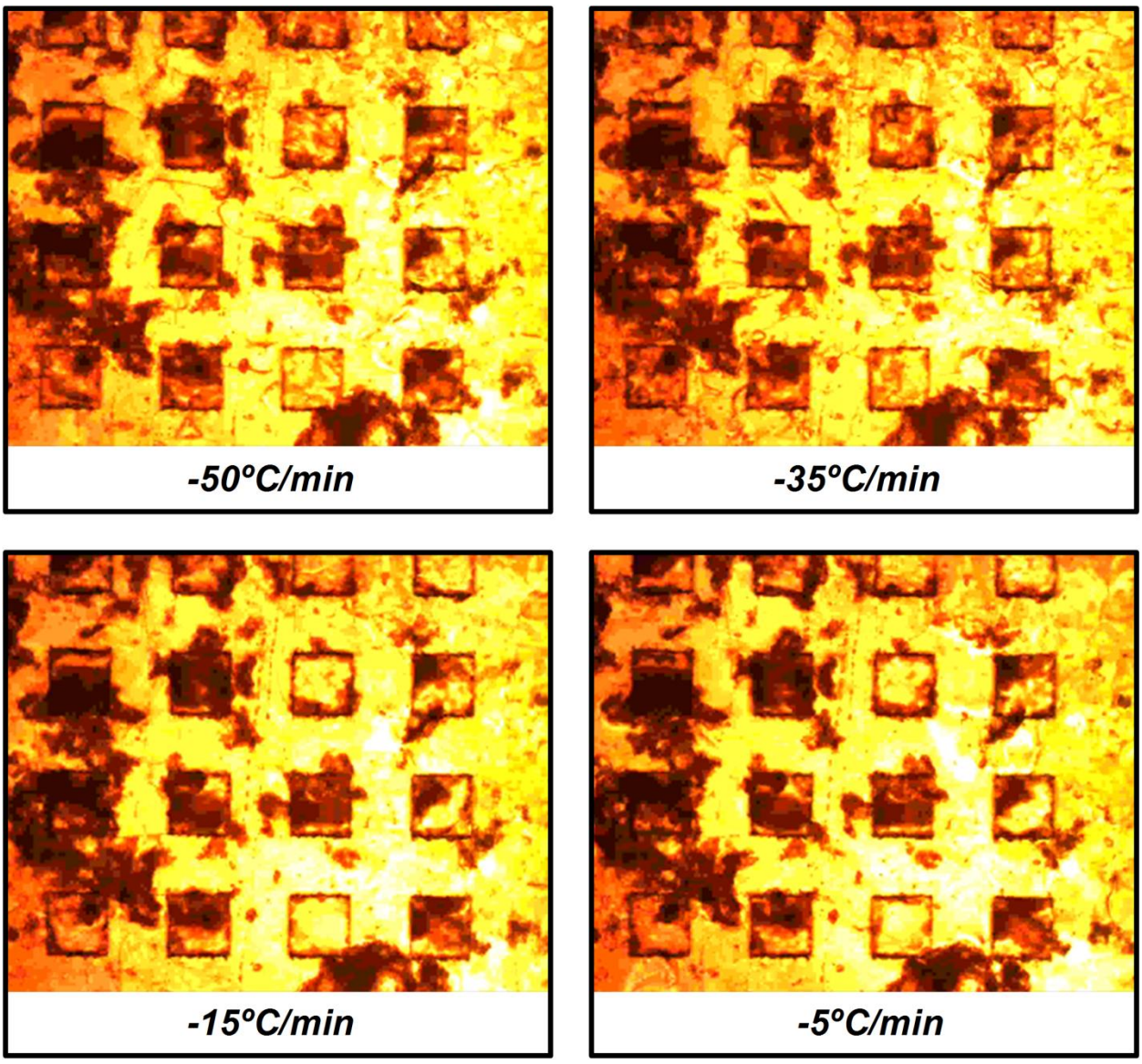

Figure 5-16. Qualitative comparison of LCN order for samples cooled at select rates.

Although analyzing the nonbirefringent areas is out of the scope of this work, Figure 5-17 shows the impact localized nonbirefringent areas have on the performance of a thermally active LCN microstructure cast from RMM491. Figure 5-17b and c showcase the cast fidelity of microstructures with slight and moderate presence of nonbirefringent areas, respectively. It should be noted that the defects at the base of these structures are due to defects in the PDMS mold itself. These SEM images confirm that the nonbirefringent areas are indeed a material defect, rather than a surface roughness defect. The thermally generated strain at 120ºC of

microstructures show in Figure 5-17b and c is shown in Figure 5-17d and e, respectively. The microstructure with significantly more nonbirefringent area is exhibiting nearly isotropic expansion, whereas the microstructure with a smaller nonbirefringent area is showing anisotropic expansion. However, it appears that even the presence of a small nonbirefringent area, relative to the structure cross section, may lead to a significant loss of alignment or actuation performance as even the structure with a small nonbirefringent areais showing expansion along the director.

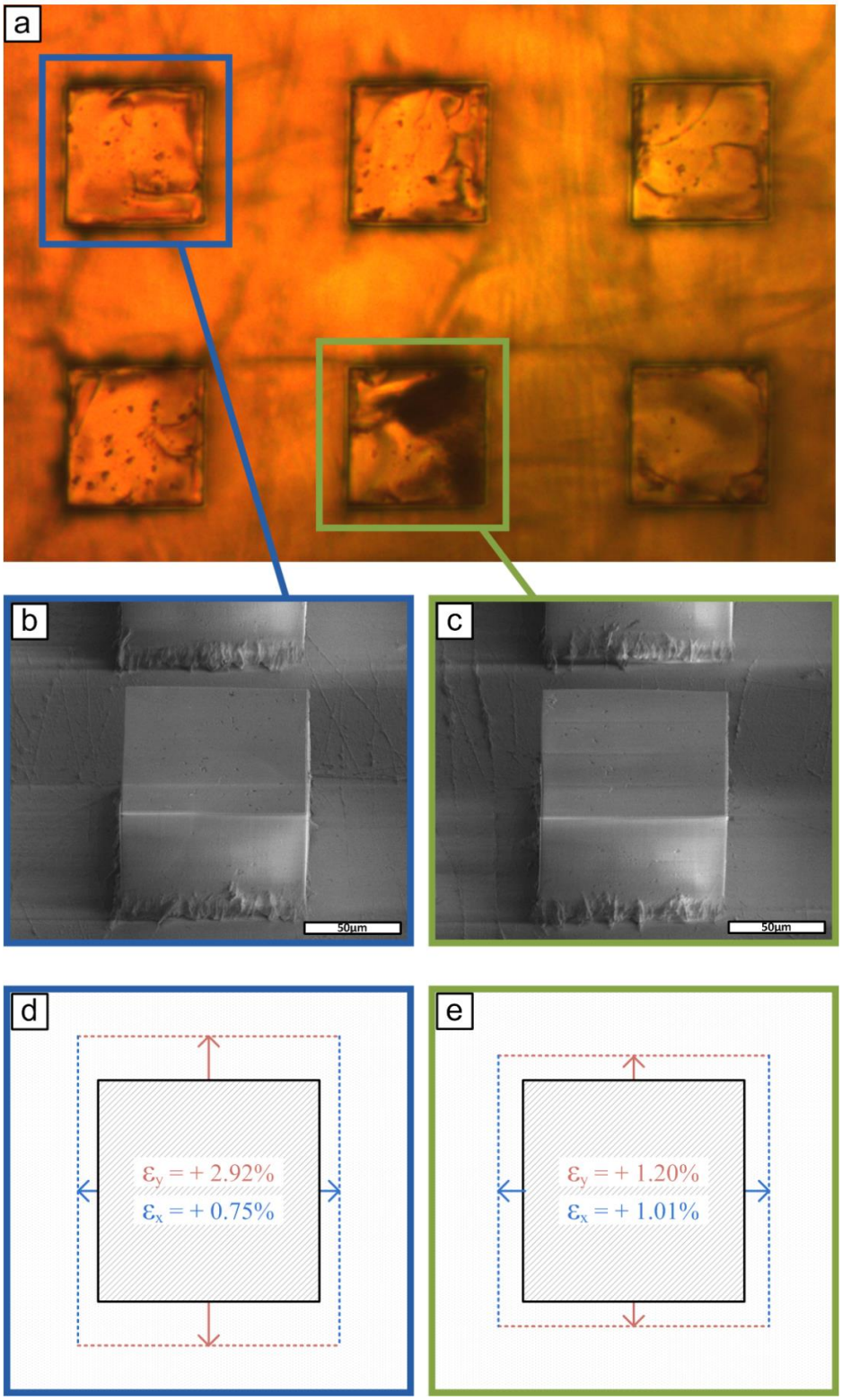

Figure 5-17. Correlation of unknown LCN defect to microstructure morphology and thermally generated strain. (b-c) SEM images of defective microstructures. (d-e) Dependence of thermally generated strain at 120ºC on defects within the microstructure.

5.5 Conclusion

LCN microactuators were fabricated and tested, exhibiting up to 0.25% strain along the director and a 0.11% contraction orthogonal to it after 5 min exposure of polarized blue light. For the first time, centimeter-scale areas of high aspect ratio microstructures were fabricated, enabled by careful environmental process control and removal of oxygen during casting. A new setup was created to further investigate the in situ phase behavior of LCN during microstructure casting, which has led to the discovery of nonbirefringent areas induced during casting. This nonbirefringent defect reduces the anisotropy of actuation significantly. With further characterization and improvement of the optically-induced strain, this technology would be suitable for fabrication of active surface textures, such as for use in microfluidics, and possibly on the surfaces of miniature vehicles.

CHAPTER 6: SUMMARY OF CONTRIBUTIONS AND OUTLOOK

6.1 Key contributions of this work

This thesis has demonstrated new methods for fabrication of microstructured surfaces having novel geometries and active properties. In Chapter 2, growth of patterned CNT microstructures was discussed along with an in depth investigation of polymer infiltration into these microstructures to form CNT-polymer nanocomposites and to improve their mechanical properties. Replica molding of complex CNT-SU-8 and DRIE silicon microstructures was used to cast high fidelity, reentrant, and HAR microstructures. In Chapter 4, infiltration of CNT forests with paraffin was shown to result into large stroke thin film actuators that can function as thermal switches. In Chapter 5, replica microstructures were cast from a new class of materials called LCN. Thermally and optically active LCN microstructures were created and their generated strain was quantified.

The major contributions of this thesis are:

- A robust method for fabrication of carbon nanotube composite microstructures by capillary forming followed by capillary driven infiltration of polymers was developed. Scalability, robustness, and high yield of arrays of microstructures fabricated were shown using this method. Heterogeneous microstructures were simultaneously infiltrated in close proximity.

- The use of CNT-SU8 microstructure arrays as robust master molds for fabrication of polymer microstructures was demonstrated. Reentrant, bent, and twisted microstructures were created using the developed process. Additionally, high aspect ratio CNT-SU-8 microstructures (AR=50) with 400nm lateral dimension were created

and subsequently replicated. These microstructures would be challenging to create using standard lithographic techniques.

- An analytical model based on first principles describing the infiltration of CNT microstructures with liquid was developed. The model employs the balance of viscous and centrifugal forces during spincoating for pressures and velocities of a deformable control volume to predict the height change per time of an arbitrary liquid between two microstructures. The model allows for increasing liquid level uniformity between microstructures of various spacing, while minimizing the loads exerted on microstructures.

- Improvements in stiffness and toughness of CNT-SU-8 and CNT-PMMA nanocomposite microstructures over pure polymers were shown. CNT-SU-8 nanocomposite microstructures are shown to have a stiffness of 18GPa (3.5 times higher than that of SU-8 replicas), while CNT-PMMA nanocomposite microstructures are shown to have a stiffness of 25GPa (8.3 times higher than that of neat PMMA).

- CNT-polymer composite microstructures were electrically integrated and packaged for uses in sensing. CNT-hydrogel microsensors were developed to serve as a sensing platform to instigate CNT transduction of hydrogel stimuli, including wetting and temperature.

- A CNT-paraffin nanocomposite sheet actuator was created and exhibited an 20% strain at 175ºC over multiple cycles. Actuator performance based on CNT morphology, controlled via pre-infiltration compression, and under various loads was quantified. Additionally, two regimes of actuator performance were identified: a regime below the melting temperature exhibiting low strain, but large stiffness, and another regime above the melting temperature exhibiting high strain, but a low stiffness and low stop load. Lastly, use of the CNT-paraffin actuator as a thermal switch was demonstrated.

- A process for replica molding of thermally and optically active LCN microstructures, with in situ application of magnetic field during curing, was developed.

- Large strains of a thermally active LCN microstructures at elevated temperature were demonstrated. The microstructures extended perpendicular to the director by about 6% at 200ºC. This corresponded to a change in cross section as well as an increase in height.

- A library of heterogeneous low aspect ratio optically active microstructures was cast. Additionally, large arrays of anisotropic optically active LCN microstructures was cast, which for the first time reaches dimensions and yield which may be useful in fabrication of optically active surfaces. Actuation of optically active LCN microstructures, exhibiting up to 0.25% strain along the director and a 0.11% contraction orthogonal was demonstrated. The generated strains in microstructures are comparable to actuation strains of centimeter scale cast sheets in literature.

- Designed and built custom vacuum chamber providing magnetic LC alignment with controlled temperature in a compact format to allow for in situ sample imaging. Used in situ imaging to correlate processing parameters to presence of ‘smudging’ defects and further correlated this defect to optically generated strains.

6.2 Remaining challenges and possible future directions

The discussion to follow will largely follow the outline of the thesis and discuss the key consideration and future direction of various parts of the work presented above. In regards to the fabricated passive CNT-polymer composites, there are outstanding questions about their potential as microstructured surfaces to be investigated. Although stiffness and toughness are discussed herein, further characterization of their shear modulus, adhesion strength (in shear, pealing, and axial), damping, surface energy, and tackiness would lead to a better understanding of their applicability towards practical active surfaces.

Future work also remains regarding electrical integration of CNT-polymer microstructures. Particularly, the characteristics of CNT-hydrogel microsensors need further investigation, including the sensitivity, accuracy, precision, sensitivity, drift, and other errors. Potentially, a variety of sensors could be fabricated based on the previously described platform. A potential high impact application would be glucose sensors, which would be fabricated from hydrogels that swell in the presence of glucose [131] and whose swelling would be electrically transduced. Additional applications which this platform would be well suited for rely on the specificity of the hydrogel to a stimulus, the size of sensor, or the demonstrated rapid response. Hydrogel stimuli have been discussed previously, but it is worth mentioning that hydrogel swell in response to DNA sequences [132] and pathogens [133]. These hydrogels exhibit incredible specificity and the transduction of their swelling would make useful immunoassays, especially considering the size and speed of the demonstrated hydrogel sensor.

The work on CNT-paraffin actuators has showed promising thermally generated strains, but the stop load in regime 2 is very low. Further investigation of the stop load and the mechanics in regime 1 are important in understanding the applicability of the developed actuator. Rigorous investigation into the stop load and work density of each regime is also required. Furthermore, relating these properties to the paraffin surface energy and forest nanoscale morphology is important to fully understand the mechanism of actuation.

In addition to investigating the mechanism of actuation, infiltrating CNT microstructures with paraffin would produce surface bound microactuators likely with similar properties as the sheet actuator. There are many challenges in doing so, since it is critical that the sheet actuators

are compressed during infiltration. An approach to solve this problem may be to densify asymmetric CNT pillars to produce bent CNT microstructures, which upon swelling would at least partially return to their straighten state, as suggested by Figure 6-1a and b. Figure 6-1c shows first attempts of infiltrating CNTs with paraffin, while an optimized infiltration method informed by the infiltration modes is shown in Figure 6-1d to produce HAR CNT-paraffin microstructures. The shown microstructures do not actuate as no pre-buckling was applied.

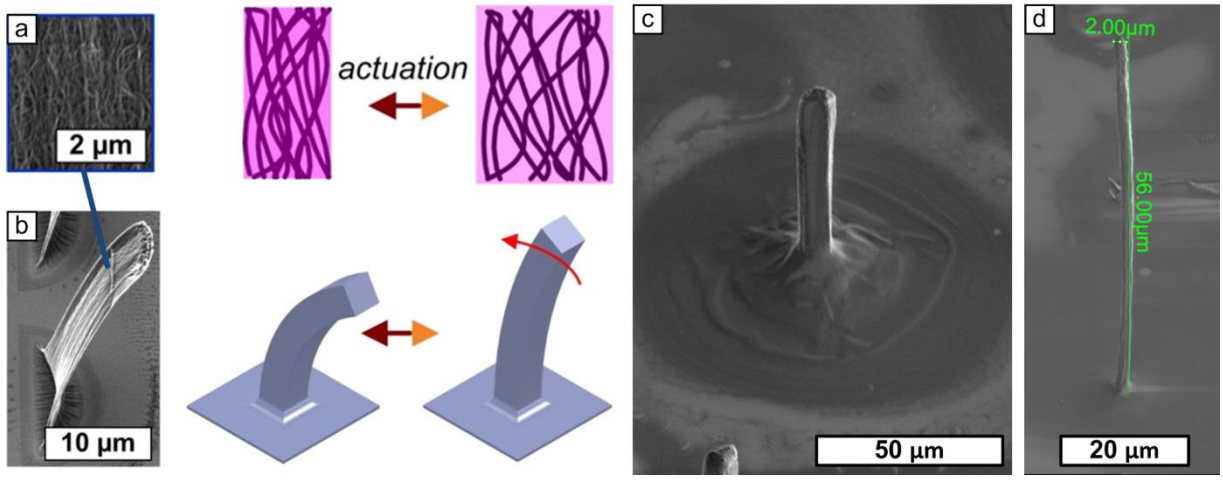

Figure 6-1. First steps towards proposed future work. (a) Schematic of actuation mechanism with (b) associated microscale change in morphology. (c) First attempt at CNT-paraffin nanocomposite microstructures. (d) Optimized processing parameters informed by the infiltration model lead to HAR CNT-paraffin nanocomposite microstructures.

In regards to LCN microstructures, a major effort is needed to either increase their strain (particularly for optically active LCN) or to increase their motion via the design of the microstructure. Rapid shape change could be achieved even with small strains if dynamic instabilities are exploited. To aid in this effort, it would be useful to be able to deterministically predict the stress and strain produced in an arbitrarily shaped microstructure based on its geometry, director orientation, illumination direction, and boundary conditions. Combining these factors would describe the precise motion of this microstructure, but is extremely challenging to do analytically for anything but the simplest geometry. For this reason, FEA simulations are preferred, especially since they would allow for a large number of designs to be investigated. Simulations of thermally active LCN microstructures attached to a rigid substrate with vertically oriented director are shown in Figure 6-2a and b. Another interesting are of investigation is infiltration of thermally active LCN into CNT microstructures, which would use both the

anisotropy of the CNTs and the anisotropy of the actuating LCN to achieved complex motions. Predicting the motion of these structures is a even bigger challenged. Conceptually, these microstructures could be heated locally or globally using either joule heating via electrical integration or light, which would be absorbed by the CNTs.

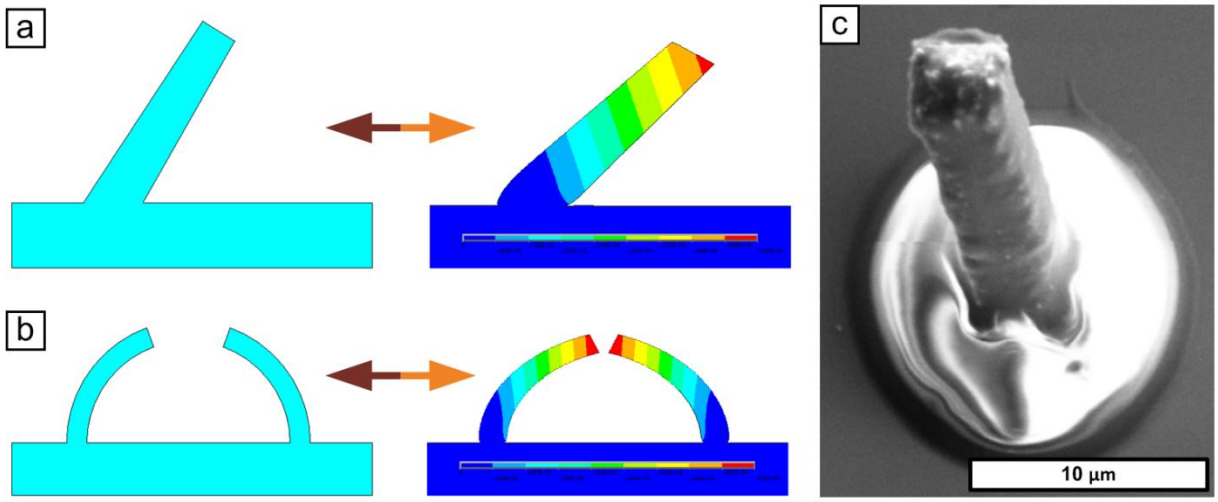

Figure 6-2. (a-b) FEA simulations of thermally active LCN microstructure actuation on rigid substrate. (c) Early thermally active CNT-LCN nanocomposite microstructure.

BIBLIOGRAPHY

[1] C.-C. Hsieh and S.-C. Yao, "Evaporative heat transfer characteristics of a water spray on micro-structured silicon surfaces," *International Journal of Heat and Mass Transfer,* vol. 49, pp. 962-974, 3// 2006.

[2] M. De Volder, S. H. Tawfick, S. J. Park, D. Copic, Z. Zhao, W. Lu, *et al.*, "Diverse 3D Microarchitectures Made by Capillary Forming of Carbon Nanotubes," *Advanced Materials,* vol. 22, pp. 4384-4389, 2010.

[3] J. L. Tan, J. Tien, D. M. Pirone, D. S. Gray, K. Bhadriraju, and C. S. Chen, "Cells lying on a bed of microneedles: An approach to isolate mechanical force," *Proceedings of the National Academy of Sciences,* vol. 100, pp. 1484-1489, 2003.

[4] R. G. Flemming, C. J. Murphy, G. A. Abrams, S. L. Goodman, and P. F. Nealey, "Effects of synthetic micro- and nano-structured surfaces on cell behavior," *Biomaterials,* vol. 20, pp. 573-588, 3// 1999.

[5] M. R. Prausnitz, "Microneedles for transdermal drug delivery," *Advanced Drug Delivery Reviews,* vol. 56, pp. 581-587, 3/27/ 2004.

[6] M. Callies and D. Quere, "On water repellency," *Soft Matter,* vol. 1, pp. 55-61, 2005.

[7] A. Tuteja, W. J. Choi, G. H. McKinley, R. E. Cohen, and M. F. Rubner, "Design parameters for superhydrophobicity and superoleophobicity," vol. 33, pp. 752-758, Aug.

[8] B. Yurdumakan, N. R. Raravikar, P. M. Ajayan, and A. Dhinojwala, "Synthetic gecko foot-hairs from multiwalled carbon nanotubes," pp. 3799-3801, 2005.

[9] Z. J. Wang, S. L. Pan, T. D. Krauss, H. Du, and L. J. Rothberg, "The structural basis for giant enhancement enabling single-molecule Raman scattering," vol. 100, pp. 8638-8643, Jul.

[10] M. Wakuda, Y. Yamauchi, S. Kanzaki, and Y. Yasuda, "Effect of surface texturing on friction reduction between ceramic and steel materials under lubricated sliding contact," *Wear,* vol. 254, pp. 356-363, 2// 2003.

[11] N. Mingo and D. A. Broido, "Carbon Nanotube Ballistic Thermal Conductance and Its Limits," *Physical Review Letters,* vol. 95, p. 096105, 08/26/ 2005.

[12] M. Nihei, M. Horibe, A. Kawabata, and Y. Awano, "Carbon nanotube vias for future LSI interconnects," in *Interconnect Technology Conference, 2004. Proceedings of the IEEE 2004 International*, 2004, pp. 251-253.

[13] J. K. Gansel, M. Thiel, M. S. Rill, M. Decker, K. Bade, V. Saile, *et al.*, "Gold Helix Photonic Metamaterial as Broadband Circular Polarizer," *Science,* vol. 325, pp. 1513-1515, Sep 2009.

[14] N. Blow, "Cell culture: building a better matrix," *Nature Methods,* vol. 6, pp. 619-U94, Aug 2009.

[15] M. A. Unger, H. P. Chou, T. Thorsen, A. Scherer, and S. R. Quake, "Monolithic microfabricated valves and pumps by multilayer soft lithography," *Science,* vol. 288, pp. 113-116, Apr 2000.
[16] M. K. Kwak, H. E. Jeong, W. G. Bae, H.-S. Jung, and K. Y. Suh, "Anisotropic Adhesion Properties of Triangular-Tip-Shaped Micropillars," *Small,* vol. 7, pp. 2296-2300, 2011.
[17] L. Ge, S. Sethi, L. Ci, P. M. Ajayan, and A. Dhinojwala, "Carbon nanotube-based synthetic gecko tapes," *Proceedings of the National Academy of Sciences,* vol. 104, pp. 10792-10795, 2007.
[18] H. E. Jeong and K. Y. Suh, "Nanohairs and nanotubes: Efficient structural elements for gecko-inspired artificial dry adhesives," *Nano Today,* vol. 4, pp. 335-346, 8// 2009.
[19] A. del Campo and C. Greiner, "SU-8: a photoresist for high-aspect-ratio and 3D submicron lithography," *Journal of Micromechanics and Microengineering,* vol. 17, pp. R81-R95, Jun 2007.
[20] A. Bertsch, S. Jiguet, and P. Renaud, "Microfabrication of ceramic components by microstereolithography," *Journal of Micromechanics and Microengineering,* vol. 14, pp. 197-203, Feb 2004.
[21] C. N. LaFratta, J. T. Fourkas, T. Baldacchini, and R. A. Farrer, "Multiphoton fabrication," *Angewandte Chemie-International Edition,* vol. 46, pp. 6238-6258, 2007.
[22] S. Reyntjens and R. Puers, "A review of focused ion beam applications in microsystem technology," *Journal of Micromechanics and Microengineering,* vol. 11, pp. 287-300, Jul 2001.
[23] A. Sidorenko, T. Krupenkin, and J. Aizenberg, "Controlled switching of the wetting behavior of biomimetic surfaces with hydrogel-supported nanostructures," *Journal of Materials Chemistry,* vol. 18, pp. 3841-3846, 2008.
[24] P. Kim, L. D. Zarzar, M. Khan, M. Aizenberg, and J. Aizenberg, "Environmentally responsive active optics based on hydrogel-actuated deformable mirror arrays," 2011, pp. 792705-792705-7.
[25] B. Zhao and J. S. Moore, "Fast pH- and Ionic Strength-Responsive Hydrogels in Microchannels," *Langmuir,* vol. 17, pp. 4758-4763, 2001/08/01 2001.
[26] T. Tanaka, D. Fillmore, S.-T. Sun, I. Nishio, G. Swislow, and A. Shah, "Phase Transitions in Ionic Gels," *Physical Review Letters,* vol. 45, pp. 1636-1639, 11/17/ 1980.
[27] E. W. H. Jager, E. Smela, and O. Inganäs, "Microfabricating Conjugated Polymer Actuators," *Science,* vol. 290, pp. 1540-1545, 2000.
[28] X. Yao, Y. Hu, A. Grinthal, T.-S. Wong, L. Mahadevan, and J. Aizenberg, "Adaptive fluid-infused porous films with tunable transparency and wettability," *Nat Mater,* vol. 12, pp. 529-534, 06//print 2013.
[29] B. Peng, M. Locascio, P. Zapol, S. Li, S. L. Mielke, G. C. Schatz, *et al.*, "Measurements of near-ultimate strength for multiwalled carbon nanotubes and irradiation-induced crosslinking improvements," *Nature Nanotechnology,* vol. 3, pp. 626-631, Oct 2008.
[30] B. Q. Wei, R. Vajtai, and P. M. Ajayan, "Reliability and current carrying capacity of carbon nanotubes," *Applied Physics Letters,* vol. 79, Aug 20 2001.
[31] E. Pop, D. Mann, Q. Wang, K. Goodson, and H. Dai, "Thermal Conductance of an Individual Single-Wall Carbon Nanotube above Room Temperature," *Nano Letters,* vol. 6, pp. 96-100, 2006/01/01 2005.

[32] M. F. L. De Volder, S. H. Tawfick, R. H. Baughman, and A. J. Hart, "Carbon Nanotubes: Present and Future Commercial Applications," *Science,* vol. 339, pp. 535-539, Feb 1 2013.
[33] J. N. Coleman, U. Khan, W. J. Blau, and Y. K. Gun'ko, "Small but strong: A review of the mechanical properties of carbon nanotube-polymer composites," *Carbon,* vol. 44, pp. 1624-1652, Aug 2006.
[34] M. F. L. De Volder, D. O. Vidaud, E. R. Meshot, S. Tawfick, and A. J. Hart, "Self-similar organization of arrays of individual carbon nanotubes and carbon nanotube micropillars," *Microelectronic Engineering,* vol. 87, pp. 1233-1238, 2010.
[35] Z. Spitalsky, D. Tasis, K. Papagelis, and C. Galiotis, "Carbon nanotube–polymer composites: Chemistry, processing, mechanical and electrical properties," *Progress in Polymer Science,* vol. 35, pp. 357-401, 3// 2010.
[36] R. Andrews and M. C. Weisenberger, "Carbon nanotube polymer composites," *Current Opinion in Solid State and Materials Science,* vol. 8, pp. 31-37, 1// 2004.
[37] P. M. Ajayan, L. S. Schadler, C. Giannaris, and A. Rubio, "Single-Walled Carbon Nanotube–Polymer Composites: Strength and Weakness," *Advanced Materials,* vol. 12, pp. 750-753, 2000.
[38] H. Cebeci, R. G. d. Villoria, A. J. Hart, and B. L. Wardle, "Multifunctional properties of high volume fraction aligned carbon nanotube polymer composites with controlled morphology," *Composites Science and Technology,* vol. 69, pp. 2649-2656, 12// 2009.
[39] O. Breuer and U. Sundararaj, "Big returns from small fibers: A review of polymer/carbon nanotube composites," *Polymer Composites,* vol. 25, pp. 630-645, 2004.
[40] B. Maruyama and K. Alam, "Carbon nanotubes and nanofibers in composite materials," *Sampe Journal,* vol. 38, pp. 59-70, 2002.
[41] M. Sennett, E. Welsh, J. B. Wright, W. Z. Li, J. G. Wen, and Z. F. Ren, "Dispersion and alignment of carbon nanotubes in polycarbonate," *Applied Physics A,* vol. 76, pp. 111-113, 2003/01/01 2003.
[42] J. C. Kearns and R. L. Shambaugh, "Polypropylene fibers reinforced with carbon nanotubes," *Journal of Applied Polymer Science,* vol. 86, pp. 2079-2084, 2002.
[43] S. Kumar, H. Doshi, M. Srinivasarao, J. O. Park, and D. A. Schiraldi, "Fibers from polypropylene/nano carbon fiber composites," *Polymer,* vol. 43, pp. 1701-1703, 3// 2002.
[44] B. Z. Tang and H. Xu, "Preparation, Alignment, and Optical Properties of Soluble Poly(phenylacetylene)-Wrapped Carbon Nanotubes†," *Macromolecules,* vol. 32, pp. 2569-2576, 1999/04/01 1999.
[45] E. K. Hobbie, H. Wang, H. Kim, S. Lin-Gibson, and E. A. Grulke, "Orientation of carbon nanotubes in a sheared polymer melt," *Physics of Fluids,* vol. 15, pp. 1196-1202, // 2003.
[46] H. Schreuder-Gibson, K. Senecal, M. Sennett, L. Samuelson, Z. Huang, J. Wen, *et al.*, "Characteristics of electrospun fibers containing carbon nanotubes," p. 210.
[47] A. Allaoui, S. Bai, H. M. Cheng, and J. B. Bai, "Mechanical and electrical properties of a MWNT/epoxy composite," *Composites Science and Technology,* vol. 62, pp. 1993-1998, 11// 2002.
[48] V. G. Hadjiev, M. N. Iliev, S. Arepalli, P. Nikolaev, and B. S. Files, "Raman scattering test of single-wall carbon nanotube composites," *Applied Physics Letters,* vol. 78, pp. 3193-3195, // 2001.

[49] J. Sandler, M. S. P. Shaffer, T. Prasse, W. Bauhofer, K. Schulte, and A. H. Windle, "Development of a dispersion process for carbon nanotubes in an epoxy matrix and the resulting electrical properties," *Polymer,* vol. 40, pp. 5967-5971, 10// 1999.
[50] K.-T. Lau and D. Hui, "Effectiveness of using carbon nanotubes as nano-reinforcements for advanced composite structures," *Carbon,* vol. 40, pp. 1605-1606, 8// 2002.
[51] L. S. Schadler, S. C. Giannaris, and P. M. Ajayan, "Load transfer in carbon nanotube epoxy composites," *Applied Physics Letters,* vol. 73, pp. 3842-3844, // 1998.
[52] H. Bubert, S. Haiber, W. Brandl, G. Marginean, M. Heintze, and V. Brüser, "Characterization of the uppermost layer of plasma-treated carbon nanotubes," *Diamond and Related Materials,* vol. 12, pp. 811-815, 3// 2003.
[53] Y. Xia, E. Kim, and G. M. Whitesides, "Micromolding of Polymers in Capillaries: Applications in Microfabrication," *Chemistry of Materials,* vol. 8, pp. 1558-1567, 1996.
[54] Y. Xia, J. J. McClelland, R. Gupta, D. Qin, X.-M. Zhao, L. L. Sohn, *et al.*, "Replica molding using polymeric materials: A practical step toward nanomanufacturing," *Advanced Materials,* vol. 9, pp. 147-149, 1997.
[55] Y. Xia and G. M. Whitesides, "Soft Lithography," *Angewandte Chemie International Edition,* vol. 37, pp. 550-575, 1998.
[56] S. Jung, C. Kang, I. Jung, S. Lee, P. Jung, and J. Ko, "Fabrication of curved copper micromesh sheets using flexible PDMS molds," *Microsystem Technologies,* vol. 14, pp. 829-833, 2008.
[57] B. Pokroy, A. K. Epstein, M. C. M. Persson-Gulda, and J. Aizenberg, "Fabrication of Bioinspired Actuated Nanostructures with Arbitrary Geometry and Stiffness," *Advanced Materials,* vol. 21, pp. 463-+, Jan 2009.
[58] A. Buguin, M. H. Li, P. Silberzan, B. Ladoux, and P. Keller, "Micro-actuators: When artificial muscles made of nematic liquid crystal elastomers meet soft lithography," *Journal of the American Chemical Society,* vol. 128, pp. 1088-1089, Feb 1 2006.
[59] D. Copic, S. J. Park, S. Tawfick, M. De Volder, and A. J. Hart, "Fabrication, Densification, and Replica Molding of 3D Carbon Nanotube Microstructures," p. e3980, 2012/07/02/ 2012.
[60] D. Copic, S. J. Park, S. Tawfick, M. F. L. De Volder, and A. J. Hart, "Fabrication of high-aspect-ratio polymer microstructures and hierarchical textures using carbon nanotube composite master molds," *Lab on a Chip,* vol. 11, pp. 1831-1837, 2011.
[61] D. Copic and A. J. Hart, "High-stroke actuation of aligned CNT-paraffin composite films," in *19th International Conference on Composite Materials (ICCM)*, Montreal, 2013.
[62] D. Copic, A. Ya'akobovitz, and A. J. Hart, "Replica molding of liquid crystal polymer microstructures for active surfaces," in *19th International Conference on Composite Materials (ICCM)*, 2013.
[63] M. Callies and D. Quere, "On water repellency," vol. 1, pp. 55-61, Jun.
[64] E. Arzt, S. Gorb, and R. Spolenak, "From micro to nano contacts in biological attachment devices," vol. 100, pp. 10603-10606, Sep.
[65] W. Xuefeng and et al., "Liquid crystal polymer (LCP) for MEMS: processes and applications," *Journal of Micromechanics and Microengineering,* vol. 13, p. 628, 2003.
[66] L. Soleymani, Z. C. Fang, E. H. Sargent, and S. O. Kelley, "Programming the detection limits of biosensors through controlled nanostructuring," vol. 4, pp. 844-848, Dec.

[67] M. R. K. Mofrad and R. D. Kamm, *Cellular Mechanotransduction: Diverse Perspectives From Molecules to Tissues*: Cambridge University Press, 2009.
[68] D. E. Ingber, "Mechanobiology and diseases of mechanotransduction," *Annals of Medicine,* vol. 35, pp. 564-577, 2003.
[69] V. Brunetti, G. Maiorano, L. Rizzello, B. Sorce, S. Sabella, R. Cingolani, *et al.*, "Neurons sense nanoscale roughness with nanometer sensitivity," vol. 107, pp. 6264-6269, Apr.
[70] D. H. Kim, E. A. Lipke, P. Kim, R. Cheong, S. Thompson, M. Delannoy, *et al.*, "Nanoscale cues regulate the structure and function of macroscopic cardiac tissue constructs," vol. 107, pp. 565-570, Jan.
[71] S. Oh, K. S. Brammer, Y. S. J. Li, D. Teng, A. J. Engler, S. Chien, *et al.*, "Stem cell fate dictated solely by altered nanotube dimension," vol. 106, pp. 2130-2135, Feb.
[72] Y. N. Xia and G. M. Whitesides, "Soft lithography," vol. 28, pp. 153-184, 1998.
[73] Q. Xu, B. T. Mayers, M. Lahav, D. V. Vezenov, and G. M. Whitesides, "Approaching Zero: Using Fractured Crystals in Metrology for Replica Molding," *Journal of the American Chemical Society,* vol. 127, pp. 854-855, 2004.
[74] F. Hua, Y. Sun, A. Gaur, M. A. Meitl, L. Bilhaut, L. Rotkina, *et al.*, "Polymer Imprint Lithography with Molecular-Scale Resolution," *Nano Letters,* vol. 4, pp. 2467-2471, 2004.
[75] M. Sun, C. Luo, L. Xu, H. Ji, Q. Ouyang, D. Yu, *et al.*, "Artificial Lotus Leaf by Nanocasting," *Langmuir,* vol. 21, pp. 8978-8981, 2005.
[76] S.-H. Kang, T.-Y. Tai, and T.-H. Fang, "Replication of butterfly wing microstructures using molding lithography," *Current Applied Physics,* vol. 10, pp. 625-630, 2010.
[77] B. W. Maynor, I. LaRue, Z. Hu, J. P. Rolland, A. Pandya, Q. Fu, *et al.*, "Supramolecular Nanomimetics: Replication of Micelles, Viruses, and Other Naturally Occurring Nanoscale Objects," *Small,* vol. 3, pp. 845-849, 2007.
[78] D. N. Hutchison, N. B. Morrill, Q. Aten, B. W. Turner, B. D. Jensen, L. L. Howell, *et al.*, "Carbon Nanotubes as a Framework for High-Aspect-Ratio MEMS Fabrication," vol. 19, pp. 75-82, Feb.
[79] A. J. Hart and A. H. Slocum, "Rapid growth and flow-mediated nucleation of millimeter-scale aligned carbon nanotube structures from a thin-film catalyst," vol. 110, pp. 8250-8257, Apr.
[80] B. P. Chaudhri, F. Ceyssens, P. De Moor, C. Van Hoof, and R. Puers, "A high aspect ratio SU-8 fabrication technique for hollow microneedles for transdermal drug delivery and blood extraction," *J. Micromech. Microeng.*, vol. 20, pp. 1-6, 2010.
[81] J. D. Williams and W. J. Wang, "Study on the postbaking process and the effects on UV lithography of high aspect ratio SU-8 microstructures," *Journal of Microlithography Microfabrication and Microsystems,* vol. 3, pp. 563-568, 2004.
[82] E. Reznikova, J. Mohr, M. Boerner, V. Nazmov, and P. J. Jakobs, "Soft X-ray lithography of high aspect ratio SU8 submicron structures," *Microsystem Technologies-Micro-and Nanosystems-Information Storage and Processing Systems,* vol. 14, pp. 1683-1688, 2008.
[83] D. Tasis, N. Tagmatarchis, A. Bianco, and M. Prato, "Chemistry of Carbon Nanotubes," *Chemical Reviews,* vol. 106, pp. 1105-1136, 2006/03/01 2006.
[84] C. R. Oliver, E. S. Polsen, E. R. Meshot, S. Tawfick, S. J. Park, M. Bedewy, *et al.*, "Statistical Analysis of Variation in Laboratory Growth of Carbon Nanotube Forests and Recommendations for Improved Consistency," *ACS Nano,* vol. 7, pp. 3565-3580, 2013.

[85] M. F. L. De Volder , S. J. Park, S. H. Tawfick, D. O. Vidaud, and A. J. Hart, "Fabrication and electrical integration of robust carbon nanotube micropillars by self-directed elastocapillary densification," *Journal of Micromechanics and Microengineering,* vol. 21, p. 045033, 2011.
[86] C. Py, R. Bastien, J. Bico, B. Roman, and A. Boudaoud, "3D aggregation of wet fibers," *Europhysics Letters,* vol. 77, 2007.
[87] F. L. D. V. a. S. J. P. a. S. H. T. a. D. O. V. a. A. J. H. Michaël, "Fabrication and electrical integration of robust carbon nanotube micropillars by self-directed elastocapillary densification," *Journal of Micromechanics and Microengineering,* vol. 21, p. 045033, 2011.
[88] Z. Zhao, S. H. Tawfick, S. J. Park, M. De Volder, A. J. Hart, and W. Lu, "Bending of nanoscale filament assemblies by elastocapillary densification," *Physical Review E,* vol. 82, p. 041605, 2010.
[89] K. Wouters and R. Puers, "Determining the Young's modulus and creep effects in three different photo definable epoxies for MEMS applications," *Sensors and Actuators a-Physical,* vol. 156, pp. 196-200, Nov 2009.
[90] A. L. Bogdanov and S. S. Peredkov, "Use of SU-8 photoresist-for very high aspect ratio x-ray lithography," *Microelectronic Engineering,* vol. 53, pp. 493-496, 2000.
[91] D. Copic, S. J. Park, S. Tawfick, M. F. L. De Volder, and A. J. Hart, "Fabrication of high-aspect-ratio polymer microstructures and hierarchical textures using carbon nanotube composite master molds," *Lab Chip,* 2011.
[92] S. Benltoufa, F. Fayala, and S. BenNasrallah, "Capillary Rise in Macro and Micro Pores of Jersey Knitting Structure," *Journal of Engineered Fibers and Fabrics,* vol. 3, pp. 47-54, 2008.
[93] E. W. Washburn, "The Dynamics of Capillary Flow," *Physical Review,* vol. 17, p. 273, 1921.
[94] A. G. Emslie, F. T. Bonner, and L. G. Peck, "Flow of a viscous liquid on a rotating disk," *Journal of Applied Physics,* vol. 29, pp. 858-862, // 1958.
[95] A. Acrivos, M. J. Shah, and E. E. Petersen, "On the flow of a non-newtonian liquid on a rotating disk," *Journal of Applied Physics,* vol. 31, pp. 963-968, // 1960.
[96] E. J. García, A. J. Hart, B. L. Wardle, and A. H. Slocum, "Fabrication and Nanocompression Testing of Aligned Carbon-Nanotube–Polymer Nanocomposites," *Advanced Materials,* vol. 19, pp. 2151-2156, 2007.
[97] M. De Volder, S. H. Tawfick, D. Copic, and A. J. Hart, "Hydrogel-driven carbon nanotube microtransducers," *Soft Matter,* vol. 7, pp. 9844-9847, 2011.
[98] Z. Yang, Z. Cao, H. Sun, and Y. Li, "Composite Films Based on Aligned Carbon Nanotube Arrays and a Poly(N-Isopropyl Acrylamide) Hydrogel," *Advanced Materials,* vol. 20, pp. 2201-2205, 2008.
[99] L. Klintberg, M. Karlsson, L. Stenmark, J. Schweitz, and G. Thornell, "A large stroke, high force paraffin phase transition actuator," *Sensors and Actuators A: Physical,* vol. 96, pp. 189-195, // 2002.
[100] E. T. Carlen and C. H. Mastrangelo, "Electrothermally activated paraffin microactuators," *Microelectromechanical Systems, Journal of,* vol. 11, pp. 165-174, 2002.
[101] E. T. Carlen and C. H. Mastrangelo, "Paraffin actuated surface micromachined valves," in *Micro Electro Mechanical Systems, 2000. MEMS 2000. The Thirteenth Annual International Conference on*, 2000, pp. 381-385.

[102] R. Bodén, M. Lehto, U. Simu, G. Thornell, K. Hjort, and J.-Å. Schweitz, "A polymeric paraffin actuated high-pressure micropump," *Sensors and Actuators A: Physical,* vol. 127, pp. 88-93, 2/28/ 2006.
[103] P. Selvaganapathy, E. T. Carlen, and C. H. Mastrangelo, "Electrothermally actuated inline microfluidic valve," *Sensors and Actuators A: Physical,* vol. 104, pp. 275-282, 5/15/ 2003.
[104] M. Lehto, R. Boden, U. Simu, K. Hjort, G. Thornell, J. Schweitz, *et al.*, "A Polymeric Paraffin Microactuator," *Microelectromechanical Systems, Journal of,* vol. 17, pp. 1172-1177, 2008.
[105] M. D. Lima, N. Li, M. Jung de Andrade, S. Fang, J. Oh, G. M. Spinks, *et al.*, "Electrically, Chemically, and Photonically Powered Torsional and Tensile Actuation of Hybrid Carbon Nanotube Yarn Muscles," *Science,* vol. 338, pp. 928-932, 2012.
[106] A. Cao, P. L. Dickrell, W. G. Sawyer, M. N. Ghasemi-Nejhad, and P. M. Ajayan, "Super-Compressible Foamlike Carbon Nanotube Films," *Science,* vol. 310, pp. 1307-1310, 2005.
[107] Y. S. Song and J. R. Youn, "Evaluation of effective thermal conductivity for carbon nanotube/polymer composites using control volume finite element method," *Carbon,* vol. 44, pp. 710-717, 4// 2006.
[108] A. M. Marconnet, N. Yamamoto, M. A. Panzer, B. L. Wardle, and K. E. Goodson, "Thermal Conduction in Aligned Carbon Nanotube–Polymer Nanocomposites with High Packing Density," *ACS Nano,* vol. 5, pp. 4818-4825, 2011/06/28 2011.
[109] K. M. Lee, N. V. Tabiryan, T. J. Bunning, and T. J. White, "Photomechanical mechanism and structure-property considerations in the generation of photomechanical work in glassy, azobenzene liquid crystal polymer networks," *Journal of Materials Chemistry,* vol. 22, pp. 691-698, 2012.
[110] K. M. Lee, H. Koerner, R. A. Vaia, T. J. Bunning, and T. J. White, "Relationship between the Photomechanical Response and the Thermomechanical Properties of Azobenzene Liquid Crystalline Polymer Networks," *Macromolecules,* vol. 43, pp. 8185-8190, Oct 12 2010.
[111] A. Shimamura, A. Priimagi, J.-i. Mamiya, T. Ikeda, Y. Yu, C. J. Barrett, *et al.*, "Simultaneous Analysis of Optical and Mechanical Properties of Cross-Linked Azobenzene-Containing Liquid-Crystalline Polymer Films," *ACS Applied Materials & Interfaces,* vol. 3, pp. 4190-4196, 2011/11/23 2011.
[112] Y. Yu, M. Nakano, and T. Ikeda, "Photomechanics: Directed bending of a polymer film by light," *Nature,* vol. 425, pp. 145-145, 09/11/print 2003.
[113] C. L. van Oosten, C. W. M. Bastiaansen, and D. J. Broer, "Printed artificial cilia from liquid-crystal network actuators modularly driven by light," *Nat Mater,* vol. 8, pp. 677-682, 2009.
[114] M. Camacho-Lopez, H. Finkelmann, P. Palffy-Muhoray, and M. Shelley, "Fast liquid-crystal elastomer swims into the dark," *Nat Mater,* vol. 3, pp. 307-310, 05//print 2004.
[115] T. J. White, N. V. Tabiryan, S. V. Serak, U. A. Hrozhyk, V. P. Tondiglia, H. Koerner, *et al.*, "A high frequency photodriven polymer oscillator," *Soft Matter,* vol. 4, pp. 1796-1798, 2008 2008.
[116] J. Cviklinski, A. R. Tajbakhsh, and E. M. Terentjev, "UV isomerisation in nematic elastomers as a route to photo-mechanical transducer," *The European Physical Journal E,* vol. 9, pp. 427-434, 2002/12/01 2002.

[117] P. M. Hogan, A. R. Tajbakhsh, and E. M. Terentjev, "uv manipulation of order and macroscopic shape in nematic elastomers," *Physical Review E,* vol. 65, p. 041720, 04/12/ 2002.
[118] Y. Yu, M. Nakano, A. Shishido, T. Shiono, and T. Ikeda, "Effect of Cross-linking Density on Photoinduced Bending Behavior of Oriented Liquid-Crystalline Network Films Containing Azobenzene," *Chemistry of Materials,* vol. 16, pp. 1637-1643, 2004/05/01 2004.
[119] T. J. White, S. V. Serak, N. V. Tabiryan, R. A. Vaia, and T. J. Bunning, "Polarization-controlled, photodriven bending in monodomain liquid crystal elastomer cantilevers," *Journal of Materials Chemistry,* vol. 19, pp. 1080-1085, 2009 2009.
[120] Y. Torres, T. White, A. McClung, and W. Oates, "Photoresponsive Azobenzene Liquid Crystal Polymer Networks: In Situ Photogenerated Stress Measurement," *ASME Conference Proceedings,* vol. 2010, pp. 39-45, 01/01/ 2010.
[121] H. Rau, "Photoisomerization of azobenzenes," ed, 1988, p. 4.
[122] T. Ikeda, ed, 2009, p. 514.
[123] N. Tabiryan, S. Serak, X.-M. Dai, and T. Bunning, "Polymer film with optically controlled form and actuation," *Opt. Express,* vol. 13, pp. 7442-7448, 09/19 2005.
[124] D. B. a. A. J. H. Assaf Ya'akobovitz and Davor Copic and Justin, "Nanoscale displacement measurement of microdevices via interpolation-based edge tracking of optical images," *Journal of Micromechanics and Microengineering,* vol. 23, p. 045004, 2013.
[125] P.-G. d. Gennes and J. Prost, *The physics of liquid crystals*. Oxford : New York: Clarendon Press ; Oxford University Press, 1993.
[126] A. C. Ya'akobovitz, D.Beroz, J.Hart, A.J., "Nanoscale displacement measurement of micro-devices via interpolation-based edge tracking of optical images," *(in review).*
[127] J. R. Bellare, H. T. Davis, W. G. Miller, and L. E. Scriven, "Polarized optical microscopy of anisotropic media: Imaging theory and simulation," *Journal of Colloid and Interface Science,* vol. 136, pp. 305-326, 5// 1990.
[128] A. Saupe, "Textures, deformations, and structural order of liquid crystals," *Journal of Colloid and Interface Science,* vol. 58, pp. 549-558, 3/1/ 1977.
[129] I. Dierking, *Textures of Liquid Crystals*: Wiley, 2006.
[130] J. Nehring and A. Saupe, "On the schlieren texture in nematic and smectic liquid crystals," *Journal of the Chemical Society, Faraday Transactions 2: Molecular and Chemical Physics,* vol. 68, pp. 1-15, 1972.
[131] J. D. Ehrick, M. R. Luckett, S. Khatwani, Y. Wei, S. K. Deo, L. G. Bachas, *et al.*, "Glucose Responsive Hydrogel Networks Based on Protein Recognition," *Macromolecular Bioscience,* vol. 9, pp. 864-868, 2009.
[132] K. G. Olsen, D. J. Ross, and M. J. Tarlov, "Immobilization of DNA Hydrogel Plugs in Microfluidic Channels," *Analytical Chemistry,* vol. 74, pp. 1436-1441, 2002/03/01 2002.
[133] G. Thomas, E. M. El-Giar, L. E. Locascio, and M. J. Tarlov, "Hydrogel-Immobilized Antibodies for Microfluidic Immunoassays," in *Microfluidic Techniques*. vol. 321, ed, 2005, pp. 83-95.